DESIGN, FABRICATION, AND CHARACTERIZATION OF DOUBLE-NEGATIVE METAMATERIALS FOR PHOTONICS

Zur Erlangung des akademischen Grades eines
DOKTORS DER NATURWISSENSCHAFTEN
von der Fakultät für Physik der
Universität Karlsruhe (TH)

genehmigte

DISSERTATION

von

Diplom-Physiker Gunnar Dolling
aus Cuxhaven

Tag der mündlichen Prüfung:	20. Juli 2007
Referent:	Prof. Dr. Martin Wegener
Korreferent:	Prof. Dr. Kurt Busch

Publications

Parts of this thesis have already been published:

In scientific journals:

- G. Dolling, M. W. Klein, M. Wegener, A. Schädle, S. Burger, and S. Linden, *Negative beam displacements from negative-index photonic metamaterials*, in preparation (2007).
- G. Dolling, M. Wegener, C. M. Soukoulis, and S. Linden, *Design-related losses of double-fishnet negative-index photonic metamaterials*, Opt. Express, submitted (2007).
- M. Wegener, G. Dolling, and S. Linden, *Plasmonics: Backward waves moving forward*, Nature Mater. **6**, 475 (2007).
- G. Dolling, M. Wegener, and S. Linden, *Realization of a three-functional-layer negative-index photonic metamaterial*, Opt. Lett. **32**, 551 (2007).
- G. Dolling, M. Wegener, C. M. Soukoulis, and S. Linden, *Negative-index metamaterial at 780 nm wavelength*, Opt. Lett. **32**, 53 (2007).
- G. Dolling, M. Wegener, and S. Linden, *Der falsche Knick im Licht: Metamaterialien mit negativem Brechungsindex*, invited paper, Phys. Unserer Zeit **38**, 24 (2006).
- S. Linden, C. Enkrich, G. Dolling, M. W. Klein, J. F. Zhou, T. Koschny, C. M. Soukoulis, S. Burger, F. Schmidt, and M. Wegener, *Photonic metamaterials: Magnetism at optical frequencies*, invited paper, IEEE J. Sel. Top. Quant. **12**, 1097 (2006).
- G. Dolling, M. Wegener, A. Schädle, S. Burger, and S. Linden, *Observation of magnetization waves in negative-index photonic metamaterials*, Appl. Phys. Lett. **89**, 231118 (2006).
- G. Dolling, S. Linden, and M. Wegener, *Metamaterialien: Licht im Rückwärtsgang*, invited paper, Phys. Unserer Zeit **37**, 157 (2006).
- G. Dolling, C. Enkrich, M. Wegener, C. M. Soukoulis, and S. Linden, *Low-loss negative-index metamaterial at telecommunication wavelengths*, Opt. Lett. **31**, 1800 (2006).

- G. Dolling, C. Enkrich, M. Wegener, C. M. Soukoulis, and S. Linden, *Simultaneous Negative Phase and Group Velocity of Light in a Metamaterial*, Science **312**, 892 (2006).
- G. Dolling, M. Wegener, S. Linden, and C. Hormann, *Photorealistic images of objects in effective negative-index materials*, Opt. Express **14**, 1842 (2006).
- G. Dolling, C. Enkrich, M. Wegener, J. F. Zhou, C. M. Soukoulis, and S. Linden, *Cut-wire pairs and plate pairs as magnetic atoms for optical metamaterials*, Opt. Lett. **30**, 3198 (2005).

At international conferences and workshops (only own presentations):

- G. Dolling, M. Wegener, C. M. Soukoulis, and S. Linden, *Negative-index metamaterials have reached the visible*, invited talk, Progress In Electromagnetics Research Symposium (PIERS), Beijing, China, March 26-30, 2007.
- G. Dolling, *Negative-index metamaterials have reached the visible*, invited talk, Workshop on Nano-Photonics, Berlin, Germany, October 18-20, 2006.
- G. Dolling, C. Enkrich, M. Wegener, C. M. Soukoulis, and S. Linden, *From "Magnetic Atoms" to Low-Loss Negative-Index Metamaterials at Telecommunication Wavelengths*, talk QWE3, Quantum Electronics and Laser Science Conference (QELS), Long Beach, CA, U.S.A., May 21-26, 2006.

Contents

Zusammenfassung

Elektromagnetische Wellen sind ein wesentlicher Bestandteil unseres Alltags: Das menschliche Auge reagiert beispielsweise so auf das Licht, dass wir unsere Umgebung wahrnehmen können. Die Bildentstehung basiert dabei auf der Brechung von Lichtstrahlen: Wenn eine elektromagnetische Welle auf eine Grenzfläche zwischen zwei Medien mit unterschiedlichen Brechungsindizes trifft, wird die Welle gebrochen und ändert ihre Ausbreitungsrichtung. Durch diesen Effekt kann Licht fokussiert und somit Objekte abgebildet werden. Ähnlich wird in modernen Mikroskopen und Teleskopen die Brechung ausgenutzt, um den Mikrokosmos oder weit entfernte Galaxien zu studieren. Neben der Brechung spielt heutzutage jedoch auch die Reflexion von elektromagnetischen Wellen eine wichtige Rolle: Unsere moderne Telekommunikation basiert beispielsweise häufig auf Glasfaserkabeln. In diesen Kabeln wird das Licht durch Totalreflexion zwischen zwei Medien mit unterschiedlichen Brechungsindizes geführt. Die genannten Beispiele und Phänomene basieren alle auf dem Brechungsindex und der resultierenden Brechung und Reflexion von Licht.

Das Konzept des Brechungsindexes beruht dabei auf der Tatsache, dass die Wellenlänge des Lichts (einige hundert Nanometer) viel größer als typische Größenskalen (unter einem Nanometer bei Atomen) in natürlichen Materialien ist. Aus diesem Grund kann eine elektromagnetische Welle die feinen Details (zum Beispiel Atome) im Material nicht auflösen. Dieser Umstand vereinfacht die Beschreibung der Wechselwirkung zwischen Licht und dem Material erheblich: Wir müssen nur den Brechungsindex n des Materials oder, um genau zu sein, die (elektrische) Permittivität ε und die (magnetische) Permeabilität μ kennen. Die Permittivität beschreibt dabei die Wechselwirkung zwischen dem Material und dem elektrischen Feld der Welle, während die Permeabilität die Wechselwirkung des Materials mit dem magnetischen Feld der Welle beschreibt. In der Natur existieren jedoch keine Materialien mit $\mu \neq 1$ bei optischen Frequenzen, so dass nur die Permittivität beziehungsweise der Brechungsindex der wichtige Parameter in der Optik ist. Diese Tatsache wird zudem durch die bekannte Formel für den Brechungsindex wiedergegeben: $n = +\sqrt{\varepsilon}$. Trotzdem existieren viele Anwendungen bei optischen Frequenzen, obwohl natürliche Materialien nur eine Manipulation des elektrischen Feldes des Lichtes ermöglichen. Die Beeinflussung des elektrischen Feldes in der Optik ist jedoch so, als würde man nur eines seiner beiden Augen verwenden.

Im Jahr 1967 beschäftigte sich Victor Veselago mit der Frage, was passieren würde, wenn die Permeabilität von eins verschieden wäre. Er fand heraus, wenn sowohl die Permeabilität und die Permittivität negativ sind, dass dann auch der Brechungsindex negativ werden würde. In solchen Medien wären die Doppler-Verschiebung und die Cherenkov-

Strahlung umgekehrt. Trotz der interessanten Effekte blieb seine Idee eine Sonderlichkeit, da keine natürlichen Materialien mit $\mu \neq 1$ oberhalb von Gigahertz Frequenzen oder höher bekannt waren. Daher war es eine faszinierende Idee, als Sir John Pendry im Jahr 1999 künstliche Materialien vorschlug, die $\mu \neq 1$ aufweisen können. Seine Idee basiert dabei auf einem einfachen LC Schwingkreis: Ein Draht wird so gebogen, dass dieser eine Spule mit nur einer Windung formt. Die Enden des Drahtes bilden die Kapazität. Diese Struktur wird split-ring resonator (SRR) genannt und weist eine LC Resonanz auf. Es ist bekannt, dass der Stromfluss bei der Resonanzfrequenz resonant erhöht ist. Dieser oszillierende Strom führt zu einem oszillierenden magnetischen Dipolmoment. Viele dieser resonanten Elemente, die in einer periodischen Anordnung dicht gepackt werden, bilden ein künstliches Material, genannt Metamaterial. In der Optik werden diese Elemente durch das elektrische oder das magnetische Feld des Lichts angeregt. Da die relevante Wellenlänge viel größer als die einzelnen Elemente ist, spürt das Licht nur eine effektive Antwort ganz analog zu natürlichen Materialien. Mit diesen funktionellen Elementen oder auch "magnetischen Atomen" ist es möglich eine Permeabilität zu erhalten, die von eins abweicht oder sogar negativ wird. In Kombination mit natürlichen Materialien, die eine negative Permittivität aufweisen, lässt sich somit ein negativer Brechungsindex realisieren.

Auf der Idee von Pendry basierend haben wir Metamaterialien hergestellt, die einen negativen Brechungsindex aufweisen. Dabei haben wir die linear optischen Eigenschaften dieser Materialien bei optischen und sichtbaren Frequenzen sowohl in Experimenten als auch in der Theorie untersucht. Wir haben ein so genanntes Fischnetz-Metamaterial verwendet, welches aus (i) "elektrischen Atomen", die zu $\varepsilon < 0$ führen, und (ii) "magnetischen Atomen", die zu $\mu < 0$ führen, besteht: (i) Die elektrischen Atome werden durch lange und dünne Metalldrähte repräsentiert, die parallel zum einfallenden elektrischen Feld orientiert sind. Ihr Verhalten ist das eines verdünnten Metalls mit einer Plasmafrequenz, die kleiner als die eines Volumenmetalls ist. (ii) Die Resonanzwellenlänge der magnetischen Atome wird durch die Länge von Doppeldrähten oder Doppelplatten vorgegeben. Das magnetische Dipolmoment stammt von der antisymmetrischen Eigenmode des Stroms in den zwei gekoppelten Metalllagen. Jede Lage kann dabei als eine Halbwellenantenne angesehen werden. Durch die Kombination der beiden Atomsorten ist es möglich, in einem Frequenzintervall sowohl eine negative Permittivität als auch eine negative Permeabilität zu erhalten. Damit ist auch ein negativer Brechungsindex realisierbar.

Bevor wir uns jedoch Experimenten widmeten, haben wir die Physik des Brechungsindexes und das Phänomen der Brechung untersucht. Mit einem Ray-Tracing Programm wie POV-Ray lässt sich zum Beispiel das Verhalten von isotropen Materialien mit einem bestimmten Brechungsindex n simulieren. Für den Fall $n < 0$ erscheinen Strahlen zur "falschen" Seite gebrochen. Dies führt dazu, dass beispielsweise einfache Szenen wie ein Trinkglas mit einer Flüssigkeit sehr kompliziert werden, wenn die Flüssigkeit einen Brechungsindex von $n < 0$ hat: Objekte erscheinen zerrissen, man kann um die Ecke sehen und viele weitere ungewöhnliche Effekte treten auf. Daher ist es natürlich, den Brechungsindex mit dem Phänomen der Brechung an einer Grenzfläche zu verbinden. Wir haben jedoch gezeigt, dass der Brechungsindex im Allgemeinen nur die Geschwindigkeit beschreibt, mit der sich Fronten konstanter Phase einer Welle in einem Medium im Vergleich zu Vakuum

ausbreiten. Um diesen Aspekt zu verdeutlichen, haben wir Beispiele präsentiert, bei denen negative Brechung auftritt, obwohl alle Brechungsindizes positiv sind. Für ein anisotropes Medium wie Kalkspat kann man zum Beispiel sowohl negative als auch positive Brechung in Abhängigkeit vom Einfallswinkel erhalten. Außerdem zeigen sogar dünne, isotrope und homogene Schichten negative Brechung. Die Physik der negativen Brechung beruht dabei auf dem Verhalten vom Poynting Vektor an einer Grenzfläche, da dieser die Ausbreitungsrichtung der Energie beschreibt. Der Poynting Vektor ist jedoch nicht direkt mit dem Brechungsindex verknüpft, womit eine negative Brechung nicht notwendigerweise mit einem negativen Brechungsindex verbunden ist.

Bevor wir Metamaterialien hergestellt haben, haben wir die Strukturen immer mittels verschiedener numerischer Methoden auf bestimmte Eigenschaften optimiert. Aus den numerischen Simulationsdaten lassen sich die effektiven Materialparameter ausrechnen: die Permittivität, die Permeabilität und der Brechungsindex. Für das Fischnetz-Design haben wir den Einfluss der Lochform auf den Brechungsindex und die resultierende Verluste untersucht. Wir haben gezeigt, dass rechteckige Löcher dabei geringere Verluste als runde Löcher bei einer Wellenlänge von 1.5 µm aufweisen.

Alle Proben wurden mittels der Elektronenstrahllithographie hergestellt. Während des Prozesses wird ein Fotolack strukturiert, welcher als Maske in einem folgenden Aufdampfprozess diente. Auf das Substrat wurden dabei verschiedene Metalle und/oder Dielektrika aufgedampft. Elektronenstrahllithographie bietet die Möglichkeit, hochqualitative Strukturen auf einer Nanometerskala herzustellen. Diese genaue Methode ist unverzichtbar, da unsere funktionellen Elemente kleiner als die relevante Wellenlänge sein müssen – für sichtbares Licht müssen die funktionellen Elemente bereits kleiner als einige hundert Nanometer sein. Die Elektronenstrahlverdampfung der verschiedenen Materialien für unsere Metamaterialien ist wichtig, da wir hochwertige Filme benötigen.

Um einen negativen Brechungsindex und damit eine negative Phasengeschwindigkeit messen zu können, haben wir ein Michelson Interferometer aufgebaut. Wir haben 170 fs optische Pulse um 1.5 µm Wellenlänge oder 125 fs Pulse um 800 nm Wellenlänge in Abhängigkeit von der relevanten Wellenlänge des Metamaterials verwendet. Dies hat uns ermöglicht, sowohl die Phasengeschwindigkeit als auch die Gruppengeschwindigkeit zu messen. Wir haben eine negative Phasengeschwindigkeit in einem Metamaterial um 1.5 µm Wellenlänge nachweisen können. Weiterhin haben wir einen spektralen Bereich gefunden, in dem die Gruppengeschwindigkeit negativ ist. Das bedeutet, dass das Maximum der Einhüllende des auslaufenden Pulses das Metamaterial verlässt, bevor das Maximum der Einhüllenden des zugehörigen einlaufenden Pulses in das Metamaterial eintritt. Dies ist jedoch im Einklang mit der Kausalität, da Pulsverformungen in der Probe bedeutend sind. In unserem Experiment haben wir zusätzlich einen spektralen Bereich gefunden, in dem sowohl die Phasengeschwindigkeit als auch die Gruppengeschwindigkeit gleichzeitig negativ sind. Diese Kombination wurde zum ersten Mal experimentell bei optischen Frequenzen nachgewiesen.

In der nächsten Generation von Proben haben wir Silber anstatt von Gold als Metall für unsere Metamaterialien verwendet. Silber hat den Vorteil von geringeren Verlusten im Vergleich zu Gold. Wir haben eine Struktur sorgfältig daraufhin optimiert, eine möglichst große figure of merit (FOM) aufzuweisen. Die FOM ist definiert als negatives Verhältnis

von Realteil und Imaginärteil des Brechungsindexes: $\mathrm{FOM} = -\mathrm{Re}(n)/\mathrm{Im}(n)$. Aktuelle Metamaterialien bei optischen Frequenzen hatten nur Werte von $\mathrm{FOM} < 1$ gezeigt, was bedeutet, dass der Imaginärteil den entsprechenden Realteil des Brechungsindexes dominiert. Wir haben erfolgreich ein Metamaterial mit $\mathrm{FOM} \approx 3$ hergestellt. Dieser Wert übersteigt die FOM des ersten Metamaterials, welches einen negativen Brechungsindex bei optischen Wellenlängen zeigte, um das 30-fache. Unsere hohe FOM ist zudem mit einem fast transparentem Metamaterial verbunden – mehr als 60% Transmission in einem spektralen Bereich mit $\mathrm{Re}(n) < 0$.

Außerdem haben wir die Wechselwirkungseffekte zwischen den funktionellen Elementen von unserem Metamaterial untersucht. In vorherigen Diskussion beruhten die optischen Eigenschaften auf den optischen Eigenschaften der individuellen Elemente. Geht man einen Schritt weiter, so führen elektrische Dipol-Dipol und magnetische Dipol-Dipol Wechselwirkungen zwischen den nächsten Nachbarn (und weiter) zu einer Kopplung der photonischen Atome. Um diese Interaktion aufzuklären, haben wir winkelaufgelöste Transmissionsmessungen durchgeführt. Dieses Vorgehen erlaubt es uns, die Dispersionsrelation in der Ebene der Atome zu messen. Wir haben herausgefunden, dass die magnetischen und elektrischen Wechselwirkungen sehr von dem Wellenvektor in der Ebene abhängen. Von der Geometrie und der Form der Dispersionsrelation haben wir darauf geschlossen, dass die Kopplung hauptsächlich durch magnetische Dipole gegeben ist, wenn die Welle entlang der magnetischen Dipole läuft. Diese Magnetisierungswellen sind das klassische Analogon von Magnonenanregungen der quantenmechanischen Spins. Wenn wir in den Simulationen die elektrischen Atome komplett entfernt haben, zeigen sich kaum Änderungen in den Transmissionsspektren für verschiedene Wellenvektoren in der Ebene. Diese Beobachtung weist darauf hin, dass die elektrischen Atome sowohl die starke elektrische also auch die starke magnetische Dipol-Dipol Wechselwirkung vermitteln. Weiterhin offenbart es, dass Änderungen im Spektrum nicht alleine eine Eigenschaft der isolierten magnetischen Atome ist.

Um einen negativen Brechungsindex im sichtbaren Spektralbereich zu realisieren, haben wir die funktionellen Elemente unseres Metamaterials weiter verkleinert. Die zugehörige Probe zeigt minimale laterale Features von 68 nm bei einer Dicke von 97 nm des Metamaterials. Das Aspektverhältnis ist somit größer als eins, was bereits große fabrikationstechnische Herausforderungen darstellt. Durch den Vergleich zwischen Transmissions-, Reflexions- und phasensensitiven Messungen mit theoretischen Rechnungen haben wir auf einen Realteil des Brechungsindexes von $\mathrm{Re}(n) = -0.6$ bei einer Wellenlänge von 780 nm – eine Wellenlänge, die im Labor deutlich sichtbar ist – mit $\mathrm{FOM} \approx 0.5$ geschlossen. Dieses Metamaterial ist das Erste gewesen, welches einen negativen Brechungsindex im sichtbaren Spektralbereich aufweist.

Alle Untersuchungen und vorherigen Diskussionen über Metamaterialen mit einem negativen Brechungsindex bei optischen Wellenlängen basierten auf nur einer funktionellen Lage. Es ist jedoch beispielsweise von kristallinen Festkörpern bekannt, dass die Oberfläche oder eine Monolage andere Eigenschaften als ein Volumenmaterial aufweisen kann. Aus diesem Grund haben wir untersucht, ob die optischen Eigenschaften einer einzelnen funktionellen Lage denen von vielen Lagen entsprechen. Dafür haben wir Proben mit einer, zwei und drei funktionellen Lagen hergestellt. Für alle drei Proben haben wir einen negativen

Brechungsindex erhalten. Für drei funktionelle Lagen haben wir beispielsweise eine Transmission von über 60% bei einer Wellenlänge von 1.44 µm festgestellt, bei der wir auch einen negativen Realteil des Brechungsindexes erhielten. Wir haben gezeigt, dass die optischen Eigenschaften der unterschiedlichen Proben dabei kaum von der Anzahl der Lagen abhängen. Die experimentellen Daten wurden sehr gut durch entsprechende numerische Rechnungen reproduziert.

Im Allgemeinen bieten photonische Metamaterialien die Möglichkeit, optische Eigenschaften zu erhalten, die nicht in natürlichen Materialien auftreten. In dieser Arbeit haben wir einen negativen Brechungsindex bei optischen Frequenzen erhalten und neue Effekte untersucht. In der Zwischenzeit wurden Ideen präsentiert, wie man mit Hilfe von Metamaterialien zum Beispiel perfekte Abbildungen erzeugen und Objekte unsichtbar machen kann. Bei optischen Frequenzen basieren die Metamaterialien jedoch noch auf fast planaren Strukturen. Gerade für Anwendungen sind jedoch echt dreidimensionale, isotrope Strukturen mit einem negativen Brechungsindex bei optischen Frequenzen interessant. Bis dahin ist es noch ein weiter Weg, jedoch wurden die ersten Schritte unternommen. Das Feld der Optik und Photonik hat sich bereits beträchtlich durch die erweiterten Möglichkeiten von photonischen Metamaterialien geändert. Weitere spannende Entdeckungen können erwartet werden.

Chapter 1

Introduction

Electromagnetic waves govern our daily life: For example, the human eye reacts to light such that we are able to observe our environment. The imaging process of the human eye is based on refraction: If an electromagnetic wave impinges on an interface between two media with different refractive indices, the wave is refracted and changes its direction of propagation. With this effect, light can be focussed, meaning for example that objects can be imaged, as in the case of our eye. Similarly, modern microscopes and telescopes employ the phenomenon of refraction in order to study the microcosmos or galaxies which are far away. Besides refraction, also the reflection of electromagnetic waves plays an important role today: Modern telecommunication, for example, is often based on optical fibers. In these fibers, light is guided owing to the total internal reflection between media with different refractive indices. These examples and phenomena make use of the refractive index and the refraction of light.

The concept of the refractive index n is based on the fact that the wavelength of light (several hundreds of nanometers) is much larger than the distance between the atoms and their individual size (below one nanometer). As a consequence, an electromagnetic wave cannot resolve the fine details, i.e., the atoms, of a material. This aspect simplifies the description of the interaction between a wave and a material: We simply have to know the refractive index n, or, to be precise, the (electric) permittivity ε and the (magnetic) permeability μ. Here, the permittivity describes the interaction of the material with the electric field of the wave, while the permeability describes the interaction of the material with the magnetic field of the wave. However, in nature, materials with $\mu \neq 1$ do not exist at optical wavelengths and hence only the permittivity or the refractive index is the important parameter in optics. This fact is also reflected in the well-known formula for the refractive index: $n = +\sqrt{\varepsilon}$. Manifold applications are found although, at optical frequencies, natural substances allow for the manipulation of the electric field of an electromagnetic wave only. However, manipulating just the electric field in optics is like using just one of two eyes.

In 1967, Victor Veselago dealt with the question what might happen if the permeability differed from one [1]. He found that for negative values of both the permeability and the permittivity the refractive index would become negative as well. In such media, the Doppler shift and the Cherenkov radiation would be reversed. Furthermore, a wave impinging onto

such a medium would be refracted to the "wrong" side. Despite these interesting effects, Veselago's idea remained obscure, since natural substances with $\mu \neq 1$ were not known for gigahertz frequencies and higher. So it was a fascinating idea when in 1999 Sir John Pendry proposed artificial materials which can exhibit $\mu \neq 1$ [2]. His idea is based on a simple LC circuit: A wire is bent such that it forms a coil with only one winding. The ends of the wire form a capacitor. This structure is called split-ring resonator (SRR) and exhibits an LC resonance. From basic circuit theory, it is well known that the current flow is resonantly enhanced at the specific resonance frequency. This oscillating current generates an oscillating magnetic dipole moment. Many resonant circuits, densely packed in a periodic lattice, form an artificial material called metamaterial. In optics, the resonant circuits are excited by the electric or the magnetic field of the incoming wave. Since the relevant wavelength is much larger than the resonant elements, the wave experiences an effective response just as in the case of natural substances. With these functional elements or "magnetic atoms" it is possible to achieve a permeability different from one or even a negative value.

Pendry's idea has triggered the development and the fabrication of metamaterials with a negative refractive index since it was possible to modify both the permittivity and the permeability. In 2001 for the first time, negative refraction was demonstrated in an experiment [3] utilizing a composite structure made of split-ring resonators as magnetic atoms and a diluted metal with a negative permittivity below its plasma frequency as electric atoms. In this experiment, Smith *et al.* showed negative refraction of a beam of microwaves impinging onto the metamaterial. The negative refractive index occurred at wavelengths of a few centimeters. This eased the fabrication of the first negative-index metamaterial, since the functional elements were on the order of millimeters.

Besides the very interesting aspect of a negative permeability, Pendry developed the idea of the "perfect lens" [4]. This lens just consists of a slab with a refractive index of $n = -1$. He found that a point source in front of the slab would be perfectly imaged at the rear side of the slab, i.e., the image is not limited by diffraction. He also showed that a thin metal slab with $\varepsilon = -1$ can act as a perfect lens in electrostatics. The latter is easier to fabricate. Indeed, in 2004, a group [5] verified this prediction experimentally by creating an image with a resolution better than the diffraction limit using a thin silver film. A fine-structured object was imaged by a $35\,\mathrm{nm}$ silver film into a photoresist using light of a wavelength of $\lambda = 365\,\mathrm{nm}$. In the developed photoresist, details of $60\,\mathrm{nm}$, corresponding to about $\lambda/6$, were resolved.

Another possible application for metamaterials was developed independently by Pendry [6] and Leonhardt [7] at the same time in 2006: cloaking, i.e., hiding objects from a viewer. Only five months later, Smith *et al.* [8] demonstrated how to exploit this idea experimentally. They achieved almost complete cloaking of a copper cylinder at microwave frequencies. Another application for metamaterials is given by an alternating layer sequence consisting of materials with positive and negative refractive indices, respectively, which can show a three-dimensional photonic bandgap [9]. Only one year later, this behavior could be experimentally demonstrated for microwaves [10].

The ideas of Pendry and other scientists and the first experimental demonstration of negative-index metamaterials served as the starting point for the fast development in the

field of metamaterials, especially metamaterials that exhibit a permeability different from one or even exhibit a negative refractive index. Up to the year 2004 [11], all metamaterials operated at microwave frequencies only. This frontier was overcome by different groups presenting a metamaterial with a negative permeability operating at terahertz [12] or even optical frequencies [13]. At this time, metamaterials with $\mu \neq 1$ entered optics for the first time. In this thesis, we extend the frequencies for a negative refractive index to the visible [14] – today's world record – and we present new aspects of metamaterials with a negative refractive index at optical frequencies.

In a time span of only eight years, the field of metamaterials developed from a single idea to a rapidly growing field in science. Many new opportunities are found in optics. This rapid development stems from the fact that photonic metamaterials offer the possibility to tailor optical properties which do not occur in natural substances. However, today's metamaterials operating at optical frequencies are limited to two-dimensional structures. It is still a long way to go for truly three-dimensional isotropic negative-index metamaterials at optical frequencies. The field of optics & photonics has already changed considerably by the enlarged possibilities offered by photonic metamaterials. Further exciting discoveries are to be expected and further ideas are necessary to exploit all possibilities. We have just started to use our second eye in optics.

Outline of this thesis

In chapter 2, we review the fundamentals of linear optics with a permeability μ unequal to unity. Furthermore, we discuss possible applications. We describe values which the permittivity and the permeability can obtain in nature at optical frequencies. We briefly introduce some possible realizations of metamaterials which exhibit a negative permeability or even a negative refractive index. In chapter 3, we discuss some physical aspects of refraction and refractive indices and the resulting problems.

In chapter 4, we introduce the methods used for fabricating our negative-index metamaterial samples. Furthermore, we describe the setups to characterize our fabricated samples optically. At the end of the chapter, we deal with the different numerical methods.

The route from materials with a negative permeability to a negative refractive index material is described in chapter 5. Furthermore, we explain in detail the "double-fishnet" structure which is used in our experiments.

The experimental results are presented in chapter 6. First, we study the results obtained on a negative-index metamaterial. We find simultaneous negative phase and group velocities in a spectral range in which the refractive index is negative. We briefly describe the theory of negative group velocities and proceed with the experimental results obtained by a low-loss negative-index metamaterial which has the lowest losses for optical negative-index metamaterials to date. We continue with a presentation of a metamaterial with a negative refractive index at the red end of the visible spectrum. Afterwards, we investigate the double-fishnet structure for oblique incidence of light. We end this chapter with a comparison of metamaterials with a different number of lattice constants – one, two, or three functional layers – in the propagation direction of the light. Finally, we conclude in chapter 7.

Chapter 2

Fundamentals of linear optics

Maxwell's equations form the basis of optics. In their general form, they characterize, among other equations, the interaction of electromagnetic waves and matter. Two important parameters for this interaction are the permittivity describing the electric interaction and the permeability describing the magnetic interaction. However, many standard text books on optics, e.g. [15], neglect the permeability. They assume $\mu = 1$ for optical frequencies and investigate the role of the permittivity. However, plenty of applications are found in optics.

In section 2.1, we assume arbitrary values of permeability and permittivity, which lead to notable modifications of the actually well-known formulas of optics. For instance, we obtain a negative refractive index. Subsequently, we focus on some of the resulting effects. Using ray optics, we discover the extraordinary properties of a material with a negative refractive index. Furthermore, achieving a permeability different from unity would also provide the opportunity to cloak objects from electromagnetic radiation.

In section 2.2, we deal with the important question of how to realize $\mu \neq 1$. First, we investigate the values which both the permittivity and permeability can have in natural materials. While one can find arbitrary values for the permittivity in optics, there are no natural materials available with $\mu \neq 1$ at optical frequencies.

However, today's technology provides the opportunity to fabricate artificial composite structures (so called metamaterials), which can show a permeability unequal to one for optical frequencies. A general overview of already fabricated structures and their performance is given at the end of this chapter (section 2.3).

2.1 Electromagnetic wave propagation

2.1.1 Maxwell's equations

The propagation of electromagnetic waves is characterized by Maxwell's equations (in SI units) [16]:

$$\nabla \cdot \boldsymbol{D} = \rho, \tag{2.1}$$

$$\nabla \cdot \boldsymbol{B} = 0, \tag{2.2}$$

$$\nabla \times \boldsymbol{E} = -\frac{\partial \boldsymbol{B}}{\partial t}, \tag{2.3}$$

$$\nabla \times \boldsymbol{H} = \boldsymbol{j} + \frac{\partial \boldsymbol{D}}{\partial t}, \tag{2.4}$$

with the following notations and units:

- $\boldsymbol{E}$ electric field, $[\boldsymbol{E}] = \mathrm{V\,m^{-1}}$,
- $\boldsymbol{D}$ electric displacement, $[\boldsymbol{D}] = \mathrm{As\,m^{-2}}$,
- $\boldsymbol{H}$ magnetic induction, $[\boldsymbol{H}] = \mathrm{A\,m^{-1}}$,
- $\boldsymbol{B}$ magnetic field, $[\boldsymbol{B}] = \mathrm{Vs\,m^{-2}}$,
- ρ free electric charge density, $[\rho] = \mathrm{As\,m^{-3}}$,
- $\boldsymbol{j}$ free electric current density, $[\boldsymbol{j}] = \mathrm{A\,m^{-2}}$,
- ε_0 absolute electric permittivity of vacuum: $\varepsilon_0 = 8.8542 \cdot 10^{-12}\,\mathrm{As\,V^{-1}\,m^{-1}}$,
- μ_0 absolute magnetic permeability of vacuum: $\mu_0 = 4\pi \cdot 10^{-7}\,\mathrm{Vs\,A^{-1}\,m^{-1}}$.

Furthermore, the relation between the electric field and the electric displacement and the relation between the magnetic field and the magnetic induction are given by the material equations:

$$\boldsymbol{D} = \varepsilon_0 \boldsymbol{E} + \boldsymbol{P}, \tag{2.5}$$

$$\boldsymbol{B} = \mu_0 \left(\boldsymbol{H} + \boldsymbol{M}\right). \tag{2.6}$$

$\boldsymbol{P}$ is the electric polarization ($[\boldsymbol{P}] = \mathrm{As\,m^{-2}}$) and $\boldsymbol{M}$ is the magnetization ($[\boldsymbol{M}] = \mathrm{Vs\,m^{-2}}$). In general, the electric polarization $\boldsymbol{P} = \boldsymbol{P}(\boldsymbol{E}, \boldsymbol{B})$ and the magnetization $\boldsymbol{M} = \boldsymbol{M}(\boldsymbol{E}, \boldsymbol{B})$ are unknown. However, since we consider only small electric fields in this thesis, we can expand $\boldsymbol{P}$ in power series and neglect all terms of higher order than the linear term, which motivates the nomenclature of *linear* optics. Additionally, the dependence of $\boldsymbol{P}$ on $\boldsymbol{B}$ is neglected. With these simplifications, the linear response function is generally given by:

$$\boldsymbol{P}(\boldsymbol{r}, t) = \varepsilon_0 \int_{-\infty}^{+\infty} \int_{-\infty}^{+\infty} \chi_e\left(\boldsymbol{r}, \boldsymbol{r}', t, t'\right) \boldsymbol{E}(\boldsymbol{r}', t')\, \boldsymbol{dr}'\, dt'. \tag{2.7}$$

Here, χ_e is the electric susceptibility which characterizes the linear response of the material to an external electric field. Generally, χ_e is a tensor of second order. However, in the case of isotropic media, χ_e can be set to be a scalar quantity, which is already applied in (2.7). Due to the homogeneity of time, χ_e has no explicit time dependence, leading to $\chi_e(\boldsymbol{r}, \boldsymbol{r}', t, t') \rightarrow \chi_e(\boldsymbol{r}, \boldsymbol{r}', t - t')$. Furthermore, we assume that the size of the building blocks is much smaller than the relevant wavelengths. This assumption is known as dipole approximation and simplifies the response function further to $\chi_e(\boldsymbol{r} - \boldsymbol{r}', t - t')$. Since we are only interested in a local response of the material, we get: $\chi_e(\boldsymbol{r} - \boldsymbol{r}', t - t') \rightarrow \chi_e(t - t')$. Due to causality, the response can appear only after the stimulus: $\chi_e(t - t') \equiv 0$ for $t' > t$. With all these assumptions, the Fourier transformation of (2.7) yields

$$\boldsymbol{P}(\boldsymbol{r}, \omega) = \varepsilon_0\, \chi_e(\omega) \boldsymbol{E}(\boldsymbol{r}, \omega).$$

Analogously, one can derive the following equation for the magnetization:

$$\boldsymbol{M}(\boldsymbol{r}, \omega) = \chi_m(\omega) \boldsymbol{H}(\boldsymbol{r}, \omega).$$

Here, χ_m is the magnetic susceptibility which describes the linear response of the material to an external magnetic field. Thus, (2.5) and (2.6) can be written as

$$\boldsymbol{D}(\boldsymbol{r},\omega) = \varepsilon_0\,(1+\chi_e(\omega))\,\boldsymbol{E}(\boldsymbol{r},\omega) = \varepsilon_0\,\varepsilon(\omega)\boldsymbol{E}(\boldsymbol{r},\omega), \tag{2.8}$$

$$\boldsymbol{B}(\boldsymbol{r},\omega) = \mu_0\,(1+\chi_m(\omega))\,\boldsymbol{H}(\boldsymbol{r},\omega) = \mu_0\,\mu(\omega)\boldsymbol{H}(\boldsymbol{r},\omega) \tag{2.9}$$

with the (relative) electric permittivity $\varepsilon(\omega)$ and the (relative) magnetic permeability $\mu(\omega)$.

2.1.2 Refractive index

From Maxwell's equations we can derive the wave equation for the electric field in a homogeneous medium:

$$\left(\Delta - \mu_0\varepsilon_0\,\frac{\partial^2}{\partial t^2}\mu\varepsilon\right)\boldsymbol{E} = 0. \tag{2.10}$$

In order to solve equation (2.10) the most general ansatz is given by $\boldsymbol{E}(\boldsymbol{r},t) = \boldsymbol{E}_0\,f(\boldsymbol{kr} - \omega t)$. This ansatz can be simplified by applying specific restrictions, yielding for example the plane wave solution with $\boldsymbol{E}(\boldsymbol{r},t) = \boldsymbol{E}_0\,\exp[\mathrm{i}(\boldsymbol{kr}-\omega t)] + \mathrm{c.c.}$ Inserting this ansatz in (2.10) we obtain:

$$\boldsymbol{k}\cdot\boldsymbol{k} = \mu\varepsilon\omega^2\,\mu_0\varepsilon_0 = n^2\frac{\omega^2}{c_0^2} = n^2\boldsymbol{k}_0^2. \tag{2.11}$$

Here, $c_0 = 1/\sqrt{\mu_0\varepsilon_0}$ is the velocity of light in vacuum, $\boldsymbol{k}_0$ is the vacuum wave vector, and

$$n(\omega)^2 = \mu(\omega)\varepsilon(\omega) \tag{2.12}$$

the square of the refractive index. For real-valued refractive indices the phase velocity is given by

$$v_{\mathrm{ph}} = \frac{c_0}{n} \tag{2.13}$$

The direction of the phase velocity is defined to be parallel to the wave vector $\boldsymbol{k}$. Obviously, by using equation (2.13), the refractive index primarily describes the factor by which the phase velocity is faster or slower in the medium than the velocity of light in vacuum. Taking the complex square root of (2.12) and rewriting its result according to [17], we obtain

$$n = \sqrt{|\varepsilon|\cdot|\mu|}\exp\left[+\frac{\mathrm{i}}{2}\left(\operatorname{arccot}\frac{\varepsilon_{\mathrm{R}}}{\varepsilon_{\mathrm{I}}} + \operatorname{arccot}\frac{\mu_{\mathrm{R}}}{\mu_{\mathrm{I}}}\right)\right]. \tag{2.14}$$

Here, ε_{R} and μ_{R} represent the real parts and ε_{I} and μ_{I} the imaginary parts of the respective functions. In formula (2.14) we have already taken into account that the refractive index can only adopt values belonging to the upper half of the complex plane given by $\mathrm{Im}(n) \geq 0$. If we allowed values with a negative imaginary part, a plane wave, for instance, would result in an exponential increase, which is physically forbidden in the case of passive materials. Thus, the solution can be determined unambiguously.

In Fig. 2.1, the electric permittivity and the magnetic permeability are derived from Lorentz oscillators (cf. chapter 2.2.1). It is clearly visible that the real part of the refractive index is negative in a certain frequency interval. We also note that $\mathrm{Re}(\varepsilon) < 0$ and

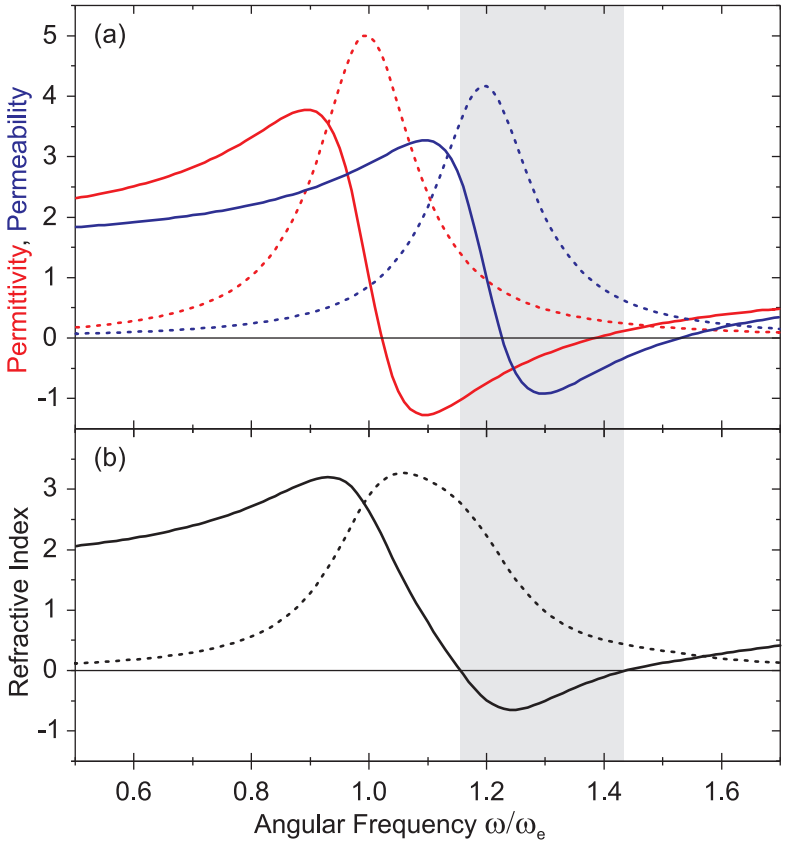

Figure 2.1: Optical constants for a model material consisting of Lorentz oscillators (cf. chapter 2.2.1). The parameters are: $\omega_{\mathrm{pl}} = \omega_{\mathrm{e}}$ and $\gamma = 0.2\omega_{\mathrm{e}}$, and $\omega_{\mathrm{m}} = 1.2\omega_{\mathrm{e}}$. (a) The electric permittivity (red) and the magnetic permeability (blue) are displayed with their real part (solid curves) and imaginary part (dashed curves). (b) The refractive index is calculated by using the functions in (a) and formula (2.14). The region with $\mathrm{Re}(n) < 0$ is depicted in grey. The imaginary parts are plotted with dashed lines.

$\mathrm{Re}(\mu) < 0$ do not represent a necessary constraint for obtaining a negative refractive index. This can be illustrated by rewriting the constraint for a negative refractive index:

$$\mathrm{Re}(n) < 0 \Leftrightarrow \varepsilon_{\mathrm{R}}\mu_{\mathrm{I}} + \varepsilon_{\mathrm{I}}\mu_{\mathrm{R}} < 0. \tag{2.15}$$

In order to obtain a negative refractive index, having the real parts of both the permittivity and the permeability negative is not a necessary constraint. Due to the imaginary parts of the respective functions, it can be sufficient to have only one of the real parts negative. However, considering Fig. 2.1, it becomes obvious that the ratio of real and imaginary part of n will be maximal if indeed both real parts are negative.

In the case of $\varepsilon = \mu = -1$ one is tempted to assume the refractive index as $n = \sqrt{(-1)\cdot(-1)} = 1$. However, applying formula (2.14) and approaching the limits $\varepsilon_{\mathrm{I}}, \mu_{\mathrm{I}} \to 0$ one obtains [17]:

$$n = \lim_{\varepsilon_{\mathrm{I}},\mu_{\mathrm{I}}\to 0} \exp\left[\frac{\mathrm{i}}{2}\left(\mathrm{arccot}\frac{-1}{\varepsilon_{\mathrm{I}}} + \mathrm{arccot}\frac{-1}{\mu_{\mathrm{I}}}\right)\right] = -1. \tag{2.16}$$

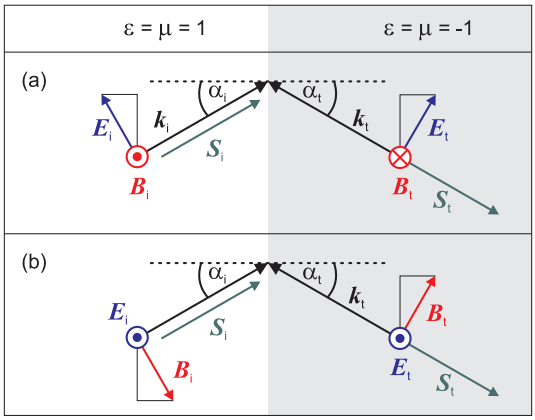

Figure 2.2: An electromagnetic wave impinging on an interface between vacuum and a material with $\varepsilon = \mu = -1$. Both p-polarization (a) and s-polarization (b) are depicted.

An important restriction results from the energy density w of the electromagnetic field, which in the case of transparent dispersive media is given by

$$w = \mathrm{Re}\left(\frac{\partial(\varepsilon\omega)}{\partial\omega}\right)|\boldsymbol{E}|^2 + \mathrm{Re}\left(\frac{\partial(\mu\omega)}{\partial\omega}\right)|\boldsymbol{H}|^2 \geq 0. \tag{2.17}$$

If both ε and μ were frequency independent and negative, the energy density would be negative. This is physically not reasonable.Hence, both functions have to be dispersive.

2.1.3 Refraction at an interface

After having analyzed the refractive index from the mathematical point of view in the previous section, we now turn our focus to the following example: an electromagnetic wave impinging on an interface between vacuum and a material with $\varepsilon = \mu = -1$. The impedance Z of the medium is defined by:

$$Z = \sqrt{\frac{\mu_0\mu}{\varepsilon_0\varepsilon}} = Z_0 \cdot \sqrt{\frac{\mu}{\varepsilon}}. \tag{2.18}$$

with $Z_0 \approx 377\Omega$ the impedance of vacuum . For physical reasons, one requires a positive real part of the impedance in passive media, since otherwise the energy conservation law would be violated, just like in the (previously discussed) case of a negative imaginary part of the refractive index [18]. This constraint determines the algebraic sign of the impedance. Thus, in the present case, the impedance of the medium equals exactly that of the vacuum. For this special case the electromagnetic wave is not reflected at the interface, as will be shown later. This fact simplifies the description of the refraction.

Using equation (2.1) and Gauss' theorem yields that the normal component of the electric displacement $D_\perp$ is continuous at the interface. Analogously, the same holds for the normal component of the magnetic field $B_{\perp,\mathrm{t}} = B_{\perp,\mathrm{i}}$. Here, $\perp$ denotes the vector component perpendicular to the interface and $||$ denotes the vector component parallel to the interface, respectively. The index i (t) corresponds to the incident (transmitted) wave. Applying

Stokes' theorem to equation (2.3) (and equation (2.4), respectively) yields the conservation of the tangential component of $E_{||,\mathrm{t}} = E_{||,\mathrm{i}}$ (and $H_{||,\mathrm{t}} = H_{||,\mathrm{i}}$, respectively) at the interface. The wave vector $\boldsymbol{k}$ can be derived from the relation $\boldsymbol{k} \times \boldsymbol{E} \parallel \boldsymbol{B}$ and equation (2.11). Furthermore, taking the material equations into account, we obtain all fields as plotted in Fig. 2.2.

One can clearly observe that in our material, the wave vector $\boldsymbol{k}$ points antiparallel to the Poynting vector $\boldsymbol{S} = \boldsymbol{E} \times \boldsymbol{H}$, i.e., $\boldsymbol{k}_\perp \cdot \boldsymbol{S}_\perp < 0$ and $\boldsymbol{k}_{||} \cdot \boldsymbol{S}_{||} < 0$. This means that the energy in both vacuum and medium propagates from left to right in Fig. 2.2, while in the medium with $\varepsilon = \mu = -1$ the phase velocity is opposite to the propagation direction of the energy. In this case, $\boldsymbol{S}$, $\boldsymbol{E}$, $\boldsymbol{B}$ form a left-handed system, which motivates the frequently used term *left-handed materials* for such a medium. This is not to be confused with the left-handedness of chiral materials.

Figure 2.2 also shows that the wave is refracted to the "wrong side". Snell's law is given by

$$\frac{\sin(\alpha_\mathrm{i})}{\sin(\alpha_\mathrm{t})} = \frac{n_\mathrm{i}}{n_\mathrm{t}}, \tag{2.19}$$

where α_i is the angle of incidence, α_t is the angle in the medium, and n_i and n_t are the respective refractive indices. Thus, the situation depicted in Fig. 2.2 can be described by simply applying a negative refractive index $n = -1$ to the medium with $\varepsilon = \mu = -1$, which is also consistent with all previous considerations.

Fresnel's equations

Using the conservation laws described in the previous section, we can calculate the amplitude reflection coefficient r and the amplitude transmission coefficient t at an interface [15]. For s-polarization we obtain:

$$r_\mathrm{s} = \left(\frac{E_{0\mathrm{r}}}{E_{0\mathrm{i}}}\right)_\mathrm{s} = \frac{\frac{n_\mathrm{i}}{\mu_\mathrm{i}}\cos\alpha_\mathrm{i} - \frac{n_\mathrm{t}}{\mu_\mathrm{t}}\cos\alpha_\mathrm{t}}{\frac{n_\mathrm{i}}{\mu_\mathrm{i}}\cos\alpha_\mathrm{i} + \frac{n_\mathrm{t}}{\mu_\mathrm{t}}\cos\alpha_\mathrm{t}} = \frac{Z_\mathrm{t}\cos\alpha_\mathrm{i} - Z_\mathrm{i}\cos\alpha_\mathrm{t}}{Z_\mathrm{t}\cos\alpha_\mathrm{i} + Z_\mathrm{i}\cos\alpha_\mathrm{t}}, \tag{2.20}$$

$$t_\mathrm{s} = \left(\frac{E_{0\mathrm{t}}}{E_{0\mathrm{i}}}\right)_\mathrm{s} = \frac{2\frac{n_\mathrm{i}}{\mu_\mathrm{i}}\cos\alpha_\mathrm{i}}{\frac{n_\mathrm{i}}{\mu_\mathrm{i}}\cos\alpha_\mathrm{i} + \frac{n_\mathrm{t}}{\mu_\mathrm{t}}\cos\alpha_\mathrm{t}} = \frac{2Z_\mathrm{t}\cos\alpha_\mathrm{i}}{Z_\mathrm{t}\cos\alpha_\mathrm{i} + Z_\mathrm{i}\cos\alpha_\mathrm{t}}. \tag{2.21}$$

Analogously, we derive for p-polarization:

$$r_\mathrm{p} = \left(\frac{E_{0\mathrm{r}}}{E_{0\mathrm{i}}}\right)_\mathrm{p} = \frac{\frac{n_\mathrm{t}}{\mu_\mathrm{t}}\cos\alpha_\mathrm{i} - \frac{n_\mathrm{i}}{\mu_\mathrm{i}}\cos\alpha_\mathrm{t}}{\frac{n_\mathrm{t}}{\mu_\mathrm{t}}\cos\alpha_\mathrm{i} + \frac{n_\mathrm{i}}{\mu_\mathrm{i}}\cos\alpha_\mathrm{t}} = \frac{Z_\mathrm{i}\cos\alpha_\mathrm{i} - Z_\mathrm{t}\cos\alpha_\mathrm{t}}{Z_\mathrm{i}\cos\alpha_\mathrm{i} + Z_\mathrm{t}\cos\alpha_\mathrm{t}}, \tag{2.22}$$

$$t_\mathrm{p} = \left(\frac{E_{0\mathrm{t}}}{E_{0\mathrm{i}}}\right)_\mathrm{p} = \frac{2\frac{n_\mathrm{i}}{\mu_\mathrm{i}}\cos\alpha_\mathrm{i}}{\frac{n_\mathrm{t}}{\mu_\mathrm{t}}\cos\alpha_\mathrm{i} + \frac{n_\mathrm{i}}{\mu_i}\cos\alpha_\mathrm{t}} = \frac{2Z_\mathrm{t}\cos\alpha_\mathrm{i}}{Z_\mathrm{i}\cos\alpha_\mathrm{i} + Z_\mathrm{t}\cos\alpha_\mathrm{t}}. \tag{2.23}$$

Here, r corresponds to the reflected wave. E_0 denotes the complex electric field amplitude. Standard text books on optics frequently assume $\mu = 1$, hence the Fresnel's equations are simplified and quoted only with dependency on the refractive index. Actually, to be more precise both the reflection and the transmission coefficients are characterized by the impedance, while the refractive index specifies only the phase velocity in a medium.

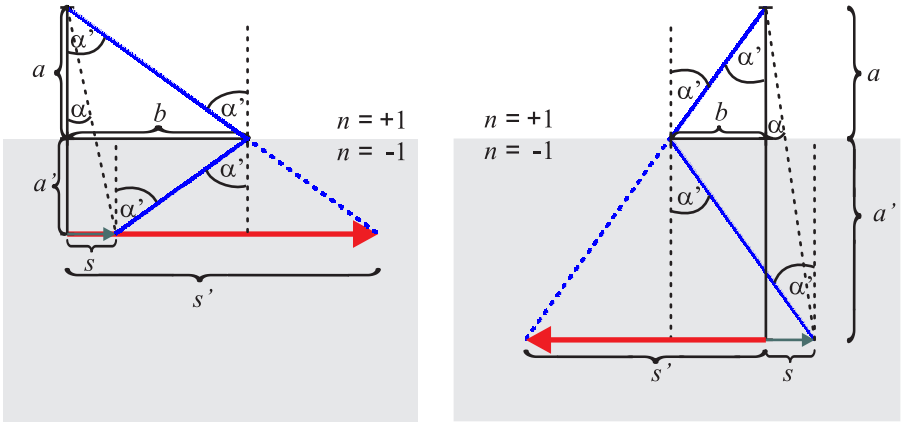

Figure 2.3: The depth dependence of the magnification factor s'/s for an object of size s in a material with $n = -1$ is illustrated. The observer looks straight down onto the arrow. The distance from the observer to the interface is a, the distance from the object to the interface is a'. (a) $a' < a$ and (b) $a' > a$.

2.1.4 Some examples for optics with $\mu \neq 1$

In this section we consider some examples of material with interesting optical properties arising from a permeability different from unity with special focus on negative-index materials.

Examples for ray optics

The first example we discuss is illustrated in Fig. 2.3. An arrow of length s with distance a' to the surface is located inside a medium with $n = -1$. The rays emitted by the arrow (blue) are negatively refracted at the interface. For an observer or a camera located at a distance a above the surface, the object straight beneath it appears magnified, since the actual viewing angle α' is larger than α, which is the expected viewing angle without the negatively refracting material, i.e., if the rays would solely propagate in air. From simple geometric considerations we can obtain the apparent size of the object, s'. Hence, the magnification factor is given by:

$$\frac{s'}{s} = \frac{a + a'}{a - a'}. \tag{2.24}$$

It is obvious that the magnification factor depends on both the position of the observer and the position of the object. Taking a to be fixed, the magnification factor increases with increasing a', starting from $a' = 0$, and diverges at $a' = a$. At this specific point (which we refer to as critical point in the following), the optical path length is exactly zero and thus, the arrow seems to be "directly in the face of the observer", causing the divergence of the magnification factor.

For the case $a' > a$ the arrow seems to have changed its orientation as if it was mirrored at the vertical axis. The optical path length is negative. Increasing the distance a' further has the effect of shrinking the apparent size of the object.

(a) (b) (c)

Figure 2.4: (a) Empty drinking glass with a metal rod. (b) Same scene as in (a), but the glass is filled with a liquid with $n = 1.3$. (c) The liquid has a refractive index of $n = -1.3$.

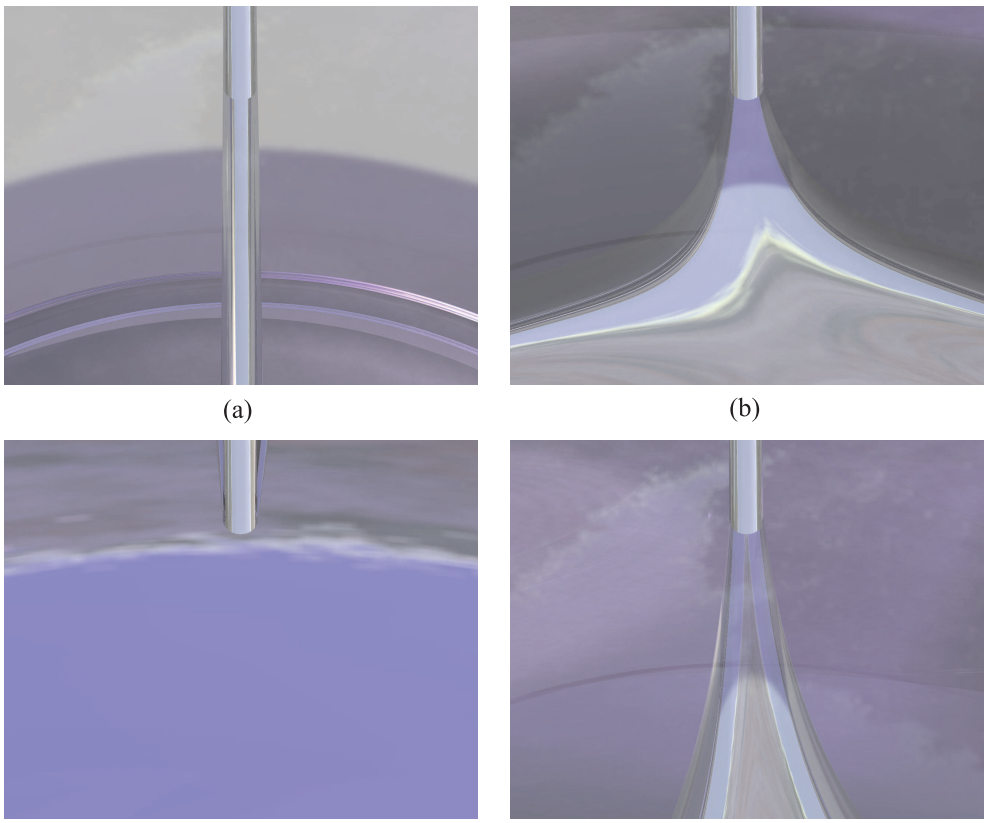

(a) (b)

(c) (d)

Figure 2.5: Same scene as shown in Fig. 2.4. A close-up view of the metal rod submerging into the liquid. (a) $n = 1, 2$, (b) $n = -1.2$, (c) $n = -1$ and (d) $n = -1.4$.

The modulus $|n < 0|$ of the medium determines the strength of the refraction: the larger the modulus, the stronger the rays are refracted towards the surface normal, leading to a reduced viewing angle. Thus, in the limit $|n < 0| \gg 1$ the magnification factor can be written in the simple form: $s'/s = (a + a')/a$.

In order to illustrate how a negative refractive index would effect our daily life, we have created some photorealistic images using the ray-tracing program POV-Ray 3.6 [19]. Figure 2.4 shows a metal rod in a drinking glass filled with different liquids. In the case of a liquid with the negative refractive index $n = -1.3$, the metal rod is refracted to the "wrong" side, as one would guess intuitively. However, one can additionally observe some smaller effects. For instance, the bottom side of the (top-located) air/liquid interface together with a part of the rod is visible, i.e. "the observer is able to look around corners". This is caused by negative refraction of the rays at the (lateral) glass/liquid interface. On the other hand, it is no longer possible to observe the bottom of the glass itself, which is yet clearly visible in the case $n = +1.2$.

If we move the camera nearer to the air/liquid interface, we obtain the images shown in Fig. 2.5. For case (a) and (b) we have simply switched the sign of n from $n = 1.2$ to $n = -1.2$. While in (a) the rod keeps its original cylindrical shape, it appears trumpet-shaped in (b). The reason for this apparent re-shaping is the depth dependence of the magnification factor. The deeper a part of the rod is inside the liquid (approaching the critical point) the more it is magnified for the observer. Thus, in (b) one can directly track the dependence of the magnification factor on depths. In (d) the re-shaping is less pronounced. This is a result of the higher modulus of the refractive index of $n = -1.4$, shifting the critical point to larger depths. In (c) the rod is refracted to the back-side. Additionally, at first sight the surface seems to cause strong reflection. However, this is not the case, since we have set $n = -1$ and $Z = Z_0$, i.e., the reflection is zero. Instead, one can observe the sky behind the camera due to the negative refraction.

Perfect lens

In the year of 2000, Sir John Pendry examined the properties of a coplanar plate with $n = -1$ [4], as illustrated in Fig. 2.6. This slab does not represent a lens of the habitual language use, since it neither produces any magnification nor does it focus or disperse parallel incident rays. Furthermore, one cannot specify an optical axis. However, considering a point source in distance a in front of this slab, all the rays emitted by the source meet in one single point behind the slab at the distance a'. Thus, in the context of ray optics the point source is perfectly imaged to the back side of this slab. Instead of the well-known lens equation $1/f = 1/a + 1/a'$ for a normal lens, in the case of a coplanar plate with $n = -1$ one obtains $d = a + a'$.

For determining the imaging properties, we have to switch to wave optics. Waves emitted from an object and propagating mainly into the z-direction, are given by:

$$\boldsymbol{E}(\boldsymbol{r}, t) = \sum_{k_x, k_y} \boldsymbol{E}_0(k_x, k_y) \mathrm{e}^{\mathrm{i}(k_x x + k_y y + k_z z - \omega t)} \tag{2.25}$$

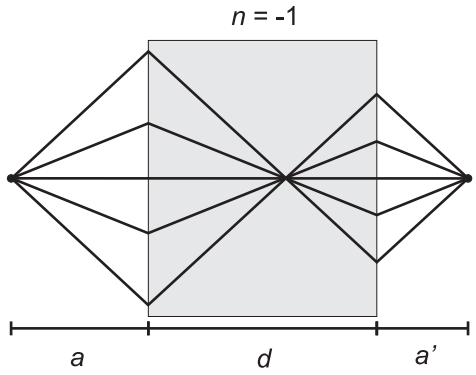

Figure 2.6: A block of thickness d and refractive index $n = -1$ is depicted in grey. A point source is located in front of this block at the distance a. It is perfectly imaged to behind the block at the distance a'.

with $k_z = \sqrt{\omega^2/c_0^2 - k_x^2 - k_y^2}$. Thus, only for $\omega^2/c_0^2 \geq k_x^2 + k_y^2$ the waves are propagating. If this condition is not satisfied, k_z becomes complex and thus produces an exponential decay in the electric field. These exponentially decreasing waves are called evanescent waves. However, as especially large values of k_x and k_y contribute to the fine details of an image, not detecting these components leads to a degeneration of the image. For this reason, in conventional optics the resolution is generally limited and approximately given by $\Delta x \approx \lambda/2$, with Δx representing the smallest possible resolution.

Pendry showed, for negative refracting materials with $\varepsilon = \mu = n = -1$, that evanescent modes increase exponentially inside the slab, so compensating for the exponential decay outside the slab. Thus, in a distance a' behind the slab, a perfect reconstruction of the original image is possible, since no information gets lost during imaging. However, this reconstruction occurs not instantaneously, otherwise the conservation of energy would be violated. This phenomenon can be described physically by the coupling of surface modes at the frontside with surface modes at the rear side of the slab. Alternatively, we can consider the optical path length between the object and the image. Since it is exactly zero for the slab with $n = -1$, effectively no distance is covered, and all information is kept.

However, it is shown in [20, 21] that even the slightest deviations δ_1, δ_2 from $n = -1 \pm \delta_1 + i\delta_2$ in the range of per mill already degrade the perfect image dramatically, reducing the image quality to a value only slightly better than obtained by conventional lenses.

Furthermore, Pendry proved in his first publication on the perfect lens that within the electrostatic limit even a very thin layer of material with a negative permittivity should be sufficient for sub-wavelength imaging. Indeed, in 2004 a group in Berkeley [5] verified this prediction experimentally by creating an image with a resolution better than the diffraction limit using a thin silver film. A fine-structured object was imaged by a $35\,\text{nm}$ silver film into a photoresist using light of $365\,\text{nm}$ wavelength. In the developed photoresist, details of $60\,\text{nm}$, corresponding to about $\lambda/6$, were resolved. The disadvantage of this kind of lens, however, is the restriction to the near-field. This restriction was finally overcome by the same group in 2006, providing a method to transfer the near-field into the far-field [22].

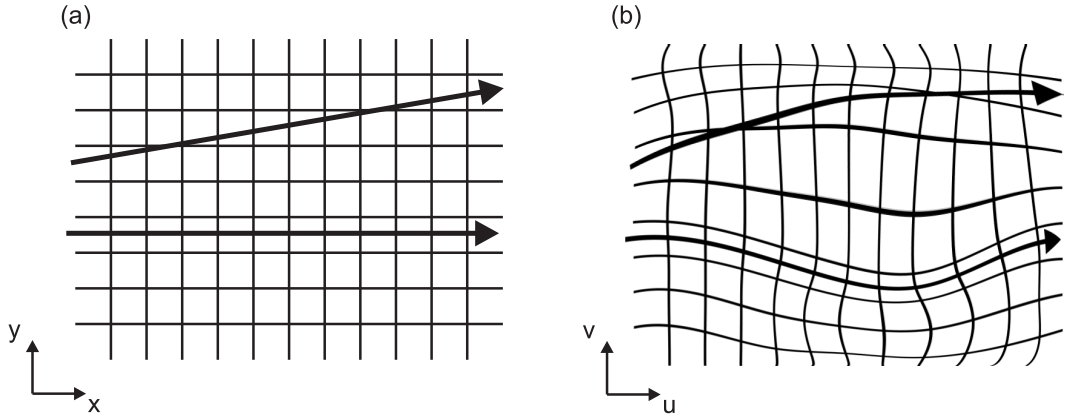

Figure 2.7: (a) Orthogonal coordinate system with two arrows indicating the propagation direction of light rays. (b) Transforming the coordinate system requires a corresponding transformation of the rays.

Cloaking

Besides the perfect lens, another possible application for metamaterials was developed independently by Pendry [6] and Leonhardt [7] at the same time: cloaking, i.e., hiding objects to a viewer. Figure 2.7 depicts exemplarily what their suggestion is based upon. One assumes an elastic Cartesian coordinate system [see (a)], in which light rays are propagate, and than distort this coordinate system. This can be described by a coordinate transformation:

$$x, y, z \rightarrow u(x, y, z), v(x, y, z), w(x, y, z). \tag{2.26}$$

Here, (u, v, w) are the coordinates of the new mesh with respect to the $x, y,$ and z axes. It is important to note that Maxwell's equations keep their form during transformation from one coordinate system to the other. Yet, the permittivity ε and the permeability μ have to be scaled appropriately. In the example shown in Fig. 2.7 in (a), both the permittivity and permeability are scalar quantities not depending on the spatial position, while the transformation in (b) leads to a strong spatial dependency of both the permittivity and permeability. However, this transformation is not only valid for light rays, but all kinds of fields, e.g., the Poynting vector $\boldsymbol{S}$. Thus, rays can be controlled at will, having chosen the appropriate values for the permittivity and the permeability.

The idea to utilize transformations has far-reaching consequences. Choosing an appropriate transformation, a specific region in space can be excluded from all electromagnetic fields, as Pendry has shown. This means that an object located in this specific area cannot be detected. Only five months later, Smith *et al.* [8] demonstrated how to exploit this idea experimentally. They achieved to almost completely cloak a copper cylinder. This experiment was performed for frequencies in the microwave regime, which simplifies the fabrication of materials with the appropriate properties.

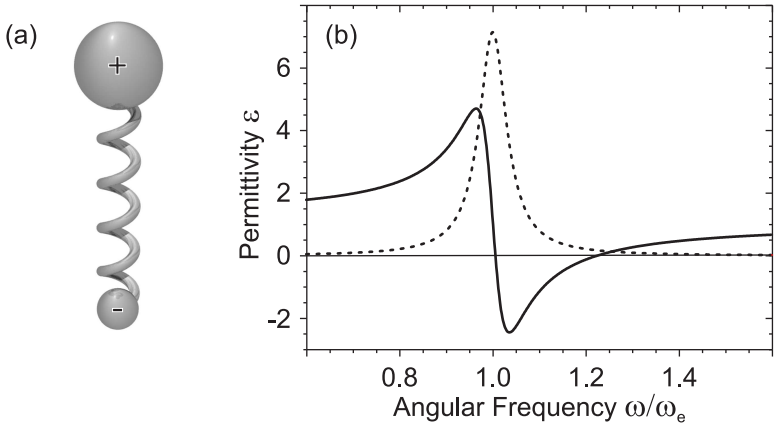

Figure 2.8: (a) Scheme of a Lorentz oscillator: The electron is connected to the positively charged atom core *via* an elastic spring. In (b) the electric permittivity of an ensemble of such oscillators is depicted. The parameters are $\omega_{\mathrm{pl}} = 0.29\omega_{\mathrm{e}}$ and $\gamma = 0.07\omega_{\mathrm{e}}$. The imaginary part is indicated by a dashed curve, the real part by a solid curve.

2.2 Natural materials

In the last section we have discovered many interesting optical effects caused by $\mu \neq 1$. However, there is an obvious reason why these effects have only been studied the last years: There are no natural materials which show a negative permeability or even a negative refractive index at optical frequencies. The following subsections deal with both the permittivity and permeability and their values found in natural materials.

2.2.1 Lorentz oscillator

In 1896, Hendrik Antoon Lorentz suggested a very simple classical model to describe the interaction of light and atoms. In his model the electron of the atom is elastically connected to the positive charged atom core, which is schematically illustrated *via* a spring in Fig. 2.8(a). The electric field of the incoming light displaces the electron with respect to the atom core, resulting in an electric dipole moment. If the incoming wave is monochromatic, the electron is driven by the Coulomb force $\boldsymbol{F} = e\boldsymbol{E} = e\boldsymbol{E}_0 \exp(-\mathrm{i}\omega t)$ with the elementary charge $e \approx -1.6 \cdot 10^{-19}\,\mathrm{C}$. This force excites the electron to oscillate at the same frequency, with an amplitude x with respect to the atom core. Since the mass of the atom core is much larger than the mass of the electron, the movement of the atom core can be neglected. Thus, for the electron we obtain the classical equation of motion in one dimension:

$$\ddot{x} + \gamma\dot{x} + {\omega_{\mathrm{e}}}^2 x = \frac{e}{m} E. \tag{2.27}$$

Here, γ is the factor of attenuation, m the electron mass and ω_{e} the resonance frequency of the mass-spring system. The well-known solution of the inhomogeneous equation is

$$x(\omega) = \frac{e}{m} \frac{1}{{\omega_{\mathrm{e}}}^2 - \omega^2 - \mathrm{i}\gamma\omega} E. \tag{2.28}$$

After multiplication with the electron charge, we obtain the dipole moment $d = ex$. To describe the properties of a medium, one considers the polarization density P, which in this case is given by $P = n_0 d$ with the oscillator density n_0. Here, we have already used the assumption that the dipoles do not interact with each other. Thus, spatial dispersion is omitted. As the polarization is linearly proportional to the electric field, we can apply the equations presented in the beginning of this chapter. In this manner we can derive the electric permittivity:

$$\varepsilon(\omega) = 1 + \frac{\omega_{\mathrm{pl}}^2}{{\omega_{\mathrm{e}}}^2 - \omega^2 - \mathrm{i}\gamma\omega} \tag{2.29}$$

with the plasma frequency $\omega_{\mathrm{pl}}^2 = (n_0 e^2)/(m\varepsilon_0)$. A typical spectral behavior is depicted in Fig. 2.8(b).

2.2.2 Drude model

In metals, the electrons of the valence band are quasi-free and do not feel any restoring force. Thus, the term ${\omega_{\mathrm{e}}}^2 x$ in equation (2.27) is zero, which corresponds to a resonance frequency of $\omega_{\mathrm{e}} = 0$. Then, the inhomogeneous solution of this accordingly modified equation is:

$$x(\omega) = -\frac{e}{m}\frac{1}{\omega^2 + \mathrm{i}\gamma\omega}E. \tag{2.30}$$

Thus, in analogy to the Lorentz oscillator model we derive the permittivity:

$$\varepsilon(\omega) = 1 - \frac{\omega_{\mathrm{pl}}^{*2}}{\omega^2 + \mathrm{i}\gamma\omega} \tag{2.31}$$

with the modified plasma frequency $\omega_{\mathrm{pl}}^{*2} = (n_0 e^2)/(m_{\mathrm{eff}}\varepsilon_0)$. Here, m_{eff} is the effective electron mass, given by the curvature of the valence band dispersion relation.

Below the plasma frequency, propagating electromagnetic waves do not exist(for $\mu = 1$), as the permittivity is negative and thus plane waves are attenuated exponentially along the propagation direction:

$$\boldsymbol{E}(x,t) = \boldsymbol{E}_0 \exp\left[\mathrm{i}\omega\left(\frac{n_{\mathrm{R}}}{c_0}x - t\right)\right]\exp\left(-\frac{x}{\delta}\right). \tag{2.32}$$

Here, n_{R} represents the real part of the refractive index $n = \sqrt{\varepsilon}$. The skin depth δ is given by

$$\delta = \frac{\lambda}{2\pi n_{\mathrm{I}}} \tag{2.33}$$

and describes the penetration depth of the electromagnetic wave into the metal. In this equation, $\lambda = 2\pi c_0/\omega$ is the vacuum wavelength and n_{I} the imaginary part of the refractive index. In noble metals, the penetration depth for optical frequencies is only a few tens of nanometers. Consequently, the electrons are displaced solely near the surface of the metal at these high frequencies.

In Fig. 2.9, experimental data [23] of the permittivity for silver (crosses) and gold (circles) are depicted. The red and black lines, respectively, are fits to the experimental data

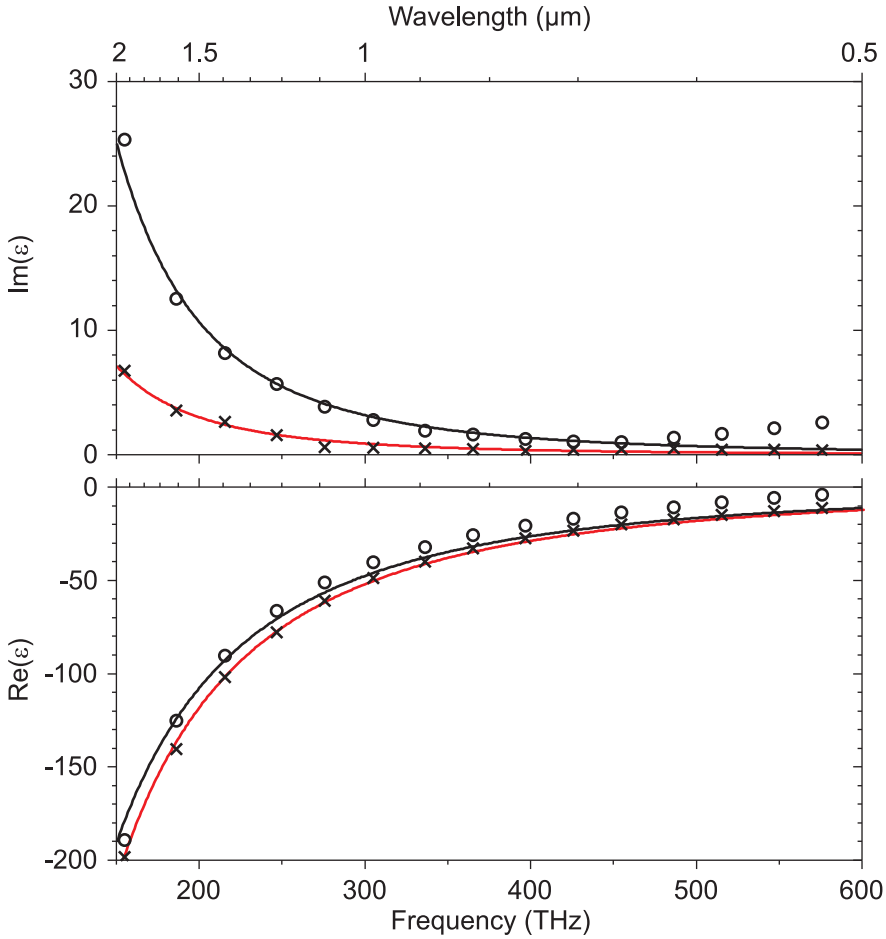

Figure 2.9: Experimental data of the permittivity of silver (crosses) and gold (circles) [23]. The black curve depicts a fit to the data of gold using the function (2.31). Accordingly, the red curve represents the fit to the data of silver. For gold the deviations from the fit of a Drude behavior are larger than for silver due to interband transitions for frequencies above $575\,\mathrm{THz}$.

using the function (2.31). For silver we obtain: $\omega_{\mathrm{pl}} = 2\pi \cdot 2184\,\mathrm{THz}$ and $\gamma = 2\pi \cdot 5.06\,\mathrm{THz}$. Analogously, we get for gold: $\omega_{\mathrm{pl}} = 2\pi \cdot 2095\,\mathrm{THz}$ and $\gamma = 2\pi \cdot 19.63\,\mathrm{THz}$. While the agreement between the experimental data and the fit is very good in the case of silver, we observe clear deviations from the assumed Drude characteristic for high frequencies in the case of gold. Here, photons with energies above $2.38\,\mathrm{eV}$ ($575\,\mathrm{THz}$) can excite electrons from the fully occupied valence band into the conduction band, which the Drude model does not account for.

Natural materials such as silver and gold are apparently ideal for achieving a negative permittivity. Yet, we are interested in a frequency region of about $300\,\mathrm{THz}$ ($1\,\mu\mathrm{m}$ wavelength). Indeed, the real part of ε is negative, but the attenuation is also very large, which is obviously undesired. One possible remedy was found by Sir John Pendry in 1996 [24]. He proposed to use infinitely long wires instead of a homogenous metal. If the lattice constant of this structure is much smaller than the considered wavelength of interest, the material acts as an effective metal. In this manner, the dipole density is reduced enormously, and fur-

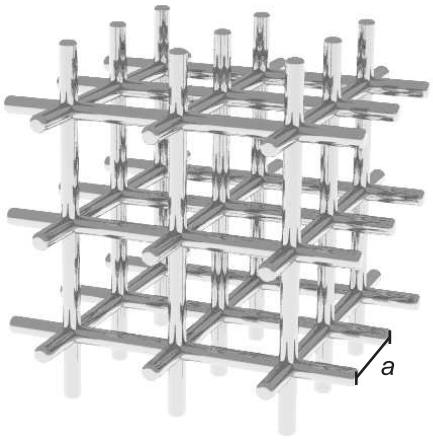

Figure 2.10: Metal wires with a radius much smaller than the lattice constant a are schematically depicted. If a is much smaller than the wavelength of the incident light, the structure acts as an effective diluted metal.

thermore the effective electron mass is modified. Hence, it is possible to tailor the effective plasma frequency to one's needs. As an example, an effective, diluted metal is illustrated in Fig. 2.10.

Such diluted metals are also applied in common microwaves ovens: A perforated metal film is located behind the front window. These holes are arranged periodically with a lattice constant smaller than the used electromagnetic radiation of the microwave. Hence, the microwave radiation "feels" a diluted homogenous metal, which it cannot penetrate. This provides the opportunity to look through holes into the microwave oven, while the microwave radiation cannot leave it.

2.2.3 Metallic nanoparticles

As we have seen in the previous section, the optical properties of metals can be described by the Drude model. Furthermore, this model holds for both diluted effective and homogeneous metals.

In contrast, in macroscopic dimensions, a metal rod of length l irradiated with an electromagnetic wave of wavelength λ, exhibits a resonance at $\lambda = 2\,N\,l$ with $N = 1, 2, 3, \ldots$, if the electric field is polarized along the metal rod. This effect is known as antenna resonance. Varying the thickness of the metal bar has virtually no effect on the resonance wavelength.

However, if we scale down the size of the antenna to several tens or hundreds of nanometers, the behavior of the antenna changes qualitatively. On this scale the electromagnetic wave penetrates a big portion of the total volume, since the geometric dimensions are comparable to the skin depth of the metal. In this case, one obtains a collective excitation of the electrons. Hence, the electrons are displaced with respect to the ion cores, which produces a restoring force.

First, we describe the optical scattering by spherical metallic particles. This analytical theory is based on the work of Gustav Mie [25]. Using a quasi-statical approximation and considering the environment of the particles one obtains the polarizability [26]:

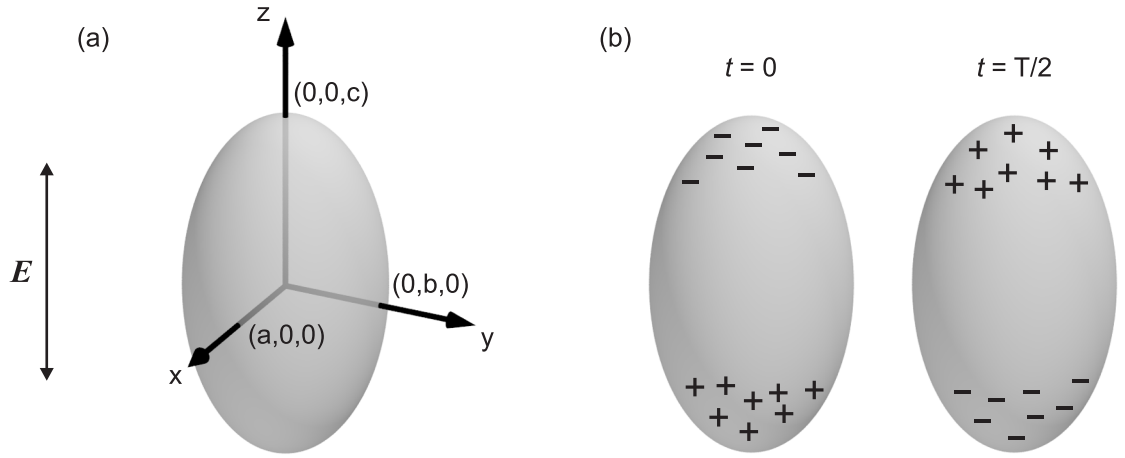

Figure 2.11: (a) Ellipsoidal shaped metal particle with an electric alternating field applied in z direction. (b) Two snap shots of a particle plasmon at different times during one oscillation period T.

$$\alpha(\omega) = 3\varepsilon_0 \frac{\varepsilon(\omega) - \varepsilon_\mathrm{s}}{\varepsilon(\omega) + 2\varepsilon_\mathrm{s}} V. \tag{2.34}$$

V represents the volume of the sphere, ε_s the permittivity of the environment and $\varepsilon(\omega)$ the permittivity of the metal. From the polarizability we derive the dipole moment:

$$\boldsymbol{d}(\omega) = \varepsilon_\mathrm{s} \alpha(\omega) \boldsymbol{E}_0. \tag{2.35}$$

The dipole moment and thus the response of the particle is at maximum if the denominator of equation (2.34) vanishes:

$$|\varepsilon(\omega) + 2\varepsilon_\mathrm{s}| = 0. \tag{2.36}$$

Only for metals with a negative permittivity can the denominator become almost zero, since for normal dielectrics $\varepsilon_\mathrm{s} > 0$ holds. The corresponding resonances are called Mie resonances, or particle plasmons.

In the case of ellipsoidally shaped particles (as depicted in Fig. 2.11), the polarizability is a tensor. Choosing the half-axes a, b, c of the ellipsoid to direct along the coordinate axes, we obtain the dipole moment [26]:

$$\boldsymbol{d} = \varepsilon_\mathrm{s} \begin{pmatrix} \alpha_x & 0 & 0 \\ 0 & \alpha_y & 0 \\ 0 & 0 & \alpha_z \end{pmatrix} \boldsymbol{E} \tag{2.37}$$

with the polarizabilities

$$\alpha_i = \varepsilon_0 \frac{\varepsilon(\omega) - \varepsilon_\mathrm{s}}{\varepsilon_\mathrm{s} + (\varepsilon(\omega) - \varepsilon_\mathrm{s}) L_i} V. \tag{2.38}$$

In this case, V represents the volume of the ellipsoid and $L_i(a, b, c) > 0$ (with $i = x, y, z$) is a geometric factor with the side condition $\sum_i L_i = 1$. Furthermore, $L_i(a, b, c)$ is a monotonic

in each variable. In the case of a sphere, we can reproduce equation (2.34) with the geometric factor $L_i = 1/3$. If the electric field is polarized along one of the principle axes, the dipole moment becomes maximal under the condition:

$$|\varepsilon_\mathrm{s} + (\varepsilon(\omega) - \varepsilon_\mathrm{s})L_i| = \min. \tag{2.39}$$

For small imaginary parts of the permittivity $\varepsilon_\mathrm{I}(\omega)$ we obtain approximately the condition:

$$\varepsilon_\mathrm{R} = \varepsilon_\mathrm{s}\left(1 - \frac{1}{L_i}\right). \tag{2.40}$$

Since $L_i \leq 1$, one requires again a negative permittivity, which occurs in metals for frequencies below the plasma frequency.

From this formula we can draw two important consequences: Increasing the permittivity of the environment shifts the resonance to the red (smaller frequencies). However, this shift is partially compensated by the smaller real part of the permittivity in metals for smaller frequencies according to the Drude model. If we change the geometry, two cases must be distinguished. Enlarging the axis directing along the electric field causes a red-shift of the resonance, while enlarging the axes perpendicular to the electric field shifts the resonance to the blue or to higher frequencies.

2.2.4 Magnetism

In the last sections we have dealt with different possibilities for obtaining a negative permittivity. Phenomenologically one can describe magnetic responses already using Bohr's atom model. Electrons with a spin circle the atom core and thus generate a magnetic moment. The individual moments of many electrons sum up to the total magnetic moment of the atom. In the case of ferromagnetica the static magnetic moments of individual atoms point into the same direction leading to a magnetic response of $\mu(\omega = 0) \gg 1$. However, studying the effects of alternating fields on the magnetic response we find most of the magnetic response vanishing for frequencies of several MHz or GHz. Thus, the permeability of these natural materials becomes unity above these (high) frequencies .

2.3 Metamaterials

While metals allow for a negative permittivity at optical frequencies, nature does not provide us with materials which exhibit a negative permeability at optical frequencies. In 1999 when Pendry proposed the fabrication of artificial structures [2] for obtaining a negative permeability, researches started to deal with metamaterials. Electromagnetic metamaterials are artificial, composite materials usually consisting of periodically arranged, identical, responsive building blocks.

If the artificial functional elements are each much smaller than the relevant wavelength, the electromagnetic wave cannot resolve the building blocks, but averages over them. Hence,

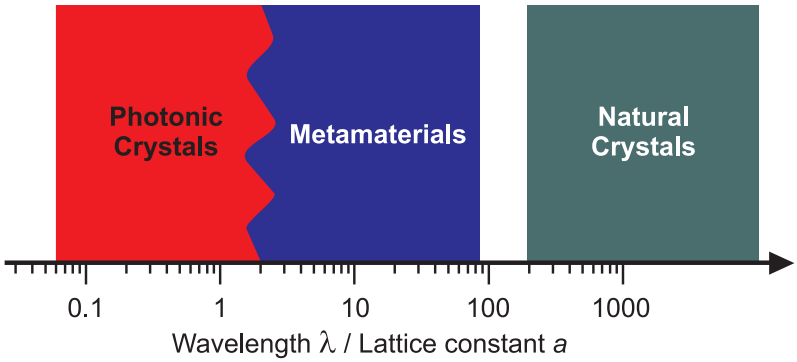

Figure 2.12: The ratio wavelength over lattice constant allows for a classification of different optical materials

the wave sees an effectively homogenous material and one can introduce an (effective) permittivity and an (effective) permeability.

In Fig. 2.12 the relation of wavelength λ to lattice constant a is exemplarily illustrated. For natural crystals the lattice constant is on the order of several Ångströms while wavelength of the visible light is several hundreds of nanometers. Thus, the typical ratio of λ/a is about 1000. This ratio illustrates that light cannot resolve the individual atoms. In metamaterials this ratio is usually lower. However, it is still sufficient for introducing an effective permittivity and an effective permeability. If the ratio is reduced to two or less, Bragg scattering or Wood anomalies (see below) can occur and the concept of metamaterials becomes questionable. However, in photonic crystals diffraction is exploited to influence the light propagation as required to one's request [27]. In this case, the exact spatial dependence of the permittivity is crucial. In section 3.2 we give a brief introduction to photonic crystals.

In the field of metamaterials we can find mainly two approaches for obtaining a negative refractive index, which we outline in the following sections. Both approaches are based on functional elements arranged in a periodic lattice with a lattice constant smaller than the relevant wavelength.

2.3.1 Transmission lines

In 1951 Georgy Danilovich Malyuzhinets [28] presented a one-dimensional model system supporting electromagnetic waves with a negative phase velocity. A scheme of this structure is depicted in Fig. 2.13. It consists of a periodic arrangement of "artificial atoms". Each is formed by two inductors L and two capacitors C. In the upper left part, L and C are connected in series, while in the right part they are connected in parallel forming a LC resonant circuit with the LC-resonance frequency $\omega_{LC} = 1/\sqrt{LC}$. Using Kirchhoff's current law

$$I_{m-1} = I_m + \frac{U_m}{Z_2} \tag{2.41}$$

and applying Kirchhoff's voltage law

$$U_{m-1} = I_{m-1} Z_1 + U_m \tag{2.42}$$

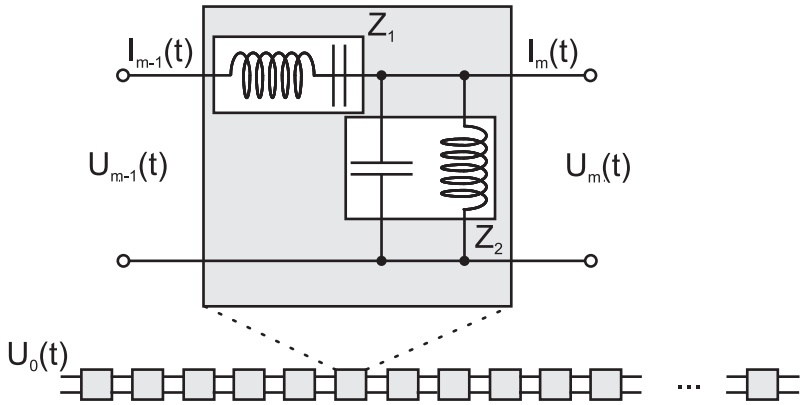

Figure 2.13: A simple one-dimensional model with waves of negative phase velocity is illustrated. The periodically arranged "artificial atoms" consist of the inductor L and the capacitor C connected in series forming the complex impedance Z_1. This impedance is connected in parallel to a further inductor and capacitor forming the complex impedance Z_2.

we obtain

$$\frac{U_{m-1} - 2U_m + U_m}{Z_1} = \frac{U_m}{Z_2}. \tag{2.43}$$

This equation can be solved with the ansatz of a plane wave: $U_m = U_0 \exp[-\mathrm{i}km]$. Applying the values of the complex impedances we derive the term:

$$2\left(\cos(k) - 1\right) = -\frac{\left(\omega^2 - \omega_{LC}^2\right)^2}{\omega^2 \omega_{LC}^2}. \tag{2.44}$$

In the metamaterial limes we have $k \ll 1$, which allows us to expand the cosine. With the requirement of the energy flow propagating from left to right, we get $U_0 I_0 > 0$, which determines the algebraic sign of k. Thus, we obtain in the limit for small k:

$$k = \frac{\omega}{\omega_{LC}} - \frac{\omega_{LC}}{\omega}. \tag{2.45}$$

While we have fixed the direction of the energy flow, the propagation direction of the phase fronts depends on the frequency. Above the LC-resonance frequency the phase fronts propagate from left to right (here $k > 0$), while below the resonance frequency they propagate from right to left ($k < 0$), i.e., opposite to the energy flow. The latter situation corresponds to a negative refractive index $n < 0$.

Therefore, transmission lines can show a negative refractive index for a large frequency range. So far, however, such transmission lines have been fabricated for the microwave regime only, since for optical frequencies appropriate designs cannot be adopted easily. One remedy was shown by Engheta *et al.* [29], yet the fabrication is difficult. Many further explanations to transmission lines and their current applications can be found in reference [30].

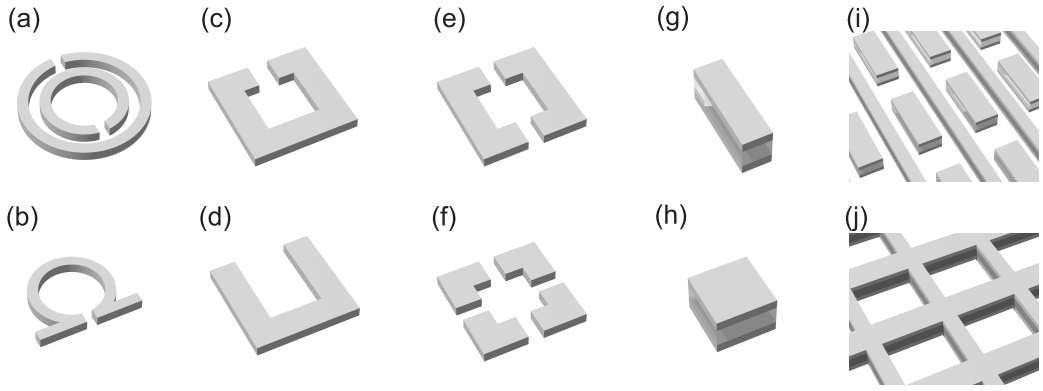

Figure 2.14: Several realizations of "magnetic atoms" [(a)-(h)] as well as two structures [(i)-(j)] with a negative refractive index are depicted. (a) Double split-ring resonator, (b) Ω-structure, (c) SRR with one cut, (d) U-like SRR, SRR with two (e), and four (f) cuts, (g) cut-wire pairs, (h) double square plates, (i) cut-wire pairs combined with long wires, and (j) "double-fishnet"-structure.

2.3.2 Resonant structures

In the case of transmission lines, a negative phase velocity is obtained in the context of alternating currents and voltages. In the following, we present functional "atoms" with a tailored electric or magnetic response. Examples of these are shown in Fig. 2.14. The most famous example is the split-ring resonator (SRR), which was realized in many different variations [see (a)-(f)]. The authorship of the idea for these elements is attributed to Pendry's work from 1999 [2], because he deduced the permeability for different SRRs explicitly for the first time. Yet, in 1982 Walter Hardy and Lorne Whitehead already studied SRRs in the frequency range of $200\,\mathrm{MHz}$ to $2\,\mathrm{GHz}$ with respect to their magnetic response [31]. Furthermore, in 1977 these structures were already discussed by Hans Schneider and Peter Dullenkopf under the name slotted-tube resonator [32]. In fact, even in a textbook of the year 1952 [33] one can find an illustration of a SRR and the corresponding formula of its magnetic response. However, Pendry was the first one who suggested to arrange the SRRs in a periodic lattice with a lattice constant smaller than the relevant wavelength. As a result, the magnetic permeability can be introduced and the idea of metamaterial was born.

The physics of the various SRRs is based on the simple LC resonant circuit. Figure 2.14(c) depicts a simplified version of a SRR. Here, the resonant circuit consists merely of one winding of a coil with inductance L, while the ends of the coil form the capacitance C. Pendry showed that combining many of such elements can provide a magnetic response and offers the possibility of realizing a negative permeability.

Apart from the SRRs, further alternative structures were proposed. Eliminating the arms in Fig. 2.14(e) and rotating the resulting wires leads to the cut-wire pairs structure [34–36] shown in (g). The advantage of these structures is the simplified fabrication compared to the SRRs, especially if they are intended for operation at high frequencies. Consequently, the cut-wire pairs are currently often employed for optical frequencies.

In 2001 for the first time, negative refraction was demonstrated in an experiment [3] by utilizing a composite structure made of magnetic and electric atoms. The magnetic atoms

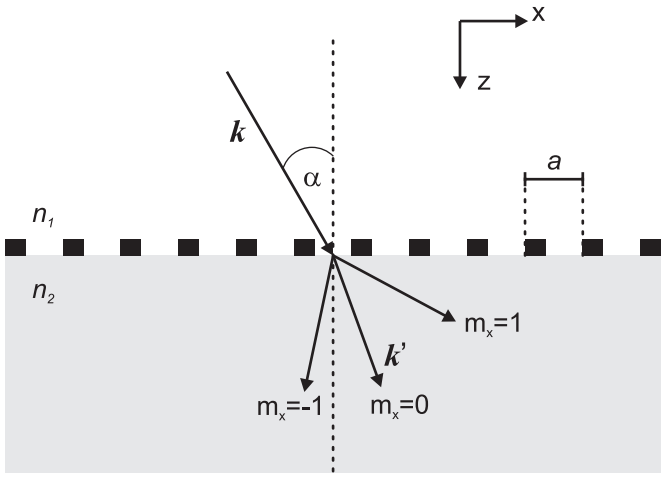

Figure 2.15: A lattice with lattice constants $a_x = a_y = a$ on top of a medium with refractive index n_2 is schematically sketched. For clarity only the periodicity in x-direction is shown. A wave with wave vector $\boldsymbol{k}$ propagating in a medium with refractive index n_1 impinges the lattice under an oblique angle of incidence α. In the medium with refractive index n_2 the orders of diffraction $m_x = \pm 1$ are schematically depicted. $m_x = 0$ corresponds to the undiffracted wave. Reflections and higher orders of diffraction are neglected for simplicity.

were realized by SRRs. Thin long metal wires served as electric atoms. As described previously, these metal wires can be considered as a diluted metal. The combination of these two elements lead to a spectral region in which a negative refractive index was obtained.

In 2005 a combination of cut-wires and long metal wires [see (j)] [37, 38] was presented by Zhang *et al.* . This structure, which remains quite feasible in fabrication even for optical frequencies, showed a negative refractive index for optical frequencies for the first time. In the course of this thesis we discuss this proposed structure yet in more detail later on. Another combination of cut-wires and metal wires touching each other is illustrated in (j) [39].

For further details concerning the progress of metamaterials using resonant structures we refer to the already large number available of current review articles [11, 40–45].

2.3.3 Wood anomalies

Metamaterials are based on a periodic arrangement of the fundamental building blocks. If the lattice constant a becomes comparable to the wavelength of light, diffraction can occur. This leads to resonances which cannot be described in terms of an effective permittivity or effective permeability. These resonances become important for some metamaterials in this thesis. In the following, we describe the physics.

In 1902 Wood [46] discovered dark and bright spectrally narrow bands in the reflection of a grating. However, these bands could only be observed if the electric field was oriented orthogonal to the grooves of the grating. Since this effect could not be explained by the ordinary grating theory, he called these bands “anomalies”. Theoretically, the first person to describe these anomalies was Rayleigh in 1907 [47]. For this reason, in literature these anomalies are named Wood anomalies as well as Rayleigh anomalies or Rayleigh-Wood

anomalies.

We consider a simple description of these anomalies which gives their correct spectral positions. The scheme of the geometry is shown in Fig. 2.15. We restrict ourselves to a two-dimensional square lattice with lattice constants $a_x = a_y = a$, since the metamaterials we fabricated and studied are also arranged in a square lattice. The lattice gives rise to diffraction. The wave vector $\boldsymbol{k}$ with $k = |\boldsymbol{k}|$ and the lattice vector $\boldsymbol{g}$ are given by

$$\boldsymbol{k} = \begin{pmatrix} k_x \\ k_y \\ k_z \end{pmatrix} \quad \text{and} \quad \boldsymbol{g} = \frac{2\pi}{a} \begin{pmatrix} m_x \\ m_y \\ 0 \end{pmatrix} \tag{2.46}$$

with $m_i = 0, \pm 1, \pm 2, \ldots$ denoting the different orders of diffraction. For the diffracted wave, the wave vector $\boldsymbol{k}'$ with $k' = |\boldsymbol{k}'|$ in the medium with refractive index n_i is then given by

$$\boldsymbol{k}' = \begin{pmatrix} k_x + g_x \\ k_y + g_y \\ \pm\sqrt{k^2 n_i^2 - (k_x + g_x)^2 - (k_y + g_y)^2} \end{pmatrix}. \tag{2.47}$$

Here, i equals 1 if the diffraction appears in the first medium and i equals 2 if the diffraction appears in the second medium. The positive (negative) square root has to be taken for the second (first) medium. k_z was obtained from equation (2.11): $k' = n_i k$.

The anomaly occurs, if the diffracted beam is oriented parallel to the lattice, i.e., the beam is at the edge between propagation and being evanescent. This corresponds to the condition $k_z = 0$. To simplify the discussion, we restrict ourselves to the case of $k_y = 0$ and distinguish the two cases with $m_x = \pm 1$ and $m_y = 0$, or $m_x = 0$ and $m_y = \pm 1$. In the first case, anomalies occur at wavelengths λ of:

$$\lambda \;=\; (n_i \mp \sin(\alpha))a. \tag{2.48}$$

For the second case, we only obtain one wavelength:

$$\lambda = \sqrt{n_i^2 - \sin^2(\alpha)}\, a. \tag{2.49}$$

At these wavelengths a dip in transmittance is observed. For wavelengths close to the Wood anomalies the structure cannot be described in terms of an effective medium or a metamaterial.

Chapter 3

Some aspects of negative refraction

In the previous chapter we have already mentioned that the refractive index should be rather understood as a "slowness factor". It defines how much faster or slower a wave front of constant phase propagates in a medium than in vacuum. In general, it is not always true that the refractive index also specifies the refraction of a wave at an interface according to Snell's law – in nature many examples can be found that a light beam is refracted to the "wrong side" though non of the materials has a negative refractive index. This behavior results form the fact that the direction of propagation of a wave is defined by the Poynting vector and not the wave vector. In the following we discuss birefringent materials, photonic crystals as well as isotropic and homogeneous thin films, all showing negative refraction under certain conditions.

3.1 Negative refraction in anisotropic materials

First, we discuss birefringent or anisotropic materials. For these natural materials the permittivity $\hat{\varepsilon}$ (and hence the refractive index $\hat{n}$) is a second-rank tensor. An example of a second-rank permittivity tensor and the corresponding refractive index tensor of a non-magnetic, i.e., $\mu = 1$, birefringent material stated in principal coordinates is given by

$$\hat{\varepsilon} = \begin{pmatrix} \varepsilon_1 & 0 & 0 \\ 0 & \varepsilon_2 & 0 \\ 0 & 0 & \varepsilon_3 \end{pmatrix} \text{ and } \hat{n} = \begin{pmatrix} \sqrt{\varepsilon_1} & 0 & 0 \\ 0 & \sqrt{\varepsilon_2} & 0 \\ 0 & 0 & \sqrt{\varepsilon_3} \end{pmatrix}. \tag{3.1}$$

We are interested in the case where the electromagnetic wave is not polarized along a principal axis of the tensor. As a consequence, we obtain in such a medium $\boldsymbol{D} \nparallel \boldsymbol{E}$. For a non-magnetic material, it is $\boldsymbol{B} \parallel \boldsymbol{H}$. However, if we additionally allow for a second-rank permeability tensor, we also obtain $\boldsymbol{B} \nparallel \boldsymbol{H}$. Furthermore, from Maxwell's equations we get $\boldsymbol{k} \cdot \boldsymbol{D} = 0$, i.e., $\boldsymbol{k} \perp \boldsymbol{D}$, and $\boldsymbol{k} \cdot \boldsymbol{B} = 0$, i.e., $\boldsymbol{k} \perp \boldsymbol{B}$. Accordingly, it is $\boldsymbol{E} \nparallel \boldsymbol{k}$ and the Poynting vector $\boldsymbol{S} \nparallel \boldsymbol{k}$. These conditions govern the refraction of a plane wave impinging from an isotropic medium (e.g. vacuum) onto such an anisotropic medium.

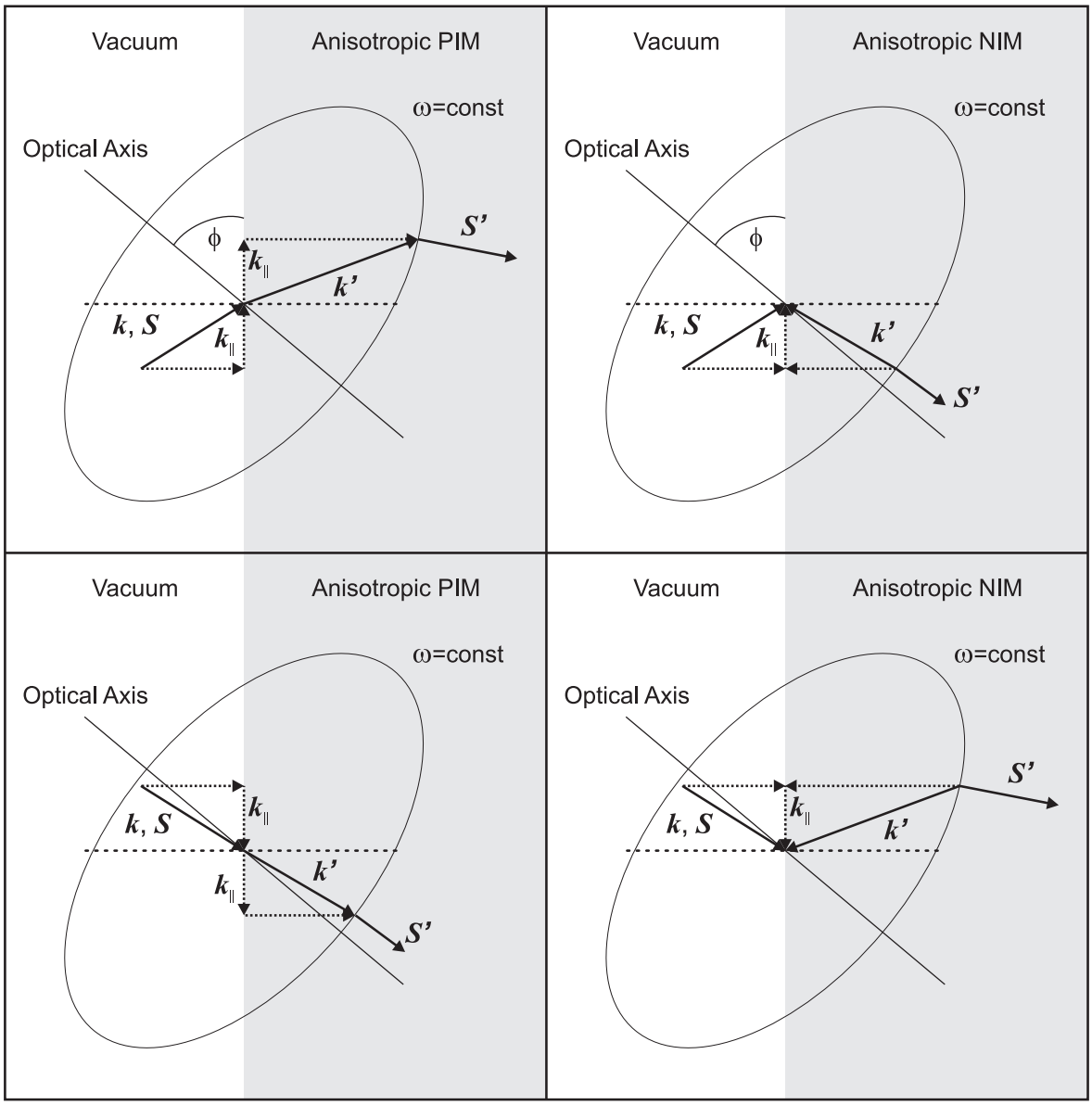

Figure 3.1: A p-polarized plane wave with frequency ω, wave vector $\boldsymbol{k}$, and Poynting vector $\boldsymbol{S}$ impinges on the interface between vacuum and a fictitious birefringent material of either positive (left column, PIM) or negative (right column, NIM) refractive indices. In both cases the optical axis is the same. The frequency ω is identical in both media (energy conservation). Furthermore, the parallel component of the wave vector $\boldsymbol{k}_{||}$ is conserved along the interface. The iso-frequency curve in the respective birefringent material is indicated by a thin line. For the anisotropic PIM both positive and negative refraction of a wave occurs at the interface depending on the angle of incidence. In the case of the anisotropic NIM again both negative and positive refraction occurs depending on the angle of incidence.

The tangential components of $\boldsymbol{E}_{||}$ and $\boldsymbol{H}_{||}$ and the normal components of $\boldsymbol{D}_{\perp}$ and $\boldsymbol{B}_{\perp}$ are conserved at the interface. Furthermore, $\boldsymbol{k}_{||}$ is conserved across the interface. The frequency ω of the incoming wave is identical in both media (energy conservation). In order to derive the normal component of the wave vector $\boldsymbol{k}'_{\perp}$ in the medium, we have to calculate the iso-frequency surface $\omega(\boldsymbol{k})$ =const in the medium. For an isotropic medium, for example, the iso-frequency surface is a sphere, because the refractive index is the same for all directions of $\boldsymbol{k}$. Since we are only interested in a plane which is spanned by the incoming wave vector and the incoming electric field vector, we obtain a circle of constant frequency (so-called iso-frequency curve) in the case of the isotropic medium. Knowing $\boldsymbol{k}_{||}$, one can calculate the corresponding normal component $\boldsymbol{k}_{\perp}$ with the help of the iso-frequency curve. Yet, for anisotropic media the iso-frequency curve is an ellipse. The lengths of corresponding main axes are defined by the different refractive indices. The ellipse is oriented along the principle axis of (3.1). Furthermore, we are interested in the Poynting vector. In the case of linear lossless dielectric materials, the Poynting vector $\boldsymbol{S}'$ and the group velocity v_{gr} point into the same direction [48]. The group velocity is given by

$$\boldsymbol{v}_{\mathrm{gr}} = \nabla_{\boldsymbol{k}}\, \omega(\boldsymbol{k}). \tag{3.2}$$

Hence, we obtain the Poynting vector by the derivation of the dispersion relation, i.e., the Poynting vector is perpendicular to the iso-frequency curve.

With all these conditions, we can construct the refraction of a beam at the interface of an anisotropic medium. Up to now, we only discussed anisotropic materials with only positive refractive indices (PIM). If we also allow for negative values of the permeability, we can obtain an anisotropic material with a second-rank refractive index tensor $\hat{n}$ which only has negative elements (NIM). Figure 3.1 depicts several examples for refraction of a plane wave at the interface of vacuum and such anisotropic materials. On the left hand side, a PIM is shown, while on the right hand side, a NIM is displayed. In both materials the optical axis has the same orientation. As one would expect for a medium of anisotropic positive (negative) refractive indices, the normal component of the wave vector $\boldsymbol{k}'_{\perp}$ is positive (negative) in the medium with respect to $\boldsymbol{k}_{\perp}$ in vacuum. However, the behavior of the Poynting vector is more complicated. Depending on the angle of incidence the parallel component of the Poynting vector $\boldsymbol{S}'_{||}$ changes sign with respect to $\boldsymbol{S}_{||}$, e.g., for $\boldsymbol{S}'_{||} \cdot \boldsymbol{S}_{||} < 0$ negative refraction occurs. As we can see in Fig. 3.1, this holds for both the anisotropic PIM and the anisotropic NIM. Detailed analytical studies of to the above qualitative discussion can be found in [49]. Corresponding experiments are described in detail in [50]. Further discussions and experiments are presented in [51–53].

Even though the refractive index is positive, negative refraction occurs in natural substances. This phenomenon results from the fact that the direction of propagation of a wave is not given by the wave vector but by the Poynting vector. The refractive index has merely an influence on the wave vector which generally does not point into the same direction as the Poynting vector. As a consequence, anisotropic materials with negative refractive indices can refract rays also to the “normal” side [49] as shown in Fig. 3.1. In conclusion, by solely looking at the refraction of a beam it is only possible to make statements about the direction of the Poynting vector but not about the wave vector or the refractive index.

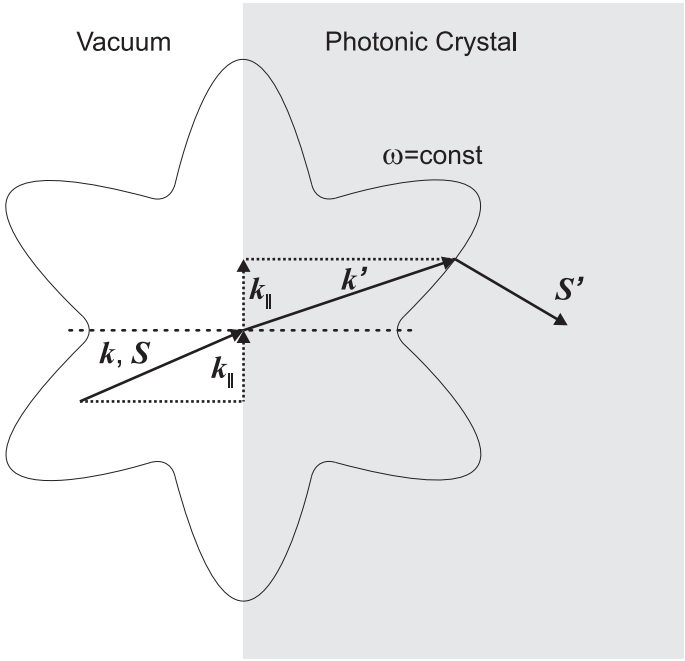

Figure 3.2: A plane wave with frequency ω, wave vector $\boldsymbol{k}$, and Poynting vector $\boldsymbol{S}$ impinges on the interface of vacuum and a photonic crystal. The frequency ω is in both media the same (energy conservation). Furthermore, the parallel component of the wave vector $\boldsymbol{k}_{||}$ is conserved along the interface. A fictitious iso-frequency curve for a photonic crystal of six-fold symmetry is indicated by the thin solid curve. As a result, Poynting vector $\boldsymbol{S}'$ and wave vector $\boldsymbol{k}'$ point into different directions. Furthermore, the parallel component of the Poynting vector changes sign which leads to negative refraction.

3.2 Negative refraction in photonic crystals

A photonic crystal is based on an alternating sequence of materials having different refractive indices [27]. Depending on the number of spatial directions the refractive index is periodically modulated, one distinguishes between one-, two-, and three-dimensional photonic crystals. For wavelengths much larger than the periodicity, an incoming wave "sees" an effective homogeneous medium just as in the case of a metamaterial. As for metamaterials, the wave cannot resolve the fine details of the structure and hence "sees" a medium with an effective refractive index. For wavelengths comparable to the lattice constant, diffraction occurs and the medium cannot be described in terms of an effective medium anymore. However, for photonic crystal the interesting wavelengths of light are comparable to the lattice constant [48]. Therefore, we refer to a photonic crystal if the wavelength of light is comparable or smaller than the lattice constant. Otherwise, we talk about metamaterials.

In photonic crystals, diffraction can lead to complicated dispersion relations and hence complex iso-frequency curves can exist. Furthermore, photons in photonic crystals behave similar to electrons in solids or any periodic potentials. In optics, the potential is given by the periodic modulation of the permittivity $\varepsilon(\boldsymbol{r}) = \varepsilon(\boldsymbol{r} + \boldsymbol{R})$ or the refractive index, respectively, in which the vector $\boldsymbol{R}$ consists of any primitive unit vector [48]. As a result, waves propagating in a photonic crystal are Bloch modes, i.e., plane waves multiplied by a vectorial function with the periodicity of the underlaying Bravais lattice – in complete

analogy to electrons in solids. Regarding these Bloch waves, it is questionable to talk of phase velocities sine we do not have plane waves anymore.

We are interested in the refraction of a wave impinging onto a photonic crystal. Exemplarily, for a fictitious photonic crystal the refraction of a wave is depicted in Fig. 3.2. The frequency ω of the wave in vacuum is identical to the one in the photonic crystal. For our fictitious photonic crystal we assume a six-fold iso-frequency curve. Here, the parallel component of the wave vector $\boldsymbol{k}_{||}$ at the interface is conserved modulo a reciprocal lattice vector. For simplicity, we consider the zeroth diffraction order only, i.e., we neglect any reciprocal lattice vectors. For this reason, we obtain an intersection of the wave vector with the iso-frequency curve. As a result, we get the direction of the group velocity and hence the direction of the energy flow. In our fictitious photonic crystal we obtain the results depicted in Fig. 3.2. It is clearly visible that the parallel component of the Poynting vector changes sign at the interface which leads to negative refraction. However, the normal component of the wave vector stays positive. Already at the end of the 80's, Russell [54] and Zengerle [55] independently showed negative refraction employing photonic crystals. In our example we have $\boldsymbol{k}'_{||} \cdot \boldsymbol{S}'_{||} < 0$ and $\boldsymbol{k}'_{\perp} \cdot \boldsymbol{S}'_{\perp} > 0$. Using photonic crystals it is even possible to realize $\boldsymbol{k}'_{||} \cdot \boldsymbol{S}'_{||} < 0$ and $\boldsymbol{k}'_{\perp} \cdot \boldsymbol{S}'_{\perp} < 0$, i.e., the wave vector in the photonic crystal points towards the interface. This configuration of Poynting vector and wave vector also occurs in a medium with a negative refractive index. However, the situation in the photonic crystal is based on diffraction. Thus, it cannot be describe in terms of an effective medium because the the periodic modulation of the refractive index (or the electric permittivity) is of crucial importance. For wavelengths much larger than the lattice constant, i.e., in the effective material limes, dispersion relations leading to negative refraction do no exist.

Although it is possible to realize negative refraction with a photonic crystal, it strongly differs from materials with $n = -1$ when talking about imaging properties. For materials with $n = -1$, it is in principal possible to achieve a perfect image, while using photonic crystals the resolution is limited by the periodicity. Furthermore, evanescent waves are normally not recovered in a photonic crystal as it is the case for materials with $n = -1$.

3.3 Negative refraction in thin, homogeneous, and isotropic materials

We already know that anisotropic materials can lead to negative refraction. However, even for isotropic materials with a positive refractive index negative refraction can occur. First, we consider a metallic mirror followed by the discussion of thin metallic films and thin homogeneous and isotropic dielectric materials.

3.3.1 Physics of a metallic mirror

An electromagnetic wave can penetrate a metal only up to the skin depth. This is caused by the negative real part of the permittivity. The resulting refractive index is mainly imaginary.

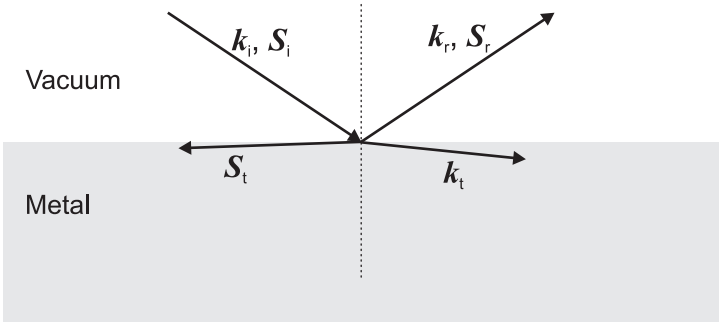

Figure 3.3: A p-polarized plane wave with wave vector $\boldsymbol{k}_\mathrm{i}$ and with Poynting vector $\boldsymbol{S}_\mathrm{i}$ impinges onto a metallic mirror. The resulting real part of the wave vector $\boldsymbol{k}_\mathrm{t}$ and the resulting time-averaged Poynting vector $\boldsymbol{S}_\mathrm{t}$ in the metal are schematically depicted. In the metal, the plane wave is evanescent. Poynting vector and wave vector point into different directions in the metal although the metal is homogeneous and isotropic. Furthermore, the parallel component of the Poynting vector changes sign at the interface which leads to negative refraction.

For silver, for instance, the refractive index is $n = 0.05 + 4.3\mathrm{i}$ at a wavelength of $\lambda = 650\,\mathrm{nm}$ [23].

What happens at the interface between vacuum and metal? In the following we restrict ourselves to a more qualitative discussion. We consider oblique incidence of light and p-polarization. The parallel component of the wave vector of light $\boldsymbol{k}_{||}$ is conserved at the air/metal interface (and, hence, the parallel component of the phase velocity of light keeps its sign). In contrast, the parallel component of the time-averaged Poynting vector $\boldsymbol{S}$ [16]

$$\langle \boldsymbol{S} \rangle = \frac{1}{2} \mathrm{Re} \left(\boldsymbol{E} \times \boldsymbol{H}^* \right) \tag{3.3}$$

(* denotes the complex conjugate) changes sign. Here, we discuss the time-averaged Poynting vector since we deal with complex quantities. The time-averaged Poynting vector changes sign because the normal component of the $\boldsymbol{E}$ field jumps discontinuously at the interface and changes sign. The origin for this behavior is the negative metal permittivity and the continuous normal component of the $\boldsymbol{D}$ field. The parallel component of the $\boldsymbol{H}$ field is conserved according to Maxwell's equations.

If we analytically calculate the fields, we end up with the time-averaged Poynting vector and the wave vector as depicted in Fig. 3.3. Both Poynting vector and wave vector are almost parallel to the interface, because the normal components of both vectors are small. For the normal component of the wave vector, for instance, the imaginary part is much larger than the real part. Furthermore, both vectors point into different directions. The parallel component of the Poynting vector changes its sign at the interface. Thus, we obtain $\boldsymbol{k}_{||,\mathrm{t}} \cdot \boldsymbol{S}_{||,\mathrm{t}} < 0$ and $\boldsymbol{k}_{\perp,\mathrm{t}} \cdot \boldsymbol{S}_{\perp,\mathrm{t}} > 0$. Since the Poynting vector describes the direction of the energy flow, the light is refracted to the "wrong" side in the metal. This effect has consequences for the reflection properties of a metallic mirror [56]: If a p-polarized Gaussian beam impinges on a mirror, it gets a negative lateral displacement at the interface. Thus, it appears as if the beam was reflected before the mirror.

The change of the sign of the parallel component of the Poynting vector in the metal can be exploited in special waveguides [57, 58]. These special waveguides consist of a dielectric

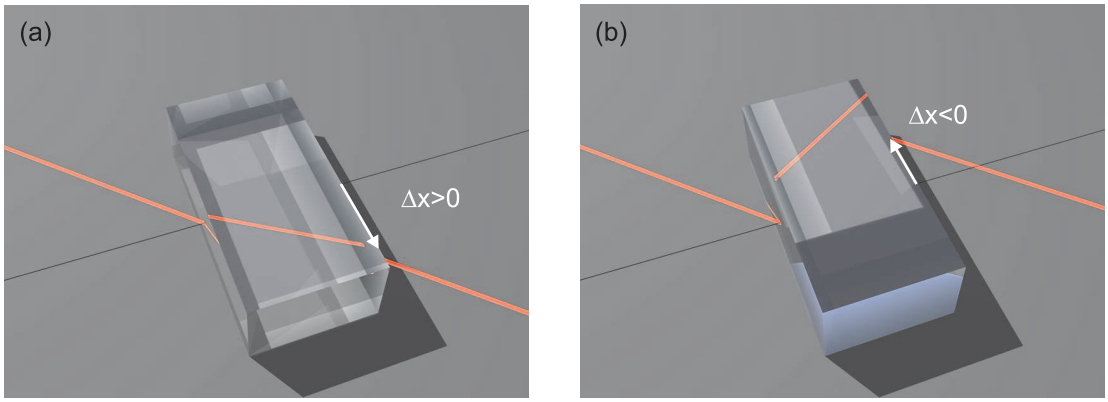

Figure 3.4: In ray optics, a positive real part of the refractive index ($\mathrm{Re}(n) > 0$) leads to a positive beam displacement Δx (a), while the displacement is negative (b) for a negative refractive index ($\mathrm{Re}(n) < 0$). In wave optics, however, the relation is not so simple. Even a single, thin (isotropic and homogeneous) metal film with $\mathrm{Re}(n) > 0$ can lead to negative displacements, hence to negative refraction.

material with metals on its top and bottom. If the dielectric is thick, the metals act just as mirror. If the thickness of the dielectric material is reduced further and further, more and more energy is transported inside the metals. Below a certain thickness, more net energy is transported inside the metals than inside the dielectric. If light impinges onto such a metal-dielectric-metal structure, the light will be negatively refracted. Recently, such a situation has been experimentally demonstrated [59]. However, the fact that most energy is transported inside the metals leads to high losses. In the experiments, for instance, the absorption lengths was only 50 nm for green light. Furthermore, negative refraction in metal-dielectric-metal waveguides is restricted to two-dimensional geometries.

3.3.2 Thin metal film

In the case of a metallic mirror, no light is transmitted. Therefore, we now discuss a thin, homogeneous, and isotropic metal film with finite transmission. We are interested in beam displacement after propagation through the film with respect to the normal. Relevant notations are found in Fig. 3.4. It shows two different materials with $\mathrm{Re}(n) > 0$ (a) and $\mathrm{Re}(n) < 0$ (b), respectively. In (a), the beam leaves the medium on the usual side with respect to the normal which corresponds to a positive beam displacement $\Delta x > 0$. In (b), the beam displacement $\Delta x < 0$ is negative.

In order to obtain a beam displacement, we need a modulation of the intensity at the interface, e.g, a Gaussian beam. But it is also sufficient to superimpose two plane waves of the same wavelength but different angles of incident α and $\alpha + \delta$. For this situation the intensity at the interface is modulated by $\cos^2$.

To calculate a beam displacement we use the transfer-matrix method for oblique incidence of light. A detailed derivation can be found in appendix A. Applying the transfer-matrix method we calculate the fields of both plane waves at the rear side of the metal. By superposition we get the required intensity modulation and thus we can calculate the beam displacement. We also have compared our results obtained from two plane waves and a

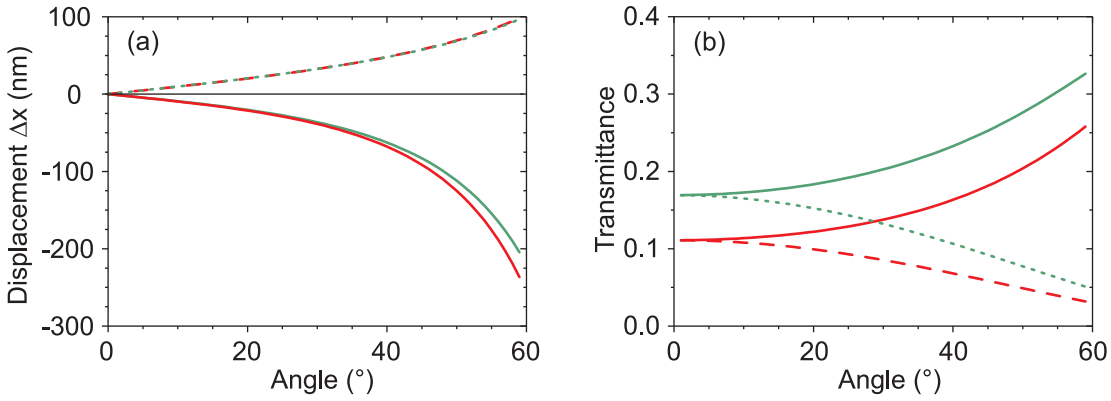

Figure 3.5: (a) Beam displacement Δx for a $d = 25\,\text{nm}$ thin silver film embedded in vacuum. Dashed (solid) lines correspond to s-(p-)polarization. Red (green) lines correspond to a wavelength of $\lambda = 650\,\text{nm}$ ($\lambda = 532\,\text{nm}$). (b) Transmittance for the different configurations.

Gaussian beam. We have found no difference if the value of δ between the angles is small.

In our example, we employ a $d = 25\,\text{nm}$ thin, isotropic, and homogeneous metal film which is embedded in vacuum. The refractive index at the wavelength of $\lambda = 532\,\text{nm}$ ($\lambda = 650\,\text{nm}$) is $n = 0.05 + 3.4\text{i}$ ($n = 0.05 + 4.3\text{i}$) [23]. Figure 3.5(a) shows our results from the calculations of the beam displacement for p- and s-polarized light. In (b), the corresponding transmittance of the thin metal film is depicted. In s-polarization the beam displacement is positive as one would expect for a positive refractive index $\text{Re}(n) > 0$. Since the refractive index is close to zero, the beam should be refracted far away from the normal. The differences between green and red light are negligible. However, for p-polarization the beam displacement is negative. Furthermore, its absolute value is larger than that of the positive beam displacement in s-polarization. The negative beam displacement can be explained by the physics of the metallic mirror. According to Snell's law a thin, isotropic and homogeneous metal film would have a negative refractive index for p-polarization and a positive refractive index for s-polarization which is obviously wrong. Furthermore, for thin films another effect gains in importance as we discus in the following.

3.3.3 Thin dielectric film

Next, we consider a thin, isotropic, and homogeneous dielectric film with a refractive index of $n = 1.5$. In thin films the interference effects caused by the interfaces are important. For example, if we take a $d = 25\,\text{nm}$ thin film, embed it in vacuum and send in light of a wavelength of $\lambda = 650\,\text{nm}$, we get the beam displacement presented in Fig. 3.6. Obviously, we obtain a negative beam displacement for s-polarization and a positive beam displacement for p-polarization. If we increase the thickness of the film, however, hardly any negative refraction occurs for the depicted range of incident angles. The origin of the behavior stems from the fact that for $d \gg \lambda$ the interference effects of the interfaces become negligible.

In conclusion, we have seen different configurations in which we obtained negative refraction at an interface. This negative refraction phenomena can have various origins: In

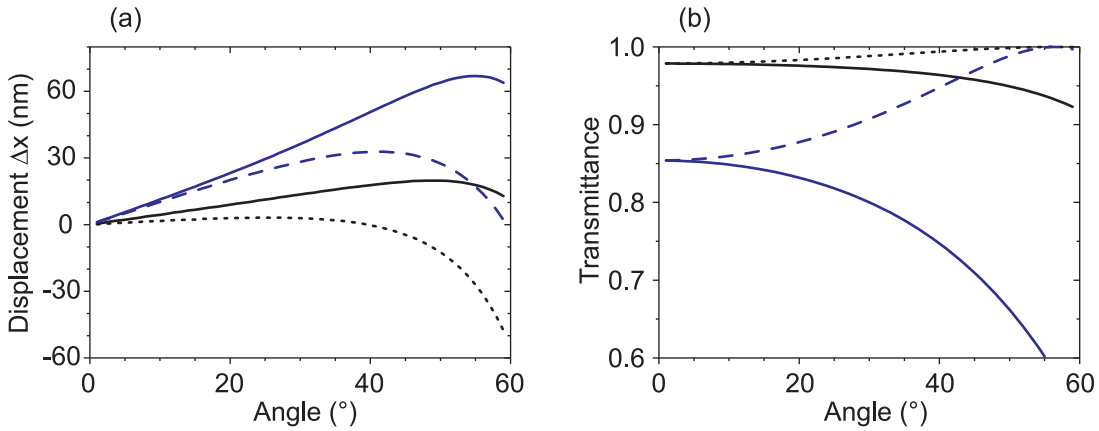

Figure 3.6: (a) Beam displacement Δx for a thin isotropic film with refractive index $n = 1.5$ embedded in vacuum. Dashed (solid) lines correspond to s-(p-)polarization. Black (blue) corresponds to a film of thickness $d = 25\,\text{nm}$ ($d = 100\,\text{nm}$). (b) Transmittance for the different configurations. The wavelength is $\lambda = 650\,\text{nm}$.

birefringent materials the anisotropy can lead to positive and negative refraction depending on the angle of incidence. In photonic crystals the periodically modulated refractive index may lead to negative refraction. The last example even showed negative refraction for homogenous and isotropic films. This discussion clearly shows that one generally has to be careful when talking of refractive index or refraction.

Chapter 4

Fabrication, characterization, and simulation

The metamaterials discussed in this thesis are fabricated by electron-beam lithography (EBL). This technique provides the possibility to fabricate structures with feature sizes of few tens of nanometers. Furthermore, using a scanning-electron microscope (SEM) the topography of the final sample can be measured with an accuracy of a few nanometers. Thus, we can check if the fabricated sample has the required dimensions and microscopic quality. Important steps for the sample fabrication are described in section 4.1.

For the optical characterization of our metamaterial samples we used two distinct optical setups. A home-built setup is used to measure angle-resolved transmittance spectra in the spectral range of 500 nm to 1.8 µm wavelength. In addition, this setup offers the possibility to perform reflectance measurements in normal incidence of the incoming light. Furthermore, we built up a Michelson interferometer to perform pulse propagation experiments on the metamaterial samples. This allows the determination of phase velocity and group velocity. All optical setups are described in section 4.2.

Experimental results were always compared to corresponding simulations. There are several simulation techniques available. Using the finite-difference time-domain (FDTD) software package MicroWave Studio (MWS), we can calculate the complete spectrum of a structure within in few minutes. However, since this tool is restricted to the case of normal incidence of the incoming light, we also used the finite-element (FEM) software package JCMsuite. This offers the opportunity to simulate the spectra for oblique incidence. Furthermore, we compared the calculations between MWS and JCMsuite for consistency. From the results of the simulations we calculated the effective refractive index of the metamaterials. Section 4.3 summarizes the numerical methods.

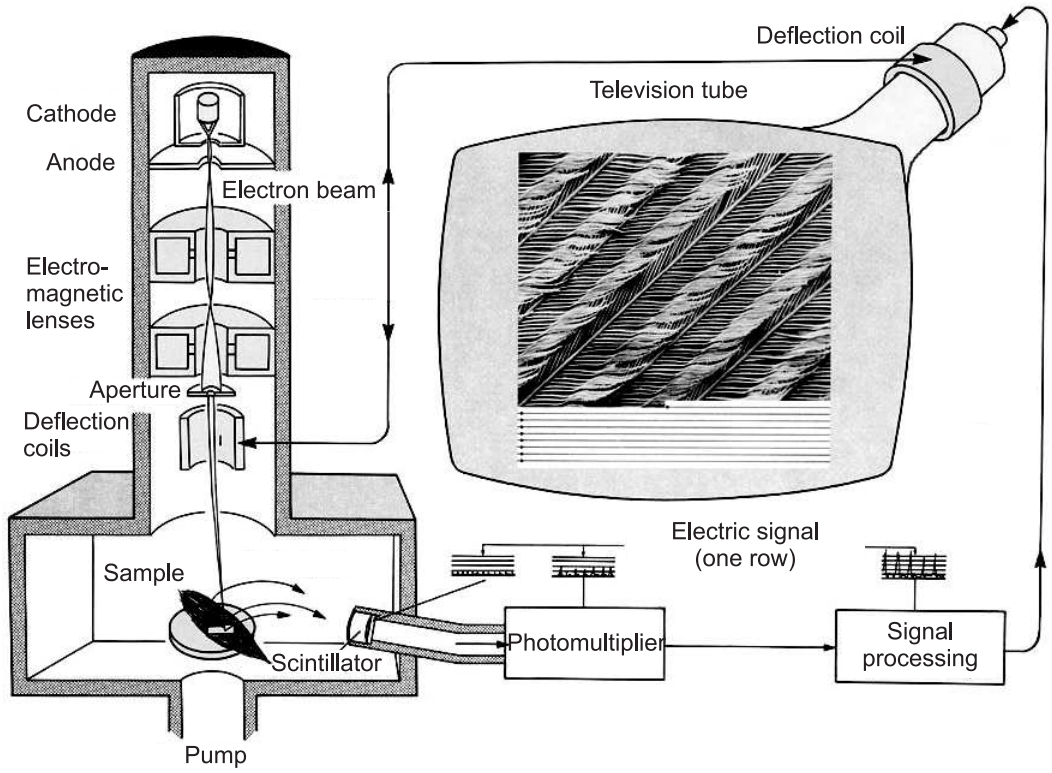

Figure 4.1: The setup of a scanning-electron microscope is schematically depicted. Copyright: [60]

4.1 Fabrication

4.1.1 Scanning-electron microscope

Conventional optical microscopes offer a limited resolution which is roughly given by half of the wavelength of light. One possibility to achieve higher resolution is the use of a scanning-electron microscope (SEM). Its forerunner method, the transmission electron microscope (TEM), was first described in 1932 by Knoll and Ruska [61], for which Ruska was awarded the Nobel Prize in 1986. As early as 1939, the TEM was commercialized by the company Siemens und Halske AG and went into sale. The first SEM was constructed by Zworykin, Hiller and Snyder in 1942 [62] and showed a resolution of down to $50\,\mathrm{nm}$ already.

The operating mode of the SEM is comparable to a conventional television. An electron beam is focused onto a sample and deflected to scan over a certain area. The setup of such a scanning-electron microscope is sketched in Fig. 4.1. At the top, the electron source is located. Emitted electrons are accelerated and focused *via* electric and magnetic fields. An aperture right at the focus shields undesired outer areas of the beam. Further focusing, removal of outer regions of the beam, and well-defined deflection allow for scanning the focused beam over the sample. The signal (cf. below) is directly displayed on a screen, since the scanning of the sample itself is identical to the scanning of a television screen (see Fig. 4.1). Furthermore, the signal can be converted into a digital one to be further processed with a computer. In order to avoid collisions of the electron beam with gas molecules, the

interior of the SEM is evacuated.

In the following sections the fundamental components of the SEM are described. For further details we refer to [63–65].

Electron source

In principle, one distinguishes two different methods to emit free electrons from the source. In a thermal electron source the cathode material is heated to such a high temperature that the kinetic energy of the electrons exceed the work function of the material. Alternatively, applying a sufficiently high electric field to a conductor can cause the electrons to leave the conductor. Today, usually a thermal source combined with high electric fields is used, as it is long-lasting and provides a constantly high power. Crucial quality parameters are the virtual size of the source (as small as possible), the "brightness" (as many electrons per unit solid angle as possible) and the energy distribution of the emitted electrons (as narrow as possible). The latter is deteriorated by Coulomb interaction of the electrons. Thus, right in the foci the energy distribution of the electrons is broadened, called Boersch effect [66].

Lenses

In analogy to ray optics, lenses for electrons are required in a SEM to provide a well-focused and directed electron beam. The electrons are focussed by electrostatic and magnetic forces. Magnetic lenses exploit the Lorentz force to direct the electrons towards the optical axis. However, at the same time the electrons are rotated along the optical axis. This property does not effect the focusing quality, but has a strong influence on the actual setup of the electron microscope. Depending on the focusing, the image is rotated differently, which has to be corrected appropriately. Besides magnetic lenses, one also has the opportunity to focus the electron beam *via* electric fields. Yet, in this case the chromatic and spherical aberrations are much larger than for magnetic lenses, which means that generally magnetic lenses are preferred. The term chromatic aberration denotes that electrons of different energy are focused differently. Spherical aberrations of electron lenses are characterized by a stronger focusing power of the exterior regions than the interior regions of the lens.

Further crucial components

Apertures are tiny holes in the beam path which cut off the exterior regions of the beam. Thus, these apertures are used similarly to apertures in optics. The deflection of the beam during scanning is again generated electrically or magnetically. Yet, alternating fields are applied. However, if the beam is deflected from the optical axis, additional abberations are introduced, which have to be corrected by additional lenses. Magnetic lenses for deflection again cause smaller aberrations than corresponding electric lenses. The self-induction of the coil has to be considered, which deteriorates the beam quality. Furthermore, due to focusing and deflection, the beam becomes astigmatic, i.e., the focal spot becomes oval-shaped. All components must be screened in order to avoid disturbing interaction effects.

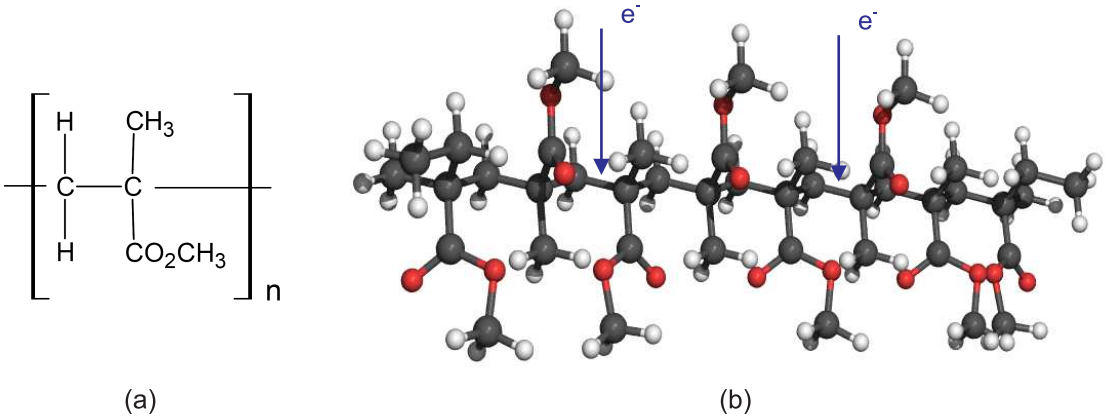

Figure 4.2: (a) Chemical structure of PMMA. (b) PMMA molecule consist of oxygen atoms (red), carbon atoms (black) and hydrogen atoms (white) and the corresponding bonds. The electrons (blue) are able to break the chemical bonds, if they have sufficiently high energy.

Detection

When the electron beam hits the sample, there are basically two possibilities to detect the signal: First, electrons which are scattered back off the sample or reflected can be detected. These electrons mainly have energies of some keV. The corresponding detector is located directly at the bottom end of the electron column. The second possibility is to detect secondary electrons, which are excited in the object by the primary electrons of the focused electron beam and which finally escape the sample. The energy of these electrons is usually just a few electron volts. In order to detect these low-energy electrons an additional grid is mounted in front of the detector to generate an electric field between detector and grid. Thus, the electrons gain additional kinetic energy and are finally detected by a so-called Everhart-Thornley detector.

In order to study a non-metallic sample, it has to be coated by a thin film of a an electrically conducting material. Otherwise, the material under observation gets charged due to the large amount of electrons hitting the sample.

4.1.2 Electron-beam lithography

The scanning-electron microscope can be used for lithography with only few modifications required. Thus, already at the end of 1960 it was possible to “write” structures with such an extended SEM [67].

For lithography it is important that the electron beam is not scanning the sample continuously, i.e., it is necessary to be able to switch the electron beam on and off. This is realized by adding a condenser right before the first aperture, which can switch sufficiently fast (on the order of some tens of nanoseconds) to deflect the beam onto the aperture. Furthermore, some more deflecting coils are added to the initial microscope setup. These coils are computer-controlled to ensure that the electron beam scans merely predefined regions of the sample.

Additionally, an appropriate resist is required. This resist is chemically modified by the impinging electrons in a way that an appropriate solvent can etch away those regions which are either scanned by the electron beam (positive resist) or not scanned (negative resist). In the following, the positive resist polymethylmethacrylat (PMMA) is discussed, which we used for the lithography in the course of this thesis. The structural formula is depicted in Fig. 4.2(a). Several kinds of PMMA exist, differing in the length of the molecular chains. For the "double-fishnet" design we have used only 950k PMMA dissolved in anisole by 4 per cent supplied by the company Microchem. If electrons of sufficiently high energy hit the molecular chains, the chemical bonds can be broken [cf. Fig. 4.2(b)]. Due to broken bonds the exposed resist is etched by the solvent methylisobutylketon (MIBK) mixed with isopropyl alcohol at the ratio 1:3. The sensitivity of the resist PMMA is determined by the length of the molecular chains. The longer the chains, the lower the sensitivity of the resist.

However, the resist is not only exposed by primary electrons. A high-energetic electron generates many secondary electrons in the resist, which can expose the resist as well. While the primary electrons penetrate the resist at well-defined positions, the generated secondary electrons are scattered off in all directions. Thus, if one writes two structures close to each other, it can happen that after the development process just one connected structure remains instead of two separated ones. This is caused by the undesired background exposure of the secondary electrons. This effect, limiting the maximum resolution of the lithography, is called proximity effect. Thus, if the structure which one fabricates by lithography is modified or changed to a complete new design, one has to do so-called dose-tests, to experimentally determine the ideal value of the dose for exposing the resist.

In this thesis we used the area dose $100\,\mu\text{C/cm}^2$ as a starting point and varied the dose systematically to determine the best exposing conditions depending on the actual structure.

4.1.3 Sample preparation

The different steps for the complete fabrication process of our samples are schematically depicted in Fig. 4.3.(a) We use pure fused quartz glass substrates (Suprasil), which are polished to $\lambda/10$. The substrates have a thickness of $1\,\text{mm}$ and an area of $1\,\text{cm}^2$. After cleaning the substrates, a thin layer of $5\,\text{nm}$ indium-tin-oxide (ITO) is deposited. In order to obtain hard and transparent ITO films, the evaporated substrates are annealed for four hours at 450°C in normal atmosphere. Since the ITO film is conductive, it prevents undesired charging effects of the resist during lithography. Furthermore, ITO is a transparent material at optical frequencies and does not affect the optical properties of the final structure. Additionally, metals like silver and gold stick well to ITO. (b) Next, the resist 950k PMMA is spin-coated onto the substrates at 500 rounds per minute (rpm) for five seconds followed by 2000 rounds per minute (rpm) for 45 seconds. Afterwards, they are baked for 30 minutes at 170°C in an oven. (c) The desired structures are designed on the computer using the CAD software Elphy. Afterwards, the structures are written into the resist using an electron-beam lithography system of Zeiss (SUPRA 55 VP). The writing procedure is controlled by the hardware of Raith. The accelerating voltage is set to $10\,\text{keV}$ or $30\,\text{keV}$. (d) Subsequently, the substrate is put into the solvent MIBK mixed with isopropyl alcohol for 16 seconds in order to etch away the

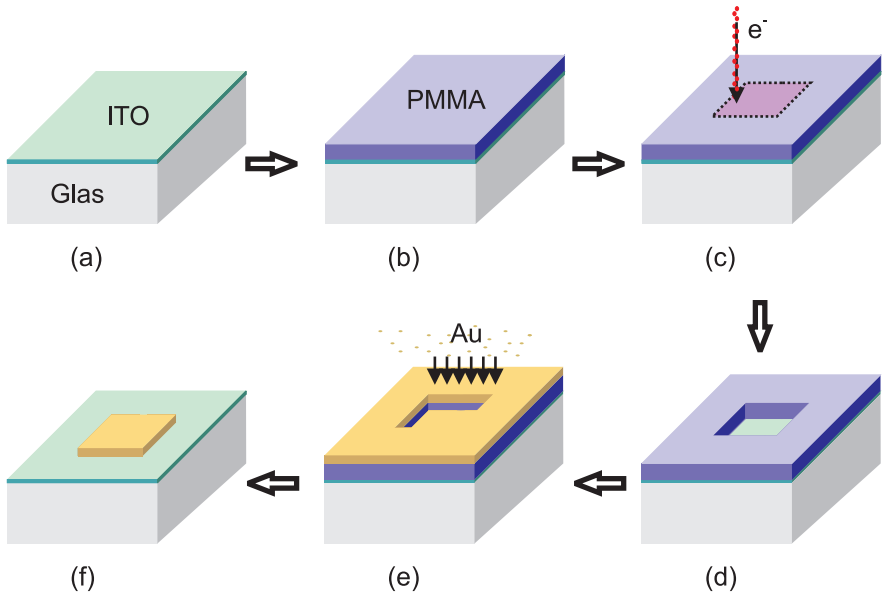

Figure 4.3: The different processing steps required to fabricate a sample are schematically depicted in (a)-(f). In this case we chose a simple gold pad as example.

exposed resist. Afterwards, the developed sample is put into isopropyl alcohol for further 30 seconds to stop the etching process. Finally, the sample is dried with nitrogen. (e) The requested materials are evaporated on top of the developed sample. This evaporation process takes place in a vacuum chamber at a pressure below 10^{-6} hPa. Inside, an electron beam is focussed onto the target material. Due to the fast electrons the material gets punctually heated up to the boiling temperature. The generated atom vapor beam is strongly directed and produces very homogeneous films of thicknesses controllable on the nanometer scale. (f) For removing the abundant film the sample is put into a 50°C hot acetone bath for several minutes. The acetone dissolves the unexposed PMMA-film and thus, rips off the abundant film. To further assist this process, an ultrasonic bath was used partially.

Electron-beam lithography has the big advantage that virtually any two-dimensional structure can be written with a resolution of down to 10 nm. However, electron-beam lithography works serially and, hence, only very small areas can be produced in a reasonable time. Thus, in this thesis the sample size is restricted to 100 µm × 100 µm. Larger samples in the range of square centimeters can be fabricated by interference holography. Further details to this technique can be found in [68].

4.2 Optical characterization

We used a home-built setup for angle-resolved transmittance spectroscopy. The setup also allows for reflection measurement for normal incidence of the light. Additionally, since the refractive index is defined by the phase velocity, a Michelson interferometer was built up to measure the phase delay. In the following subsections, the experimental setups are described in more detail.

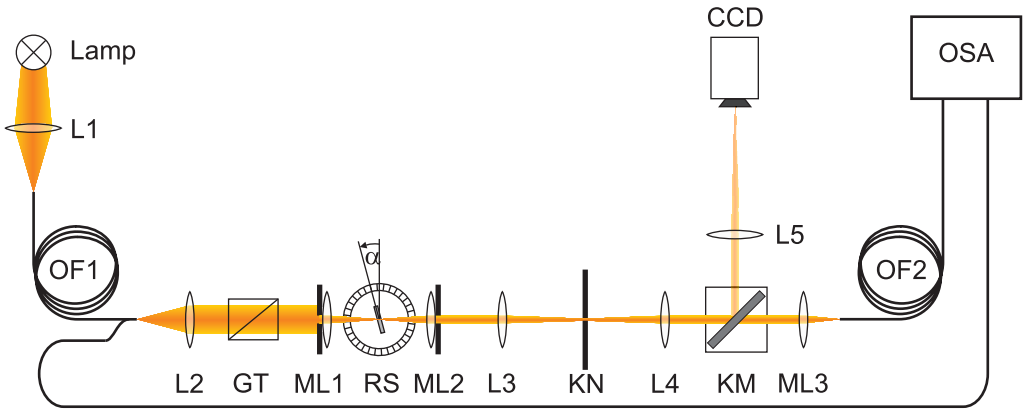

Figure 4.4: Setup for polarization-resolved transmittance and reflectance spectroscopy. In transmission the angle of incidence of the incoming light can be additionally varied. A tungsten halogen lamp is used as a light source. L1: lens, $f = 50.2\,\text{mm}$; OF1: $200\,\mu\text{m}$ core IR/VIS optical fiber with y-splitter; L2: lens , $f = 25.4\,\text{mm}$; GT: Glan-Thompson polarizer; ML1, ML2: microscope objectives with circular apertures, $f = 8\,\text{mm}$; RS: rotation and translational stage with goniometer and sample holder; L3, L4: lenses, $f = 150\,\text{mm}$; KN: intermediate image plane with knife-edge aperture; KM: kinematic mirror; ML3: microscope objective, $f = 16.5\,\text{mm}$; L5: lens, $f = 500\,\text{mm}$; OSA: optical spectrum analyzer

4.2.1 Reflectance and angle-resolved transmittance spectroscopy

All transmittance and reflectance spectra of the double-fishnet structures are measured by a home-made setup (cf. Fig. 4.4), which has been built up by Markus Deubel [69]. Light of a $100\,\text{W}$ tungsten halogen lamp is coupled into an optical multi-mode fiber (OF1) using the lens L1 of numerical aperture $\text{NA} = 0.22$. Afterwards, the light is coupled out again and collimated by lens L2. The light is sent through a Glan-Thompson polarizer and finally focussed onto the sample by the microscope objective ML1 (Zeiss Achroplan LD $20\times$ KO, $\text{NA} = 0.4$). Thus, the core of the fiber is imaged onto the sample. The semi-aperture angle of the setup is 5°, which is assured by the iris diaphragm that reduces the numerical aperture to $\text{NA} = 0.088$. The sample holder is fixed to a goniometer, which in turn is mounted on top of a rotation stage. The combination of rotation stage and goniometer offers the possibility to align the sample along the optical axis very accurately. Additionally, the sample can be rotated by a an angle α with respect to the optical axis (see Fig. 4.4). Furthermore, the whole combination is mounted on top of a three-dimensional translational stage to align the sample relative to the focus. The second microscope objective ML2 and lens L3 image the sample onto an intermediate image plane. Using knife-edges, well-defined regions of the sample can be selected. Then, this intermediate image plane is further imaged onto a second IR/VIS fiber with a core diameter of $200\,\mu\text{m}$ (OF2) by lens L4 and microscope objective ML3 (Newport M-$10\times$, $\text{NA} = 0.25$). The output of the second fiber is connected to an optical spectrum analyzer (Ando AG 6315B), covering a spectral range from $500\,\text{nm}$ to $1.8\,\mu\text{m}$ wavelength.

In order to align the sample appropriately on the optical axis, the intermediate image plane can be imaged onto a CCD camera using a kinematic mirror (KM). The magnification of this setup is $62.5\times$, which is sufficient for aligning small objects of several micrometers.

For transmittance measurements we use the substrate covered with ITO as reference. For

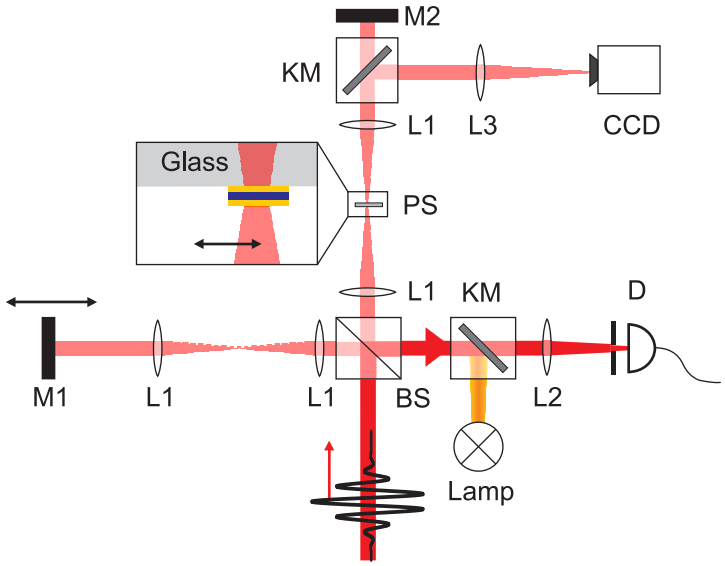

Figure 4.5: Michelson interferometer for time-resolved spectroscopy. To align the sample, an imaging system including a halogen lamp and a CCD camera was built up. BS: non-polarizing 50/50 beam splitter; L1: lens, $f = 75.6$ mm; L2: lens, $f = 75$ mm; L3: lens, $f = 200$ mm; M1: silver mirror on piezo scanning stage; M2: silver mirror; PS: sample holder with three-dimensional piezo scanning stage mounted on a three-dimensional translational stage; KM: kinematic mirror; D: detector

reflectance experiments, the second arm of fiber OF1 is connected to the optical spectrum analyzer, instead of fiber OF2. This measurement setup does not allow for reflection measurements with oblique incidence of light. For reference, a silver mirror is required on the sample. For this purpose, each time an unstructured field was fabricated (by electron-beam lithography) with the same size as the actual sample. As multi-layer systems are evaporated, the layer thickness of silver or gold, respectively, was at least 50 nm, to guarantee a sufficient quality of the mirror on the substrate. Additionally, for reflectance measurements the background has to be subtracted, which is caused by internal reflections at the Y-splitter.

4.2.2 Michelson interferometer

The previously described setup does not allow for phase-sensitive measurements. Hence, we have set-up a compact Michelson interferometer (not actively stabilized) which allows to measure the phase and group delay.

For our measurements we either used 170−fs transform-limited Gaussian pulses derived from an optical-parametric oscillator (OPO, Spectra-Physics Opal) that are tunable around 1.5 µm wavelength, or 125−fs transform-limited Gaussian pulses from a Ti:Sapphire laser (Spectra Physics Tsunami) that are tunable around 800 nm wavelength.

The interferometer setup is illustrated in Fig. 4.5. The beam is split into the two interferometer arms by a non-polarizing 50/50 beam splitter (BS). One arm of the interferometer contains the sample holder on a three-dimensional piezo scanning stage (PS, Piezosysteme Jena Tritor 101 NV, 100 µm linear travel) mounted on a three-dimensional translational stage (Newport ULTRAlign 561D). The beam is focussed by the lenses L1 ($f = 75.6$ mm each).

The laser spot on the sample has a size of about $30\,\mu$m. As the pulse in the sample arm is deformed due to dispersion of the lenses, an identical pair of lenses is placed in the second interferometer arm. The light is reflected by the silver mirrors M1 and M2, where M1 is mounted on a piezoelectric scanning stage (Piezosysteme Jena PX 100, $100\,\mu$m linear travel). The light from the two arms is recombined coaxially in the beam splitter and focused onto the detector (D) by the lens L2 ($f = 75\,$mm). For wavelengths in the infrared regime a germanium detector is used, while for wavelengths around $800\,$nm, a silicon detector is utilized. In each case, the detector is connected to a low-noise current pre-amplifier (Standford Research System SR570). The voltage output of the pre-amplifier is connected to the analog-digital converter of a PC board (National Instruments PCI-MIO-16XE10). The same board is used to control the scanning operation of the piezo stage with the mirror. The scanning operation and the data acquisition are hardware-synchronized and therefore independent of the time base of the controlling system. The data is recorded as a function of the length of one of the interferometer arms, which can be immediately translated into an interferometer time delay. A LabVIEW program provides a graphical user interface to set all the scanning parameters and displays the data acquired by the PC board. Additionally, the software offers the opportunity to move the sample in and out of the laser spot via the three-dimensional piezo stage. In this manner, the interferograms of the glass substrate and subsequently of the metamaterial structure on the substrate are measured within $2\,$s acquisition time. The glass substrate is in the optical path in either case, hence it drops out when considering the difference in the interferograms. The complete procedure is repeated at least 20 times. In this fashion, we can identify possible drifts of our setup. Typically we find drifts smaller than 100 attoseconds throughout the procedure.

The time line of the interferometer is calibrated via the $\lambda = 632.8\,$nm line of a Helium-Neon laser. The mirror M2 was adjusted such that the reflected light of the glass side of the sample overlaps with the back reflection of the mirror M2, since the sample is aligned perpendicular to the beam. Afterwards, the mirror M1 was aligned to have optimum interference of the pulses both in space and time. Therefore, the ratio of mean intensity and minimum intensity of the interferogram is optimized. For the alignment of the sample with respect to the focus of the laser the kinematic mirrors (KM) can be inserted into the setup. Using the light of a halogen lamp the sample with the laser spot can be imaged onto a CCD camera.

4.3 Numerical methods

In order to compare our experimental results with theoretical expectations, we have used two different simulation tools. The first program is Microwave Studio (MWS) developed by CST GmbH. This program offers a simple and intuitive graphical interface. The calculation of a single spectrum takes less than half an hour on a standard PC with this program. The second program is JCMsuite, programmed by the Nano-Photonics group of Frank Schmidt at the Zuse Institut Berlin. This program is distributed by the company JCMWave. To meet our requirements the program was upgraded accordingly. Achim Schädle dealt with the calculations for our structures. Calculating one frequency point of the spectrum takes more

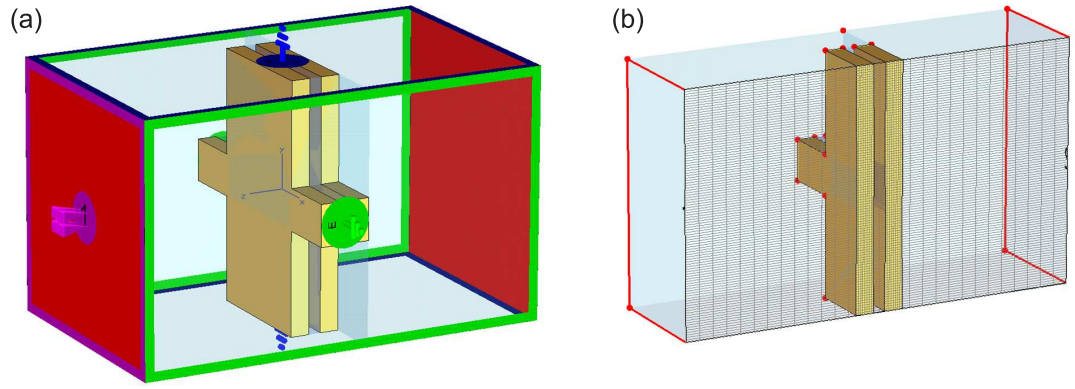

Figure 4.6: View of a structure in MWS. In (a) the "waveguide geometry" is depicted. Here, a unit cell of the double-fishnet structure is embedded in vacuum. Additionally, the so-called ports (red) and the boundary conditions are shown. (b) illustrates the discretization of the structure taken from the software.

than ten minutes on a standard PC.

Using the data of these programs we can calculate the transmittance and reflectance spectra as well as the interferograms which we measure in the time-resolved experiment. Furthermore, it is possible to derive the refractive index and the impedance of the respective structures from the numerical data.

4.3.1 MicroWave Studio

MicroWave Studio supports several different simulation modes. The amplitudes and phases in both transmission and reflection of a three-dimensional structure can be calculated either in frequency domain or in time domain. The structure is discretized by an automatic expert system [cf. Fig. 4.6(b)]. Thus, simulations can be performed without a detailed knowledge of simulation techniques. The user interface follows CAD programs and provides an intuitive handling. Thanks to the graphical interface it is also possible to inspect field distributions for a given structure as a video sequence or a series of snapshots.

For our simulations we merely used the transient solver for calculating the amplitudes and phases and the field distributions. The corresponding calculations operate in the time-domain, i.e., the development of the fields is computed at discrete time-steps at discrete points in the simulation volume. This ansatz is known as finite-difference time-domain (FDTD) method and is based on K. S. Yee's work from the year of 1966 [70].

In order to simulate the double-fishnet structure we have adopted the "waveguide geometry" [cf. Fig. 4.6(a)]. The structure is constructed using the CAD interface and it is embedded in vacuum or located on a glass substrate. This determines the simulation volume. The permittivities of the different components can be set individually. At one port (red area) a pulse is launched into the simulation volume and the outward propagating signals are detected at both ports. Furthermore, we have to define the conditions at the boundaries of the volume. At the side of the ports, open boundary conditions (purple) are chosen (otherwise the pulse cannot be launched into the simulation volume). As it is not possible to employ

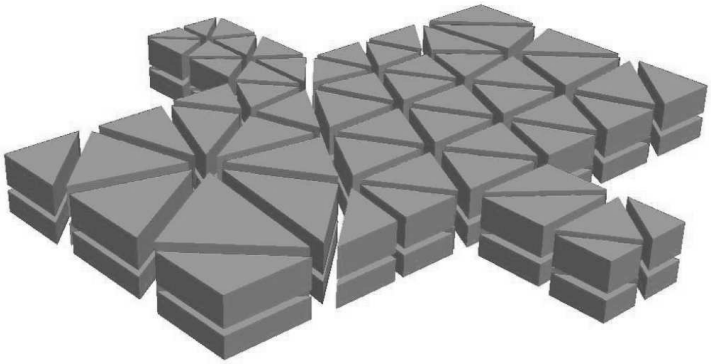

Figure 4.7: Exemplarily discretization of the upper layer of the double-fishnet structure as prisms. Most calculations for the double-fishnet structures are computed by JCMsuite with similar resolution.

periodic boundary conditions with this program in the time domain, we have have to set the tangential component of either the electric (green) or the magnetic field (blue) to zero at the remaining boundaries. This also determines the polarization of the incident pulse and "simulates" periodic boundary conditions. From the simulation we finally obtain the amplitudes and phases in transmission and reflection in the selected frequency range. During a simulation run, field distributions can be calculated and subsequently illustrated for selected frequencies which are contained in the pulse.

With personal a computer with dual-core Xeon CPU of 3.0 GHz and 2 GByte memory, one of these calculations lasts generally less than half an hour.

4.3.2 JCMsuite

Currently, MWS can only be used to simulate our structures for normal incidence. In order to overcome this problem, we used the finite-elements method (FEM) which operates in the frequency domain. The simulations were performed by Achim Schädle using JCMsuite.

By default, Bloch-periodic boundary conditions for the x- and y-directions [71] are applied. In the $\pm z$-direction we define transparent boundary conditions based on the perfectly-matched-layer method [72, 73]. We discretize a unit cell with an unstructured mesh of about 600 prisms (an example is depicted in Fig. 4.7). Maxwell's equations are discretized using vectorial finite elements (Whitney elements) of second order polynomial, leading to a sparse matrix equation with about 130 000 unknowns. For one frequency point, the calculation takes more than ten minutes on standard PC.

4.3.3 Calculating an interferogram

In order to compare the measured interferogram of the Michelson interferometer with theory, a Matlab script was written. Two Gaussian pulses of the form

$$E(t) \quad = \quad e^{-\frac{t^2}{2w^2}} \cdot e^{-\mathrm{i}\omega_0 t} \tag{4.1}$$

with the central frequency ω_0 and the width w are superimposed. The first pulse is modified by the metamaterial. The second pulse is shifted by τ in time with respect to the first pulse. In order to calculate the interferogram, we switch to the frequency domain. The superposition of the pulses is given by

$$E(\omega,\tau) \;=\; f(\omega)^2 \cdot E(\omega) + e^{-\mathrm{i}\omega\tau} \cdot E(\omega) = \left(f(\omega)^2 + e^{-\mathrm{i}\omega\tau}\right) E(\omega). \tag{4.2}$$

Here, $f(\omega)$ represents the transmission function of the metamaterial layer. This function can be extracted from MWS. Since we use a Michelson interferometer, the pulse passes our sample twice, which means that the transmission function enters as squared. To obtain the reference interferogram, $f(w)$ is substituted by the phase delay which corresponds to the propagation of a plane wave in vacuum for the thickness of the metamaterial layer. Additionally, we have exploited that the Fourier transform of the second pulse $E(t-\tau)$ is given by $\exp[-\mathrm{i}\omega\tau] \cdot E(\omega)$.

The detector in the experiment measures the average intensity I which depends on the time delay τ:

$$I(\tau) \;=\; \int_0^\infty \left|E(\omega,\tau)\right|^2 d\omega. \tag{4.3}$$

The calculated interferograms are analyzed by another Matlab script. This script was also used to analyze the experimental data. Thus, the following procedures are identical for both experiment and theory. First, maxima and minima of each fringe of both the metamaterial and reference interferograms are determined. By comparing the interferometer delay of the corresponding extremes the phase delay is identified. However, this procedure is not unambiguous. For instance, one maximum of the reference interferogram can lie between two maxima of the metamaterial interferogram. For the phase delay, the Matlab program specifies the interferometer delay of the respective maxima, resulting in two phase delays. To choose the right phase delay, the metamaterial has to be optically thin compared to the operational wavelength. As a result, the phase delay caused an optically thin metamaterial is much smaller than one oscillation of light. This is fulfilled for all metamaterials under investigation in this thesis and, hence, the right phase delay can be chosen. The sum of both phase delays is the time period of one oscillation of the central frequency of the Gaussian pulse. In addition to the phase delays, the corresponding standard deviations are calculated.

To determine the group velocity, we have performed a least-squares fit of a Gaussian curve to the envelope of the interferogram. Additionally, we obtain the central wavelength and the transmission coefficient. The latter can be compared to transmission measurements performed with a different setup. Thus, we have the possibility to check our data for consistency.

4.3.4 Retrieval of the refractive index and the impedance

Based on the complex-valued amplitude transmittance coefficient (t) and the complex-valued amplitude reflectance coefficient (r), we can derive both the effective refractive index n and

the effective impedance Z of the simulated layer. From these values we can subsequently compute the effective permittivity $\mu = n \cdot Z$ and the effective permeability $\varepsilon = n/Z$ of the structure. The impedance is given by [41, 74]:

$$Z = \pm Z_i \cdot \sqrt{\frac{\left[\frac{1+r}{t} - \cos\left(n\, k_0\, d\right)\right]^2}{-Z_c^2\left(1 - \cos\left(n\, k_0\, d\right)^2\right)}} \tag{4.4}$$

with

$$\cos\left(n\, k_0\, d\right) = \frac{1 - r^2 + Z_c t^2}{t\left(1 + Z_c + r(Z_c - 1)\right)}. \tag{4.5}$$

Z_i (Z_t) is the impedance of the material before (behind) the metamaterial layer. d is the thickness of the layer. The value Z_c is given by $Z_c = Z_i/Z_t$. The algebraic sign in equation (4.4) has to be chosen such to fulfil $\mathrm{Re}(Z) \geq 0$, as already explained in chapter 2. Solving equation (4.5) for the refractive index gives:

$$\mathrm{Im}(n) = \pm \mathrm{Im}\left[\frac{1}{kd}\cos^{-1}\left(\frac{1 - r^2 + Z_c t^2}{t\left(1 + Z_c + r(Z_c - 1)\right)}\right)\right], \tag{4.6}$$

$$\mathrm{Re}(n) = \pm \mathrm{Re}\left[\frac{1}{kd}\cos^{-1}\left(\frac{1 - r^2 + Z_c t^2}{t\left(1 + Z_c + r(Z_c - 1)\right)}\right)\right] + \frac{2\pi m}{kd}. \tag{4.7}$$

Equation (4.6) can be solved unambiguously by applying the condition $\mathrm{Im}(n) \geq 0$ for passive media. However, the solution of equation (4.7) is ambiguous. Thus, we have to apply some physically reasonable assumptions. For the case of $\omega \to 0$, we get $m = 0$ and the algebraic sign is set to $+$. For physical reasons, ε and μ or n^2 and Z^2 have to be analytical function of the frequency, respectively [75]. Thus, following the curve progression of $\mathrm{Re}(n)$ with increasing ω, one can identify the correct branch m in equation (4.7).

A dedicated Matlab program works in this fashion. First, the program calculates the additional phase which results from the half-spaces of vacuum and the substrate in MWS. For the thickness d of the metamaterial layer, always the physical thickness of the layer is chosen. Then, many branches of equations (4.7) are calculated for the refractive index and the two possible solutions for the impedance. The correct solution of Z can be determined quite simply because only one solutions fulfills $\mathrm{Re}(Z) \geq 0$. For the correct calculation of n the procedure was explained above. From these results, one can derive the permittivity and the permeability. In order to verify our results, all significant quantities are plotted in graphs by the program. Thus, errors due to the wrong choice of the branch can be easily identified and, in case, subsequently corrected manually.

This procedure provides insights into the physics of our (experimentally) studied structures. Furthermore, the structures can be optimized for specific properties such as a strong magnetic resonance.

Chapter 5

From split-ring resonators to double-negative metamaterials

In nature, one cannot find materials with a permeability unequal to unity at optical frequencies. However, using artificial structures it is possible to obtain a magnetic response at optical frequencies. These artificial elements form the basis for metamaterials. The route from simple split-ring resonators *via* cut-wire pairs to double-negative metamaterials is described in the following sections.

5.1 Split-ring resonators

In magnetostatics it is well-known, that a magnetic dipole moment is generated by a circulating current in a coil with an inductance L. The magnetic dipole moment is given by the product of the area of the coil and the current and is orientated perpendicular to the plane of the coil. Adding a capacitance C to the coil, a LC oscillatory circuit [a schematic illustration is given in Fig. 5.1(a)] with resonance frequency ω_{LC} is obtained. At ω_{LC} one expects a resonantly enhanced current flow and hence a resonantly enhanced magnetic dipole moment. Figure 5.1(b) exemplarily depicts a LC oscillatory circuit which has been reduced to the limit: It consists of a wire which has been bent to form a coil with only one winding. The ends of the wire form the capacitor. This structure is called split-ring resonator (SRR).

The resonance frequency ω_{LC} of such an oscillatory circuit can be roughly estimated making several approximations: We assume that the capacitance can be characterized by the standard formula of a plate capacitor with closely arranged plates ($C \propto$ area/distance) and the inductance by the formula of a "very long" coil with only one winding ($L \propto$ area/length) Thus, taking the nomenclature of Fig. 5.1(b), the capacitance is given by:

$$C = \varepsilon_0 \varepsilon_s \frac{wt}{d} \tag{5.1}$$

with ε_s the relative dielectric constant of the material between the plates. The inductance is obtained from:

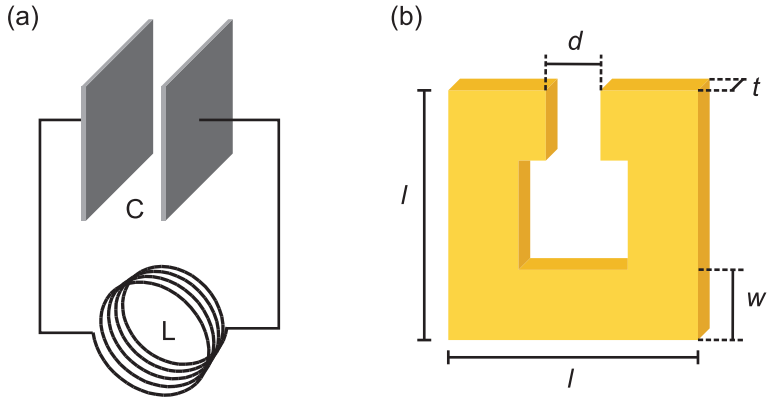

Figure 5.1: (a) A LC oscillatory circuit consisting of a coil of inductance L and a capacitor of capacitance C is schematically sketched. (b) One possible realization is reduced to its minimum requirements. This oscillatory circuit has merely one winding and the ends of the coil form the capacitor.

$$L = \mu_0 \frac{l^2}{t}. \tag{5.2}$$

This leads to the LC resonance frequency

$$\omega_{LC} = \frac{1}{\sqrt{LC}} = \frac{1}{l} \frac{c_0}{\sqrt{\varepsilon_s}} \sqrt{\frac{d}{w}} \tag{5.3}$$

and the LC resonance wavelength

$$\lambda_{LC} = \frac{2\pi c_0}{\omega_{LC}} = l\, 2\pi \sqrt{LC} \sqrt{\frac{w}{d}}. \tag{5.4}$$

Despite the many simplifying assumptions, one obtains a very good estimate [42] for the resonance frequency and resonance wavelength. Furthermore, we see that the resonance wavelength is proportional to the linear size l of the coil, if the ratio w/d is assumed to be fixed. For the values $\varepsilon_s \geq 1$ and $w \approx d$, we find the resonance wavelength to be approximately given by:

$$\lambda_{LC} \approx 10 \cdot l. \tag{5.5}$$

This shows that the dimensions of these structures are much smaller than the resonance wavelength. Thus, many SRRs can be densely packed in a periodic lattice with a lattice constant much smaller than the resonance wavelength. As a result, an incident electromagnetic wave averages over many of such structures, offering the possibility to introduce an effective response in terms of the permeability. After a simple calculation, one can derive an equation for the effective permeability [42]:

$$\mu(\omega) = 1 + \frac{F\omega^2}{\omega_{LC}^2 - \omega^2 - \mathrm{i}\gamma\omega}. \tag{5.6}$$

F represents the volume filling factor. $F = 1$, for instance, indicates that nearest neighbors already touch each other. This formula apart from the factor ω^2 in the numerator corresponds

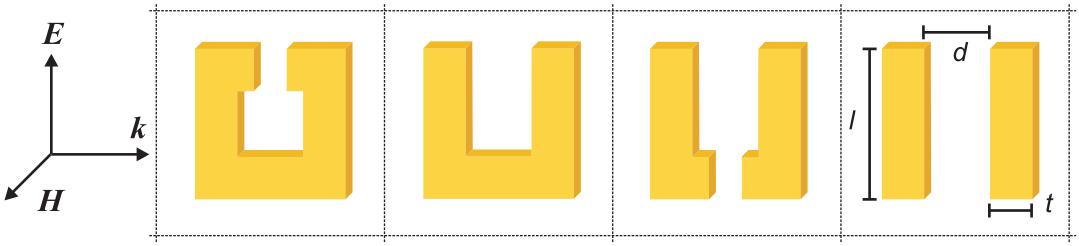

Figure 5.2: Adiabatic transition from SRR (left) to the double-wire structure (right). The polarization at which a magnetic coupling to the resonance occurs, is depicted on the left.

to the Lorentz oscillator formula for the permittivity. Near the resonance frequencies both graphs are almost identical, while the asymptotics differ.

5.2 Cut-wire pairs

The general goal is to extend the experimentally accessible spectral region of the magnetic response to telecommunication frequencies or even to the visible. However, miniaturizing the SRR is technically hardly feasible, since the structures have to be fabricated with an accuracy of 50 nm and less. Furthermore, the magnetic response of SRRs saturates at 900 nm if gold is used [76]. An alternative metamaterial design is the double-wire or the cut-wire pair. Theoretical studies of these structures [34–36] show that a negative refractive index is even feasible without any additional components. This finding is confirmed experimentally in [77]. However, this structure suffers from high losses if a negative refractive index is obtained. The reason is that both an electric and a magnetic resonance have to overlap in some frequency interval. Yet in this case either the permeability or the permittivity gets negative while the other function is positive. Therefore. the refractive index can only become negative due to the large imaginary parts of the respective functions (as discussed in chapter 2). However, this results in an imaginary part of the refractive index which is almost ten times larger than the corresponding real part [77] which is of course not favorable. For this reason, this metamaterial is merely used in the following to obtain a negative permeability. The physics of the cut-wire pairs can be understood in two different ways.

Modification of SRR

Figure 5.2 depicts schematically the transition from a SRR to a double-wire structure. The resonance frequency is given by $\omega_{LC} = 1/\sqrt{LC}$. Opening the upper slit completely, the capacitance is reduced and thus the resonance frequency increased. Additionally opening another slit in the bottom arm of the remaining “U”-shaped structure, the capacitance is reduced further. Removing the lower arms completely, one ends up at double-wires of reduced capacitance and hence increased resonance frequency, without decreasing the total dimensions of the structure itself. In this process, the ohmic current in the lower horizontal arm of the SRR is substituted by the displacement current in the case of the double-wires. While the ratio of resonance wavelength to lattice constant is $\lambda/a \approx 10$ for the SRR, the ratio is

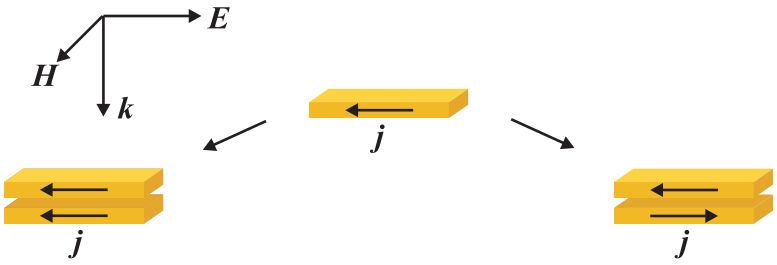

Figure 5.3: If an electromagnetic wave of the depicted polarization impinges on a wire, an antenna resonance with electric response is excited. Adding another wire, two modes appear analogously to two coupled oscillators in mechanics. The anti-symmetric mode (right) exhibits a magnetic dipole, while the symmetric mode (left) corresponds to an electric resonance only.

reduced to about $\lambda/a \approx 3$ in the case of double-wires. Although this ratio is close to two, we will see that such a medium can be still described in terms of a metamaterial.

Two coupled oscillators

Now a short wire with length l is considered as a starting point. For a perfect conductor this wire acts as an antenna with resonance wavelength $\lambda = m \cdot l/2$ ($m = 1, 2, \ldots$), i.e., an electrically resonant behavior is generated. For optical frequencies, however, the resonance wavelength shifts as explained for metallic nanoparticles previously. If another wire is added to the first one, a system of two coupled oscillators is obtained exhibiting two new eigenmodes: the anti-symmetric mode with both oscillators oscillating in opposite phase and the symmetric mode with both oscillators oscillating in phase (cf. Fig. 5.3). The symmetric mode does not exhibit a magnetic dipole moment, while the anti-symmetric mode does. Thus, due to the anti-symmetric mode one can obtain a magnetic response.

Yet, this strict separation of symmetric and anti-symmetric mode is removed by the presence of a substrate. Furthermore, the geometry of excitation causes the first wire to be excited before the second. For these reasons, the two modes will not be purely symmetric or anti-symmetric but will also comprise a portion of the opposite symmetry.

5.2.1 Experimental results

The cut-wire pairs are a fundamental building block of the negative-index metamaterial presented in this thesis. Therefore, we discuss experimental results of the cut-wire pairs in detail. Arrays of cut-wire pairs were fabricated with the methods described in chapter 4 and consist of one layer of gold (Au), followed by magnesium fluoride (MgF_2) and again gold. A schematic sketch of a cut-wire pair and the relevant parameters are shown in Fig. 5.4. We have used magnesium fluoride for our structures, because of its small permittivity $\varepsilon = 1.90$. If one takes a different dielectric with a larger permittivity, one would need a thicker layer to maintain the same capacitance. However, thicker layers are more difficult to fabricate by electron beam lithography.

Figure 5.5 shows experimental spectra of different samples measured for different polar-

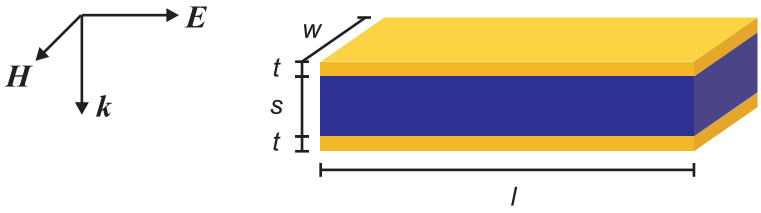

Figure 5.4: Scheme of cut-wire pairs found in Fig. 5.5(a) consisting of gold (yellow) and magnesium fluoride (blue).

izations of the incident light [78]. In the left column, the electric field is oriented parallel to the long axis of the wires (vertical polarization), while in the right column the electric field is orthogonal to the long axis (horizontal polarization). The lattice constants $a_x = 500\,\text{nm}$ and $a_y = 1050\,\text{nm}$ are kept fixed for all samples. Sample parameters are given in the caption of Fig. 5.5. For each case depicted in the left column, one can reveal two distinct dips in transmittance and two maxima in reflectance, respectively. As expected from the antenna picture, one can clearly observe, that the resonances shift to shorter wavelengths with reducing the length of the wires (reducing l). In order to check, if both resonances are actually caused by coupling effects of the two wires, another sample identical to (a) was fabricated yet without the uppermost gold wire. The corresponding transmittance and reflectance spectra [dashed curve in (a)] reveal just one single resonance, which is based on the antenna resonance of the single wire. Furthermore, the resonance wavelength of the single wire lays between the two resonances of the cut-wire pair.

In horizontal polarization one can observe two differently pronounced resonances for the double-wires. In this configuration resonances are excited along the short axis of the wire-pair. Besides, the measurements show that the dip of the resonance becomes less pronounced from (a) to (c), which can be explained due to the decreasing filling fraction.

In (d) a sample identical to (b) except reducing the distance between the wires from $s = 80\,\text{nm}$ to $s = 60\,\text{nm}$ is illustrated. Due to the reduced distance the coupling between the pairs is enhanced, causing an increase of the splitting of the two resonances. This is confirmed by comparing the spectra of (b) and (d).

The measured spectra are reproduced by numerical calculations [79]. With the aid of the corresponding field distributions at the resonances, the symmetric and the anti-symmetric mode are identified. At the short wavelength resonance currents with equal phase are excited in the two wires. For the resonance at longer wavelength the currents are out of phase. Furthermore, from the numerical calculations we can retrieve the permittivity and the permeability. The short wavelength resonance is the result of a resonance in the permittivity while the long wavelength resonance is caused by a resonance in the permeability Note, that the permeability even becomes negative. However, since the permittivity is positive, the refractive index remains positive in the entire spectral region.

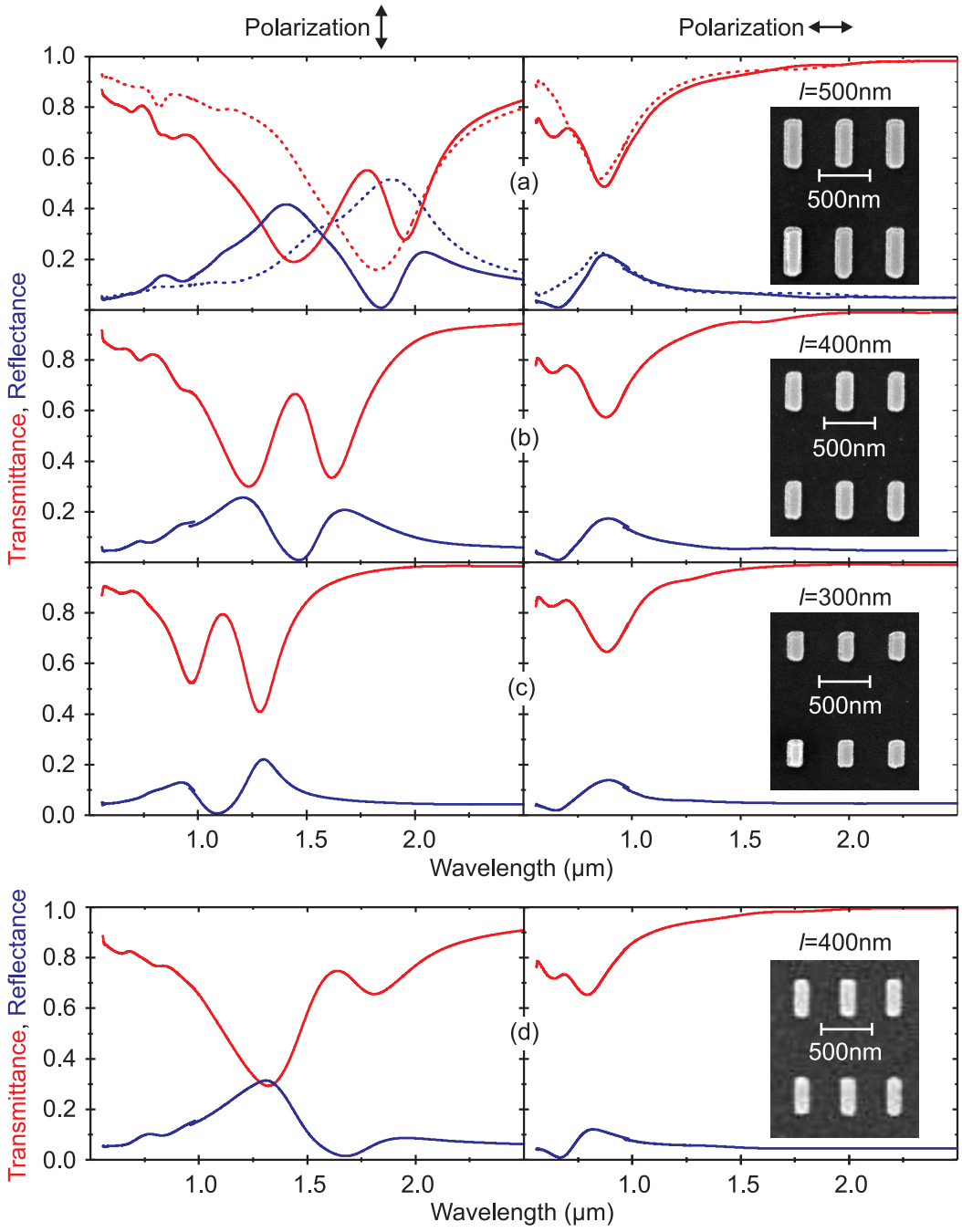

Figure 5.5: Measured transmittance (red) and reflectance spectra (blue) of double-wire structures for vertical (left column) and horizontal (right column) polarization. l = (a) 500 nm, (b) 400 nm, (c) 300 nm. Fixed parameters in (a)-(c): $w = 150$ nm, $t = 20$ nm, $s = 80$ nm, $a_x = 500$ nm and $a_y = 1050$ nm. The dashed curve in (a) is measured for a nominally identical sample, yet with the uppermost gold layer missing. (d) corresponds to (b) but with $s = 60$ nm instead of $s = 80$ nm. The inset shows SEM images of the according structures in top view.

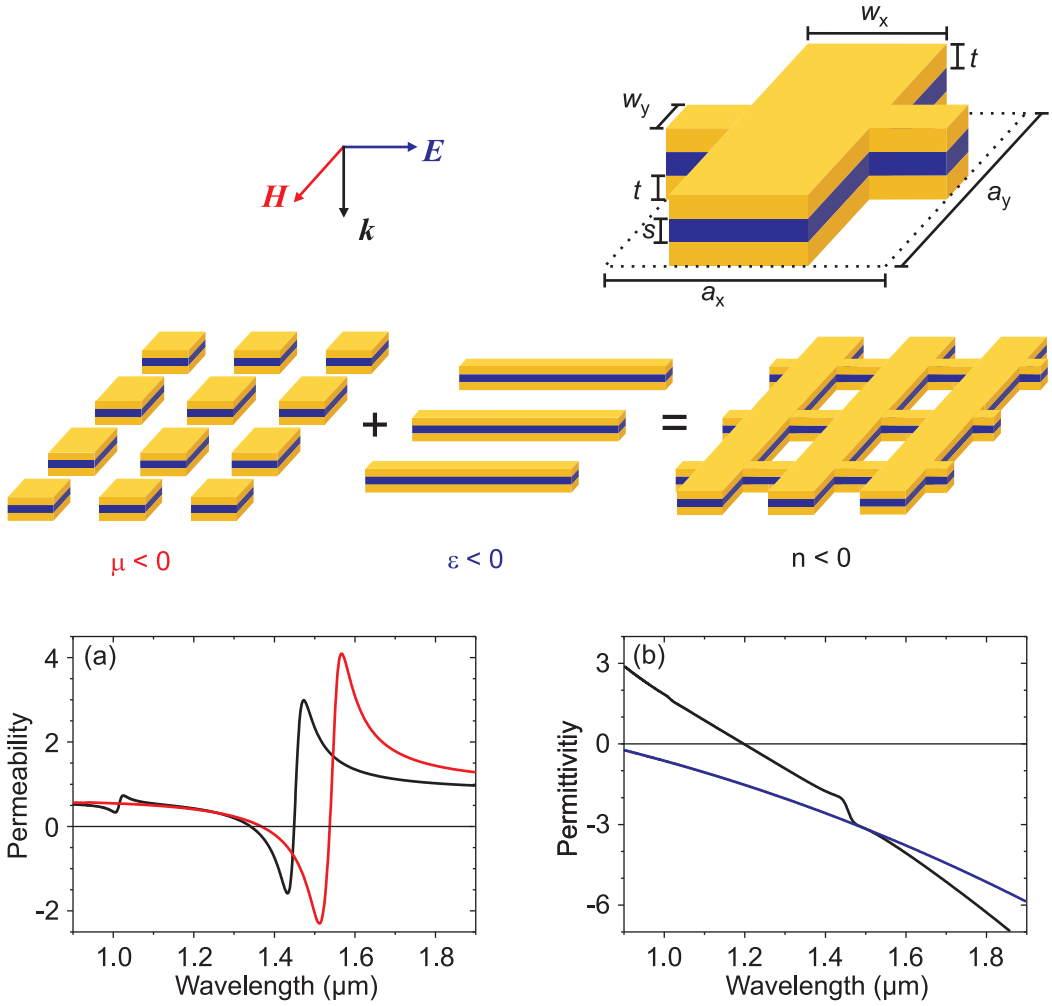

Figure 5.6: By combining the cut-wire pairs as magnetic atoms and long wires as electric atoms one obtains the double-fishnet structure. Using this structure a negative refractive index can be realized. The graphs show the magnetic response (a) of the independent cut-wire pairs (red) and the double-fishnet structure (black) and the electric response (b) of the single long wires (blue) and the double-fishnet structure (black).

5.3 Double-fishnet design

As we have already discussed, one can obtain a negative refractive index with either a negative permeability or a negative permittivity due to the large imaginary parts. However, the losses become very high in these cases [77]. Since we would like to determine the quality of a negative refractive index sample, it is useful to consider the so-called figure of merit (FOM):

$$\mathrm{FOM} = -\frac{\mathrm{Re}(n)}{\mathrm{Im}(n)} \tag{5.7}$$

For the cut-wire pairs [77] showing a negative refractive index a $\mathrm{FOM} \approx 0.1$ around 1.5 µm wavelength was realized. In order to obtain a larger FOM both the permeability and the permittivity are to be negative in the same spectral region. Structures exhibiting

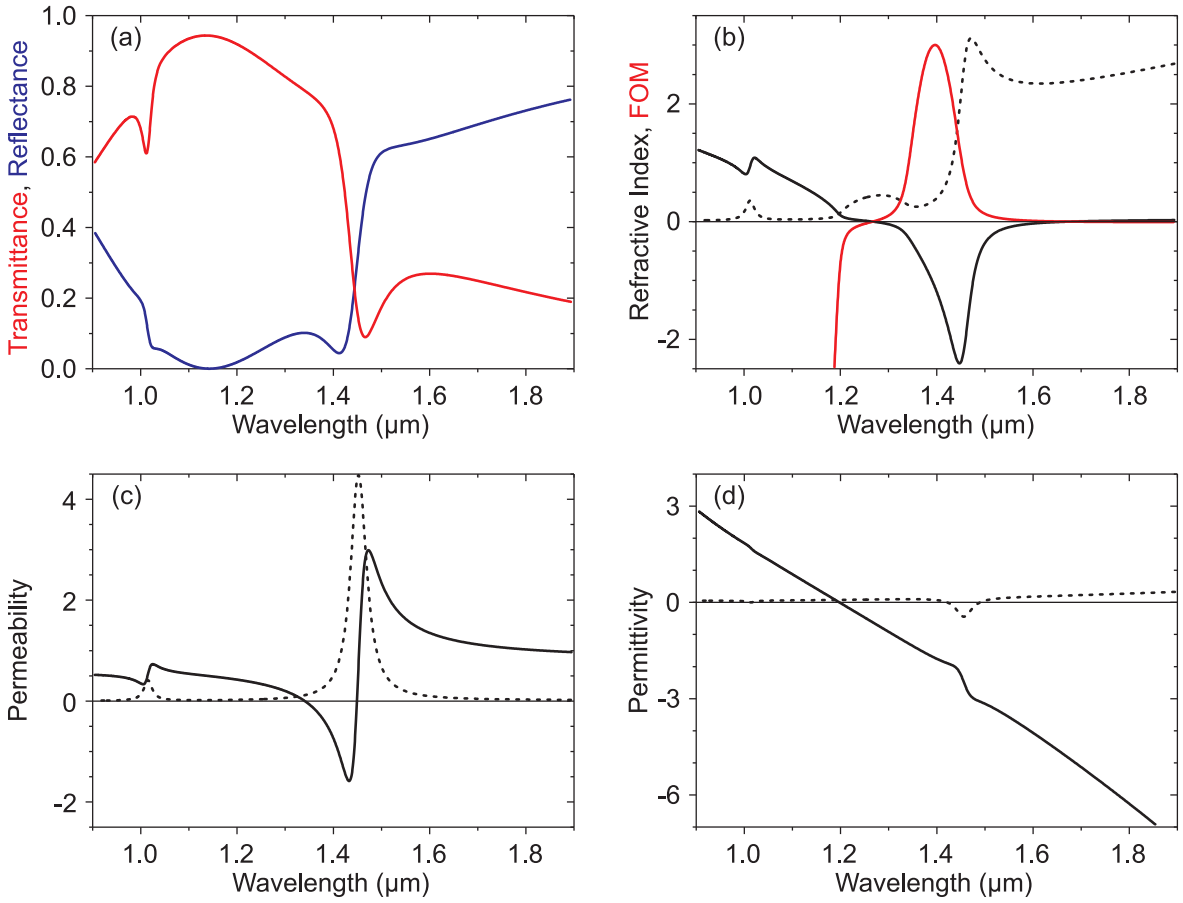

Figure 5.7: (a) Transmittance (red) and reflectance (blue). (b) Retrieved refractive index (black) and the resulting FOM (red), (c) retrieved permeability, and (d) retrieved permittivity. Solid black curves correspond to the real part, dashed black curves correspond to the imaginary part of the respective function.

a negative permittivity and a negative permeability simultaneously are also called double-negative metamaterials indicating lower losses. A combination of cut-wire pairs as magnetic atoms and long wires as electric atoms can fulfil the requirements for a double-negative metamaterial. The following structure was theoretically proposed first by Zhang *et al.* [38]. The cut-wire pairs serve as a starting point. In the spacing inbetween we add long wires. Note, that the electric field must be orientated parallel to these long wires. In order to ease fabrication, we elongate the cut-wire pairs up to the point that they touch the long wires. Furthermore, this strengthens the magnetic response, as the filling fraction of the magnetic atoms is increased. The resulting structure is schematically depicted in Fig. 5.6 and it is called double-fishnet structure due to its appearance.

The question arises, if the combination of the different elements in such a simple way leads to a negative refractive index, since the interaction might lead to a different behavior of the magnetic and the electric atoms. For this reason, we have performed simulations of each structure, namely the cut-wire pairs, long wires and the final double-fishnet structure and retrieved the permittivity and permeability of each structure. For the plasma frequency

ω_{pl} and damping or collision frequency $\gamma = \omega_{\mathrm{col}}$ of the silver metal layer we have assumed the following values (see following chapter): $\omega_{\mathrm{pl}} = 1.37 \cdot 10^{16}\,1/\mathrm{s}$ and $\gamma = 8.5 \cdot 10^{13}\,1/\mathrm{s}$. Compared to the single cut-wire pairs (red), the magnetic resonance of the double-fishnet structure (black) is slightly shifted to shorter wavelengths [cf. Fig. 5.6(a)]. Furthermore, the resonance is less pronounced in the case of the double-fishnet structure. In Fig. 5.6(b) one can see, that the long wires (blue) act as a diluted metal. The plasma frequency is much smaller than that of a homogeneous metal. The double-fishnet structure shows a similar Drude behavior as the long wires alone.

In the following, we study the double-fishnet structure in more detail. For simplicity we neglect the substrate. The findings can subsequently be transferred to simulations which include a glass substrate as well. Figure 5.7 depicts the simulated spectra of a double-fishnet structure and the results of the retrievals. On the long wavelengths side the transmittance and reflectance behave like a diluted Drude metal. Around 1.5 µm wavelength the transmittance and reflectance drop. While the reflectance remains at low values for shorter wavelengths, the transmittance increases to values of more than 90% until a second resonance appears at around 1 µm wavelength. The long wavelength resonance at $\lambda = 1.5$ µm is caused by a strong magnetic resonance combined with a negative permeability, while the short wavelength resonance exhibits only a weak magnetic response [see Fig. 5.7(c)]. The permittivity behaves similar to a Drude metal. However, at the long wavelength resonance the imaginary part gets negative. Yet, this does not violate the energy conservation law, as the imaginary part merely defines the phase relation between electric field and dielectric displacement. The important requirement is that the imaginary part of the refractive index is positive in the entire spectral region, which is indeed fulfilled. Further on, one can also clearly observe that the real part of the refractive index gets negative at the spectral position of the long wavelength resonance at 1.5 µm wavelength. If moreover both the permeability and the permittivity are negative, the imaginary part of the refractive index drops to small values. This is also apparent in the FOM, which shows its maximum value at 1.4 µm wavelength. Furthermore, the transmittance increase to values of more than 60%. However, if both the permeability and the permittivity are positive the refractive index becomes positive as well. Around 1.1 µm most light is transmitted and virtually no light reflected. At this spectral position both the permeability and the permittivity are approximately unity, i.e., the impedance of the material matches approximately the impedance of the vacuum.

Now. we study the influence of different structural parameters. The corresponding effective material parameters are summarized in Figs. 5.8 and 5.9.

We start with varying the length w_x of the magnetic atoms, i.e., we vary the length of the cut-wire pairs. Hence, we expect the magnetic resonance to shift to longer wavelength as the length of the antenna increases. One can clearly observe a shift of the magnetic resonance to longer wavelengths with increasing length of the magnetic atoms. Furthermore, the magnetic response becomes stronger. Simultaneously, the plasma frequency decreases slightly to shorter frequencies. Due to the increased absolute value of the negative real parts of both the permeability and permittivity, the real part of the refractive index gets more negative as well. However, the FOM does not increase as strongly, as the imaginary parts of the permittivity and permeability are also enhanced.

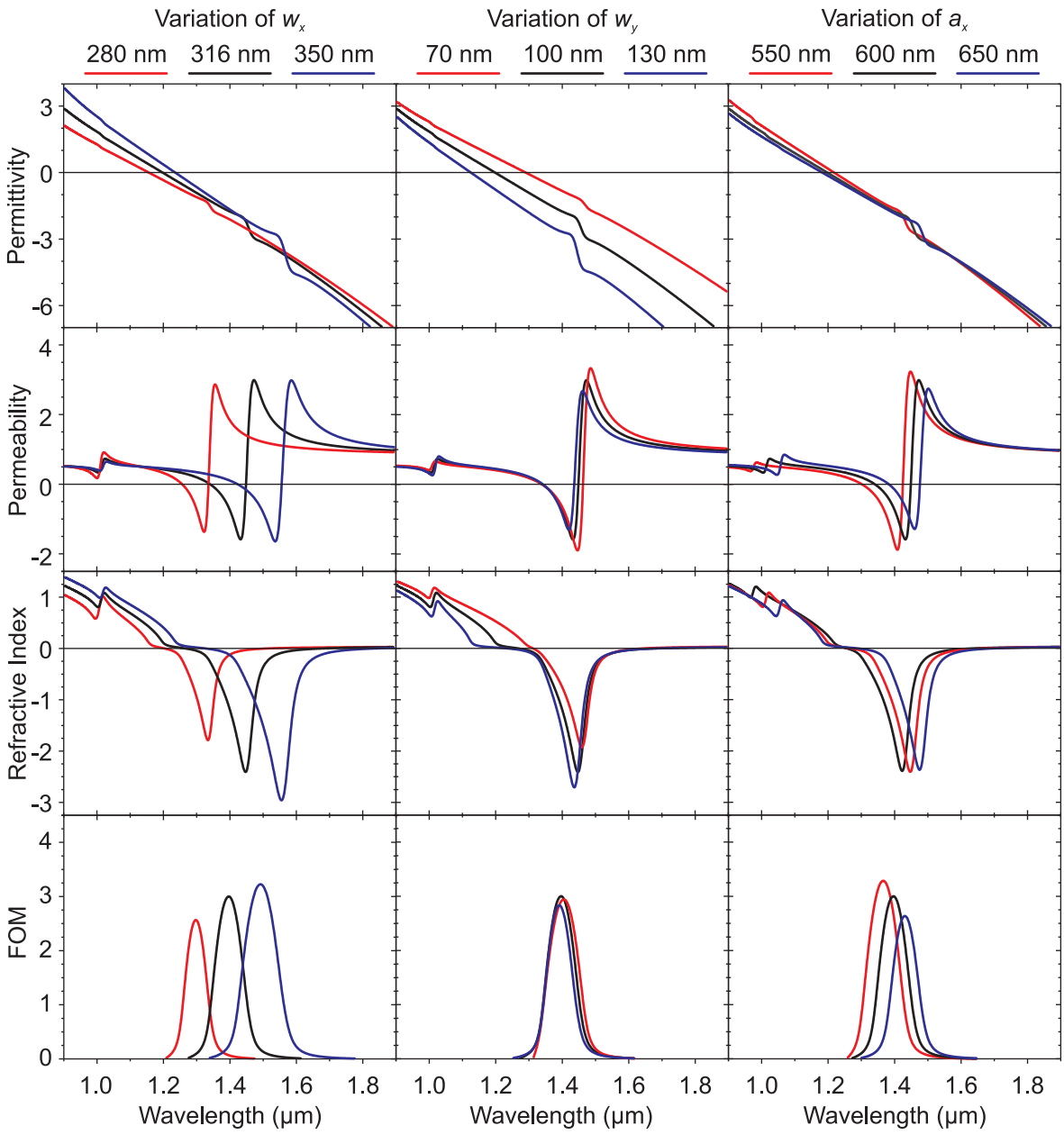

Figure 5.8: Variations of different parameters of the double-fishnet structure: w_x (left column), w_y (middle column), and a_x (right column). The real part of the permittivity (first row), the real part of the permeability (second row), the real part of the refractive index (third row), and the resulting FOM (last row) are depicted. The black curves correspond to the structure shown in Fig. 5.7.

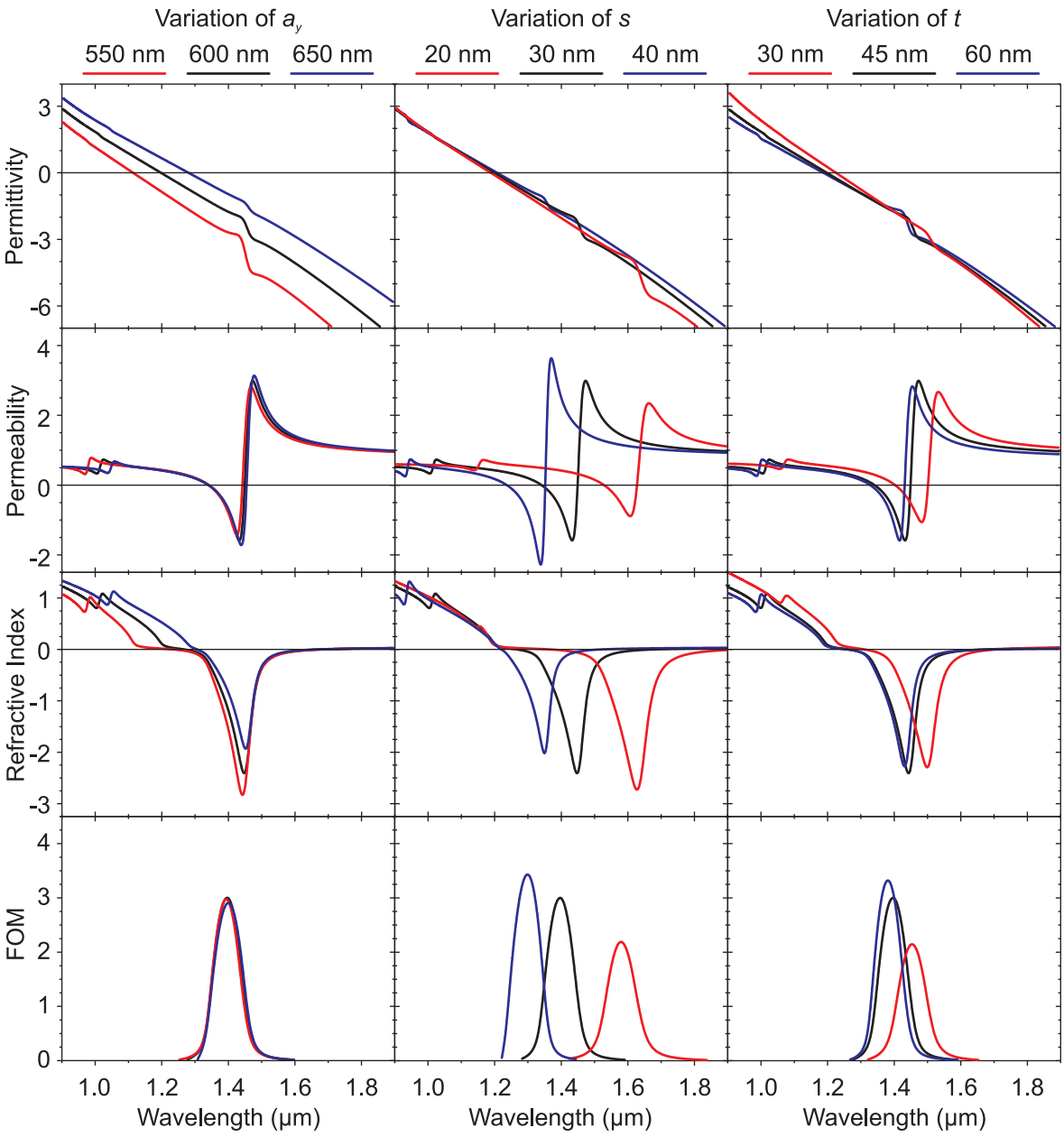

Figure 5.9: Variations of different parameters of the double-fishnet structure: a_y (left column), s (middle column), and t (right column). The real part of the permittivity (first row), the real part of the permeability (second row), the real part of the refractive index (third row), and the resulting FOM (last row) are depicted. The black curves correspond to the structure shown in Fig. 5.7.

Broadening the thin wires w_y leads to a larger filling fraction of the metal which acts like a diluted Drude metal. Hence, the plasma frequency shifts to higher frequencies or shorter wavelengths, respectively. Due to the increasing width of the wires, the strength of the magnetic resonance decreases, since the effective density of the magnetic atoms is reduced. In the depicted example, the influence of the wire width has only a minor effect on the refractive index and the FOM, since the plasma frequency is already in the vicinity of the magnetic resonance.

The filling fraction of the metal belonging to the building block of the long wires is approximately given by w_y/a_y. Varying the lattice constant a_x has virtually no effect on the plasma frequency. However, if we vary the lattice constant a_y a clear influence on the plasma frequency is visible. For the magnetic atoms the filling fraction is approximately given by w_x/a_x. Increasing the lattice constant a_x, the strength of the magnetic response decreases accordingly. Yet, varying the lattice constant a_y has hardly any influence on the magnetic response.

Apart from the lateral structural parameters one can also vary the thickness of the magnesium fluoride layer or the thickness of the metal layers. If we vary these parameters, we observe hardly any alteration in the permittivity. Reducing the distance between the metal plates, i.e. varying s, enhances the coupling. This leads to a shift of the magnetic resonance to longer wavelengths and in addition enhances the splitting of the two magnetic resonances. Thus, the magnetic resonance is very sensitive to variations of the spacer on the nanometer scale. The thickness of the metal layers t has less effect on the magnetic resonance. Only when the thickness reaches the skin depth, the effects take on greater significance.

5.3.1 Influence of the hole shape

A recent detailed study has reported that the hole shape is not important at all [80] by comparing three particular gold-based samples with identical lattice constants and identical thicknesses. We investigate this aspect in a systematic theoretical study employing three different hole shapes: rectangular holes (as discussed above), square-shaped holes, and circular holes. We use a quadratic lattice, i.e. $a_x = a_y = a$, for all three hole shapes. For a fixed thickness we have merely three free parameters for the rectangular holes: w_x, w_y, and the lattice constant a. In essence, the problem with circular holes is that one has just two rather than three free parameters, namely the hole radius r and the lattice constant a. The same holds for square-shaped holes. It would be purely coincidental if this reduced number of degrees of freedom delivered identical results. If, on the other hand, one acquires additional freedom by varying at least one further parameter, such as, e.g., the dielectric spacer thickness s, one again has three free parameters and it appears possible in principle to achieve comparable performance with circular holes or square-shaped holes than with rectangular holes. However, these structures suffer from different problems to be discussed below.

To validate this qualitative overall reasoning, we proceed in two steps. (A) First, we fix the spacer thickness – as in reference [80] – and explicitly invalidate the general claim of reference [80] by example. (B) Second, we vary the spacer thickness at the same time.

For the Drude model we use the plasma frequency $\omega_{\mathrm{pl}} = 1.37 \cdot 10^{16}\,\mathrm{s}^{-1}$ and damping

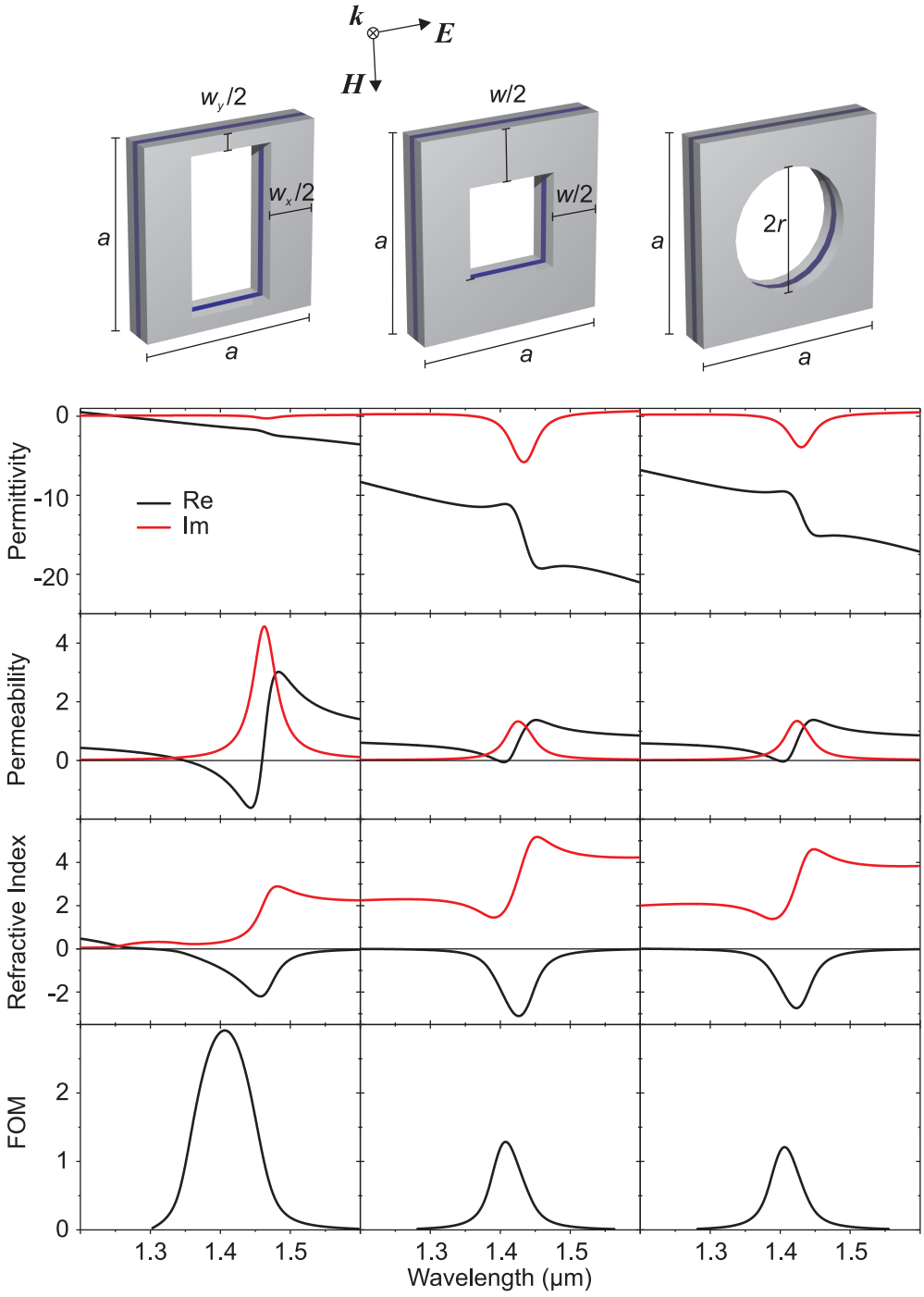

Figure 5.10: Comparison of rectangular, square, and circular-shaped holes in double-fishnet structures. The three columns represent the three hole shapes, which are indicated on the top. The polarization configuration is also shown on the top. The rows below show the real and imaginary parts of the retrieved effective electric permittivity ε, the magnetic permeability μ, the refractive index n, and the resulting $\mathrm{FOM} = -\mathrm{Re}(n)/\mathrm{Im}(n)$. The parameters for rectangular holes are $w_x = 316\,\mathrm{nm}$, $w_y = 100\,\mathrm{nm}$, and $a = 600\,\mathrm{nm}$. The best parameters that we have found here for square-shaped holes are $w_x = w_y = w = 319\,\mathrm{nm}$ and $a = 625\,\mathrm{nm}$; for circular holes $r = 192\,\mathrm{nm}$ and $a = 625\,\mathrm{nm}$. The vertical layer thicknesses are kept fixed for all three hole shapes: $45\,\mathrm{nm}$ Ag (gray), $30\,\mathrm{nm}$ MgF_2 (blue), and $45\,\mathrm{nm}$ Ag (gray).

$\gamma = 8.5 \cdot 10^{13}\,\mathrm{s}^{-1}$ for silver. The $\mathrm{MgF_2}$ refractive index is taken as $n = 1.38$. In our calculations, we embed the double-fishnet structure in an effective homogeneous medium with a refractive index of $n = \sqrt{1.1}$, whereas the structures are usually located on a glass substrate in experiments. This simplification is unproblematic unless Wood anomalies (see chapter 2.3.3) arising from diffraction of light into the substrate spectrally merge with the metamaterial resonances. Obviously, one is leaving the effective-medium limit in this case, which implies that a description in terms of effective material parameters becomes meaningless. This aspect will become relevant in step (B) below but is unimportant for step (A).

(A) We start from the vertical layer thicknesses Ag ($t = 45\,\mathrm{nm}$), $\mathrm{MgF_2}$ ($s = 30\,\mathrm{nm}$), and Ag ($t = 45\,\mathrm{nm}$) that have been used for a low-loss metamaterial (see following chapter). Lateral parameters are $w_x = 316\,\mathrm{nm}$, $w_y = 100\,\mathrm{nm}$, and $a = 600\,\mathrm{nm}$. The resulting $\mathrm{FOM} \approx 3$ is the best experimentally verified value available at present (see Fig. 5.10). We emphasize that this is not even the best theoretically possible set of parameters for rectangular holes. For example, for $t = 45\,\mathrm{nm}$, $s = 30\,\mathrm{nm}$, $w_x = 351\,\mathrm{nm}$, $w_y = 100\,\mathrm{nm}$, and $a = 500\,\mathrm{nm}$ we find a $\mathrm{FOM} = 3.72$ at around 1.4 µm wavelength.

To find the best theoretically possible values for square-shaped holes, we proceed as follows. We simultaneously vary a and $w = w_x = w_y$ and keep the operation wavelength fixed at 1.4 µm and search for an optimum of the FOM at this wavelength. For circular holes, we proceed analogously by varying a and r. The results of these optimizations are depicted in Fig. 5.10, revealing an optimum FOM of 1.29 and 1.21 for square-shaped and circular holes, respectively. While the resulting FOM for square-shaped and circular holes are quite similar, they both differ by about a factor of 2.5 from the FOM for the rectangular-hole case. The larger losses for the square/circular holes mainly originate from a deteriorated magnetic resonance that barely exhibits a negative real part of the magnetic permeability above resonance. This means that these samples are not really double negative. The real part of the electric permittivity of the square/circular holes is even more negative than in the rectangular-hole case due to the larger volume fraction of metal in the diluted-metal parts. This overall behavior supports our above qualitative reasoning in that one generally does not have a sufficient number of free parameters for the loss optimization in the square/circular-hole case.

(B) Next, we vary the thickness s of the dielectric $\mathrm{MgF_2}$ spacer layer. We start by continuing along the lines of (A) in that we consider a metamaterial embedded in an effective dielectric environment, i.e., we do not account for a substrate. Again, the operation wavelength is fixed to $\lambda = 1.4\,\mu\mathrm{m}$ to allow for direct comparison with the above rectangular-hole structures. The small variations of λ in table 5.1 are due to limited computation time.

As the spacer thickness s is increased from 30 nm to 100 nm in table 5.1, a and r have to be increased to keep the vacuum wavelength λ fixed. The FOM increases from 1.21 to 3.37 which seemingly outperforms the optimum rectangular holes. Even without a glass substrate, however, several parameter choices exhibit values $(\lambda/n)/a < 2$, where $n = \sqrt{1.1}$ is the refractive index of the embedding medium. Recall that the ratio $(\lambda/n)/a = 2$ corresponds to the fundamental Bragg condition. Hence, for ratios below 2, the effective-medium approximation can be questionable.

The situation becomes even worse if the glass substrate is accounted for. To further

s	a	r	λ	λ/a	$(\lambda/n)/a$	FOM
30 nm	625 nm	192 nm	1.406 µm	2.25	2.15 (1.50)	1.21 (0.99)
40 nm	670 nm	191 nm	1.407 µm	2.10	2.00 (1.40)	1.47 (1.09)
50 nm	700 nm	188 nm	1.404 µm	2.01	1.91 (1.34)	1.78 (1.35)
60 nm	735 nm	201 nm	1.406 µm	1.91	1.82 (1.28)	2.11 (1.31)
70 nm	755 nm	197 nm	1.409 µm	1.87	1.78 (1.24)	2.41 (1.48)
80 nm	780 nm	211 nm	1.409 µm	1.81	1.72 (1.20)	2.74 (1.35)
90 nm	800 nm	221 nm	1.410 µm	1.76	1.68 (1.18)	3.06 (1.15)
100 nm	820 nm	241 nm	1.405 µm	1.71	1.63 (1.14)	3.37 (0.88)

Table 5.1: FOM of circular-hole double-fishnet negative-index photonic metamaterials obtained by embedding the structure in an effective homogeneous medium with refractive index $n = \sqrt{1.1}$ (i.e., no glass substrate). The FOM values in brackets refer the corresponding calculations for structures in air ($n = 1$) on a glass substrate with refractive index $n = 1.5$. The thickness of the spacer layer increases from $s = 30\,\mathrm{nm}$ in the top to $s = 100\,\mathrm{nm}$ in the bottom row. The metal thickness $t = 45\,\mathrm{nm}$ is fixed. To keep a fixed vacuum wavelength $\lambda = 1.4\,\mu\mathrm{m}$, the lattice constant a, and the hole radius r have to be adjusted. The column labeled λ/a refers to the ratio of vacuum wavelength and lattice constant. The column to the right refers to the corresponding ratio for the material wavelength (λ/n) in the embedding medium with refractive index $n = \sqrt{1.1}$ (glass substrate with refractive index $n = 1.5$).

investigate this aspect, we have repeated the calculations for the double-fishnet structure in air located on a glass substrate. The corresponding FOM values are given in brackets in table 5.1. Obviously, they are generally lower. Moreover, the FOM first increases with increasing s but then drops again, reaching a maximum value of $\mathrm{FOM} = 1.48$ for the circular holes at $s = 70\,\mathrm{nm}$. The reason underlying this drastic influence of the substrate is the Wood anomaly corresponding to diffraction of light into the substrate (i.e., $(\lambda/n)/a = 1$ with the glass-substrate refractive index $n = 1.5$) that gradually shifts towards the magnetic resonance with increasing s, hence increasing a, and eventually overlaps with it. This overlap deteriorates the metamaterial performance, especially its FOM. Moreover, an interpretation of the results in terms of an effective material is highly questionable at this point as $1 \approx (\lambda/n)/a < 2$.

The bottom line of part (B) is that the FOM of the circular holes can only be increased slightly by varying the dielectric-spacer thickness.

In conclusion, for fixed vertical layer sequence and fixed operation wavelength, the hole shape has a large influence on the losses. Clearly, this finding does not exclude the possibility of special operation frequencies for which the hole shape accidentally has no large influence. Indeed, as the operation frequency increases towards the red end of the visible, the rectangular holes tend to become more square-shaped (see following chapter), and the difference between rectangular/square/circular holes becomes quite small because the performance is limited by the losses introduced by the constitutive metal rather than by the losses introduced by design.

Chapter 6

Experimental results

We have performed transmittance and reflectance spectroscopy on several negative-index double-fishnet metamaterials. Experiment and theory agree well. Furthermore, we have performed a series of interferometric pulse propagation experiments on negative-index double-fishnet structures. From the interference fringes with and without the sample, we have directly inferred the phase time delay. From the pulse-envelope shift, we have determined the group time delay. In a spectral region, we have found that the phase and the group velocity are negative simultaneously.

By optimizing the structure parameters and utilizing silver instead of gold, we have significantly reduced the losses of the double-fishnet metamaterial. For this sample, we retrieve a real part of the refractive index of $\mathrm{Re}(n) = -2$ around 1.5 µm wavelength. The maximum of the ratio of the real to the imaginary part of the refractive index is about three at a spectral position where $\mathrm{Re}(n) = -1$.

Further downscaling of the lattice constant has brought the negative-refractive index to the red end of the visible spectrum. By comparing transmittance, reflectance, and phase-sensitive time-of-flight experiments with theory, we infer a real part of the refractive index of $\mathrm{Re}(n) = -0.6$ at 780 nm wavelength – which is visible in the laboratory.

Measuring and calculating oblique-incidence transmittance spectra of a negative-index metamaterial allow for inferring the in-plane dispersion relation of the magnetization wave. From the geometry and the dispersion shape, we conclude that coupling is predominantly *via* magnetic dipoles for wave propagation along the magnetic-dipole direction. These magnetization waves are the classical analog of magnon excitations of quantum-mechanical spins.

Furthermore, we have also fabricated negative-index double-fishnet metamaterials with up to three functional layers. The measured performance is close to theory and in that the retrieved optical parameters do not change too much with the number of functional layers.

6.1 Simultaneous negative phase and group velocities of light

In Fig. 6.1(a) measured transmittance (solid curves) and reflectance (dashed curves) spectra of a double-fishnet structure consisting of Au/$\mathrm{MgF_2}$/Au are depicted. The corresponding calculations are shown in part (b). Experiment and theory are found to agree very well. Ad-

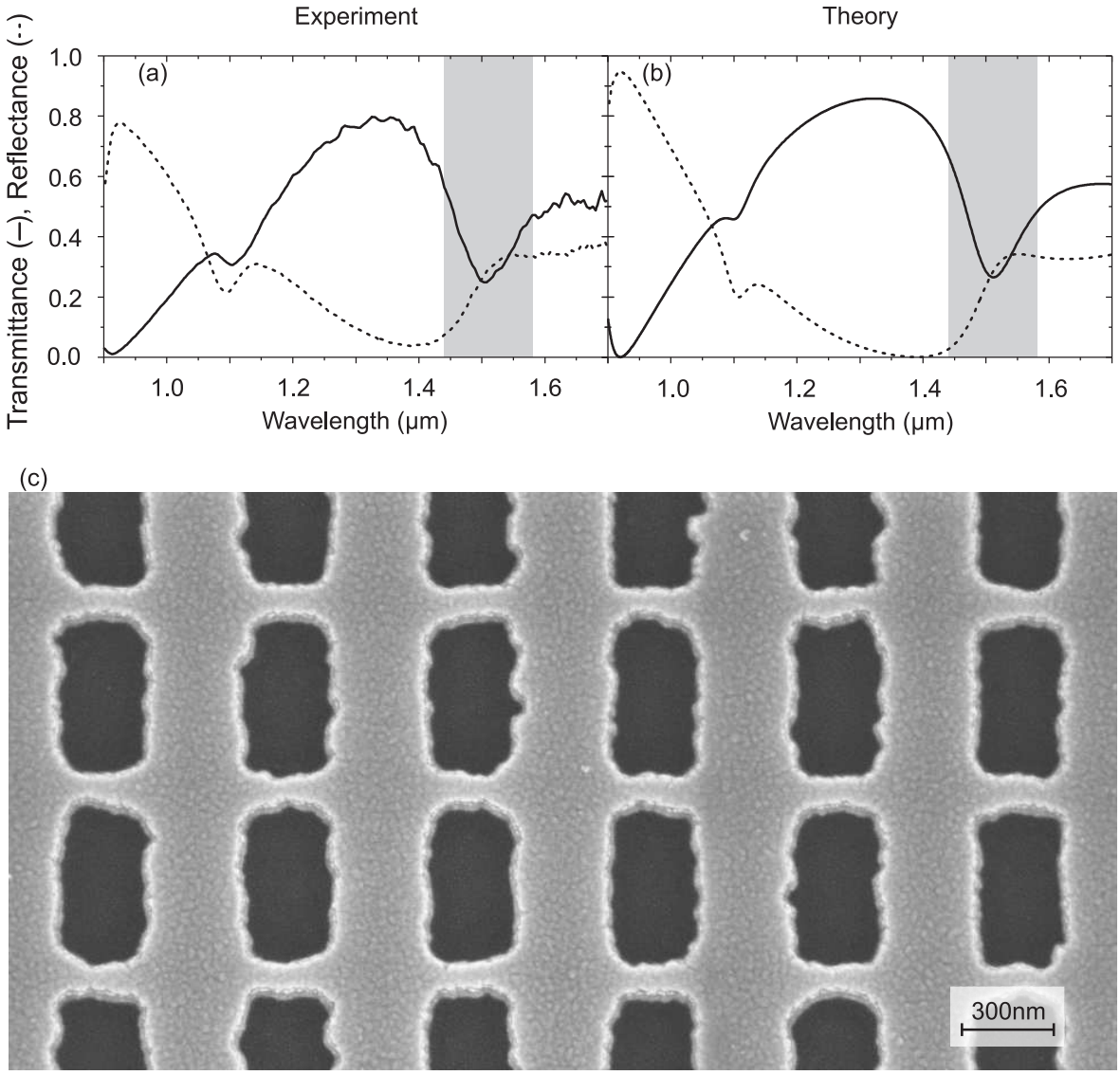

Figure 6.1: (a) Measured transmittance (solid) and measured reflectance (dashed) spectra for the electric field polarized parallel to the thin wires of a double-fishnet structure and (b) corresponding calculations are shown. To guide the eye, the total spectral region shown in Fig. 6.5 is highlighted by the grey area. (c) Top-view electron micrograph of corresponding double-fishnet structure. Parameters of the sample are: $t = 25\,\mathrm{nm}$, $s = 35\,\mathrm{nm}$, $w_x = 307\,\mathrm{nm}$, $w_y = 100\,\mathrm{nm}$, and lattice constant $a_x = a_y = a = 600\,\mathrm{nm}$. The metamaterial thickness is $d = 2t + s = 85\,\mathrm{nm}$. Gold and $\mathrm{MgF_2}$ are employed as constituent materials.

ditionally, the SEM image in Fig. 6.1(c) reveals a good quality of our double-fishnet structure employed in the experiments. The sample parameters are given in the corresponding caption. For gold we assumed a plasma frequency of $\omega_{\mathrm{pl}} = 1.32 \cdot 10^{16}\,\mathrm{s}^{-1}$ and a damping of $\gamma = 1.2 \cdot 10^{14}\ \mathrm{s}^{-1}$. These values are obtained from a fit of the Drude model to the measured complex permittivity of thin gold films [23] in the near infrared. The refractive index of the glass substrate is $n = 1.5$ and that of the $\mathrm{MgF_2}$ spacer layer is $n = 1.38$.

It is important that exactly the same set of parameters will be used later on in the theoret-

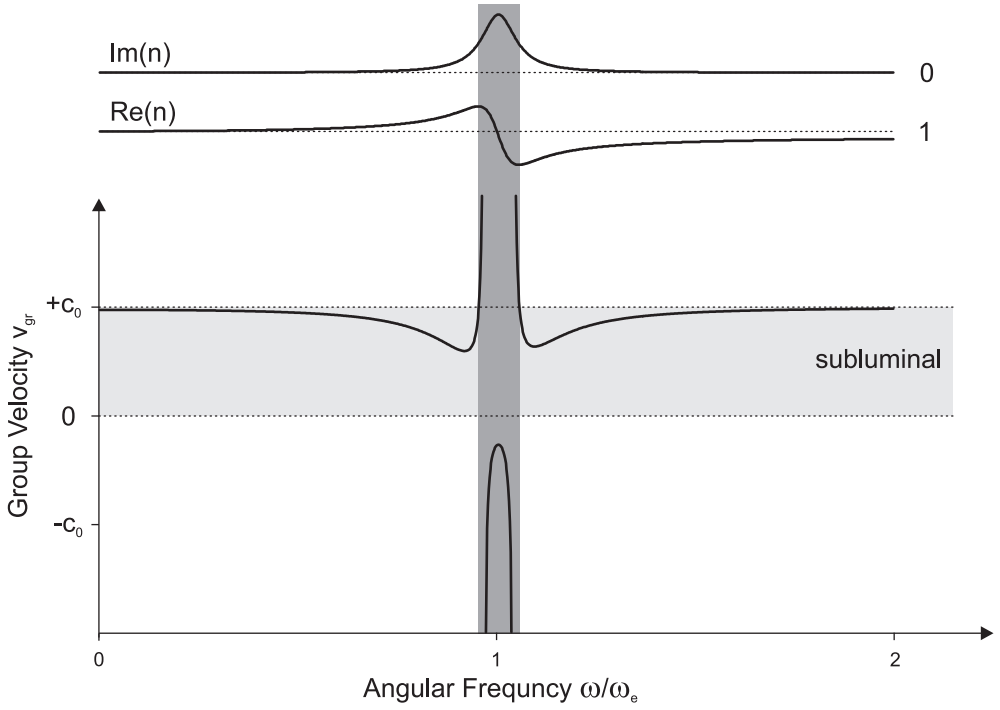

Figure 6.2: Group velocity v_{gr} of the Lorentz oscillator model. The real part and the imaginary part of the refractive index are depicted on top. $\mathrm{Re}(n)$ is always positive. The dashed lines indicate the case of $\mathrm{Im}(n) = 0$ and $\mathrm{Re}(n) = 1$, respectively. The dark gray region corresponds to anomalous dispersion. With decreasing damping $\gamma/\omega_{\mathrm{e}}$, this region shrinks in width. The parameters are: $\gamma/\omega_{\mathrm{e}} = 0.1$ and $\omega_{\mathrm{pl}}^2/{\omega_{\mathrm{e}}}^2 = 0.05$ (taken from [81]).

ical analysis of the interferometric experiments as well as in the effective parameter retrieval. Before we analyze the results of the time-resolved measurements, we study theoretically the behavior of the group velocity at a resonance.

6.1.1 Theory of negative group velocities

The group velocity describes the speed at which the envelope of a pulse propagates and is given by

$$v_{\mathrm{gr}} = \frac{d\omega}{dk} = \frac{c_0}{\mathrm{Re}(n) + \omega \frac{d\mathrm{Re}(n)}{d\omega}} = \frac{c_0}{n_{\mathrm{gr}}}. \tag{6.1}$$

Here, the group index n_{gr} is introduced analogously to the refractive index of the phase velocity and specifies the difference of the velocity of the pulse inside the medium compared to vacuum. For the fictitious case of negligible dispersion ($\frac{d\mathrm{Re}(n)}{d\omega} = 0$), the group velocity is identical to the phase velocity, i.e., the group velocity is negative if the phase velocity is negative.

For simplicity we assume $\mu = 1$. For the permittivity we assume the previously described Lorentz oscillator. This case is shown in Fig. 6.2. In the upper part the refractive index is depicted, and below, the corresponding group velocity. Despite the quite simple characteristics of the refractive index, the group velocity exhibits a rather complex behav-

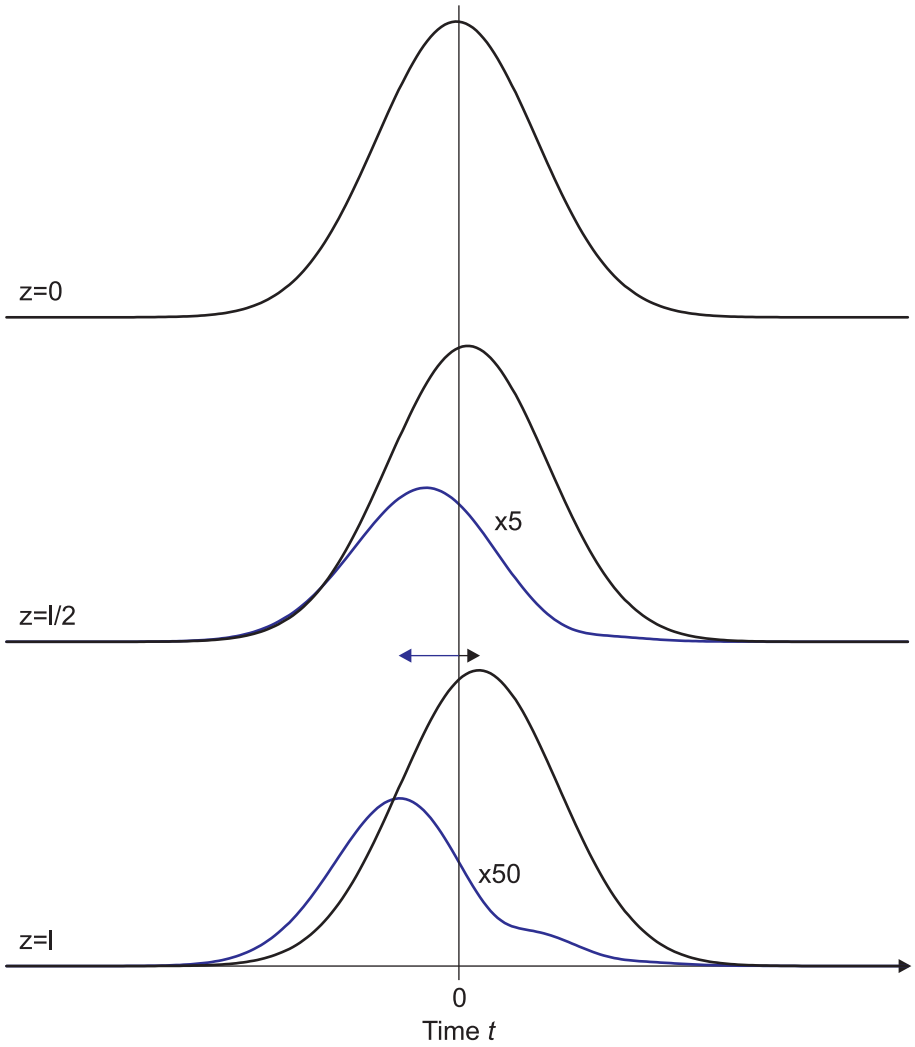

Figure 6.3: Absolute value of the electric field $|E(z,t)|$ at three different positions ($z = 0$, $z = l/2$, and $z = l$) for a gaussian pulse propagating in vacuum (black) and in a Lorentz oscillator medium under conditions of negative group velocity (blue curve). Pulse parameters are (see equation 4.1): $\omega_0/\omega_e = 1$ and $w/\omega_0 = 0.02/\sqrt{2}$. Oscillator parameters are: $\omega_{pl}^2/{\omega_e}^2 = 0.05$ and $\gamma/\omega_e = 0.1$. The medium has a thickness of $l = 20c_0/\omega_0$. For $z = l$ one can already see distortions of the Gaussian pulse shape. The blue curves are multiplied by the indicated factors to compensate for the exponential attenuation.

ior. In the spectral region around the resonance ω_e, we obtain anomalous dispersion, i.e., $\frac{d\mathrm{Re}(n)}{d\omega} < 0$. If the denominator in equation (6.1) drops below unity, v_{gr} becomes larger than the vacuum speed of light. These velocities are called superluminal group velocities. For large negative slopes even the group velocity itself becomes negative. While group velocities between $v_{gr} = 0$ and $v_{gr} = c_0$ are considered as "normal", the discovery of group velocities with $v_{gr} > c_0$ or $v_{gr} < 0$ led to many discussions. For this reason, we deal with the dark grey region of Fig. 6.2 in more detail. In this spectral region the absorption is at maximum. We consider a spectrally narrow Gaussian pulse propagating inside the medium shown in Fig. 6.2. What happens to the pulse? The result is depicted in Fig. 6.3. We look at three different positions in the material and measure how the absolute value of the electric field

depends on time at these positions. At the entry of the medium at $z = 0$ the pulse remains unaffected from the medium (we neglect reflections for simplicity). Thus, the reference pulse propagating through vacuum (black) and the pulse propagating through the medium (blue) are still identical. Now, we take a look at a position inside the medium ($z = l/2$) and compare the pulses. The reference pulse in vacuum is shifted along the time axis towards later times, since the pulse needs the time $t = z/c_0$ to propagate from the position at $z = 0$ to $z = l/2$. However, regarding the pulse which propagates inside the medium, we observe, that the maximum of the pulse is shifted to negative times. This effect is even more pronounced for the third position at $z = l$. The maximum of the pulse appears yet earlier. This means, an observer located at $z = l$ can see the maximum of the pulse before another observer sees the maximum of the pulse impinging onto the medium. If the medium had a thickness of l, it would appear as if the maximum of the transmitted pulse leaves the medium before the maximum of the incident pulse enters the medium. How can we understand this situation?

In our case, the observer at $z = l$ could hardly detect the pulse since it would have been already strongly absorbed inside the medium. Furthermore, the pulse at this position is no longer Gaussian shaped. So, the question arises, what actually happens to the pulse. Absorption occurs if the oscillators inside the medium are phase shifted by $\pi/2$ with respect to their excitation. When the maximum of a resonant pulse with $\omega_0 = \omega_\mathrm{e}$ impinges on the medium, already a big part of the leading edge has penetrated into the material. Inside the material, the oscillators are excited to perform oscillations. On a time scale identical roughly to the inverse damping rate γ the oscillators are not yet at exact $\pi/2$ phase shift. Thus, the part of the pulse which propagates inside the medium for times on the scale of $1/\gamma$, is just weakly damped. However, for later times the oscillators are already on steady state. Hence, the major part of the pulse is strongly damped. This also causes the pulse reshaping observed at $z = l$. Furthermore, the pulse maximum the observer detects at $z = l$ is located in the part of the pulse, which is least absorbed, i.e. in the leading edge.

This behavior as well as the negative group velocity are not at all in conflict with relativity or causality, essentially because the peak of the output pulse is not a cause of the peak of the input pulse. In other words, even though input and output pulse can have the same Gaussian shape, reshaping of the pulse envelope is of crucial importance [82]. Already in the past, several examples of abnormal dispersions have been discussed [83].

For the first time negative group velocity was measured on an excitonic absorption resonance in a GaP:N semiconductor sample by time resolving the transmission of a picosecond optical pulse [84]. Further experiments along these lines, e.g., on positive-index systems [85–87], have confirmed this behavior. Naturally the question arises if this effect allows for information communication faster than the speed of light. Here, the difficulty is to answer what information is. A Gaussian pulse itself cannot serve for information communication. Only a sequence of pulses (or the absence of pulses, respectively) leads to information communication. Already Sommerfeld [88] and Brillouin [89] discussed and philosophized this issue. Sommerfeld delineated that oscillators inside the medium have to be excited in first instance and thus, cannot react on the field instantaneously. In consequence, the leading edge of the pulse always propagates through the medium with the speed of light. Subsequently, Sommerfeld focused on a discontinuity or a non-analytic point in the pulse. This point ap-

pears due to switching on or off a light source and hence carries information. Therefore, information is already located well before the maximum of the entire pulse. These so-called Sommerfeld- and Brillouin precursor never exceed the speed of light. This could be confirmed experimentally, for instance in [90]. An illustrative explanation can also be found in [91].

6.1.2 Experimental data

The Michelson interferometer offers the opportunity to measure the phase delay Δt_{ph} and group delay Δt_{gr}. Figure 6.4(a) results from averaging 20 individual scans with a total acquisition time of $40\,\mathrm{s}$. For a center wavelength of the pulse of $1.5\,\mu\mathrm{m}$ we have $\Delta t_{\mathrm{ph}} = -0.62\,\mathrm{fs} < 0$ and $\Delta t_{\mathrm{gr}} = -19.1\,\mathrm{fs} < 0$. The error in determining Δt_{ph} is $0.07\,\mathrm{fs}$, the error in Δt_{gr} is $0.3\,\mathrm{fs}$. To test our apparatus, we also performed experiments on a $d = 120\,\mathrm{nm}$ thin dielectric film of HfO_2 with real refractive index $n = +1.95$ on the glass substrate, leading to positive phase delay $\Delta t_{\mathrm{ph}} = +0.79\,\mathrm{fs} > 0$ and positive group delay $\Delta t_{\mathrm{gr}} = +0.78\,\mathrm{fs} > 0$. Here, phase and group delay are identical within the measurement error and consistent with the HfO_2 refractive index.

From the delay time

$$\Delta t = \Delta t_{\mathrm{interfaces}} + \frac{2d}{v} - \frac{2d}{c_0}. \tag{6.2}$$

we can calculate the velocities. Here, v is either the phase velocity $v_{\mathrm{ph}} = c_0/\mathrm{Re}(n)$ or the group velocity v_{gr}. d corresponds to the total thickness of our sample. The factor two stems from the double-pass geometry of our Michelson interferometer. In our experiment, the pulse envelope propagates with velocity v_{gr} and the individual fringes of the pulse with velocity v_{ph} through the metamaterial, which corresponds to the second term in the equation. For reference, the pulse propagates in vacuum with speed of light c_0, giving rise to the third term. In the case of vacuum (one can easily see that) we would obtain a time delay of zero. The first term reflects the effects caused by the surface of the metamaterial. Due to the interfaces air/metamaterial/glass an additional delay can arise. At these interfaces the Fresnel equations and the complex impedance of our metamaterial have to be taken into account. In order to clarify the influence of the interface, a thin homogeneous metal layer can be used. If one measured the total time delay for a thin layer of metal with the interferometer using red light, one would obtain a negative phase delay in this case. If one neglects the first term in equation (6.2), one might conclude that this thin metal layer had a negative refractive index. Of course, this is not true, as the refractive index of a metal is always positive. Thus, we have to check our measurements carefully with appropriate numerical calculations.

Additionally, for determining the phase delay we have to keep in mind that the phase is only defined modulo 2π. Hence, the studied layers have to be thin in order to guarantee that the phase delay caused by the propagation through the layer is less than one period of the used wavelength. For our metamaterials under study this condition is always fulfilled.

Figure 6.5 summarizes measured phase and group delays for various center wavelengths of our Gaussian pulses and the corresponding transmittance values. The measured transmittance agrees well with calculated data. The phase delay Δt_{ph} is negative for the entire

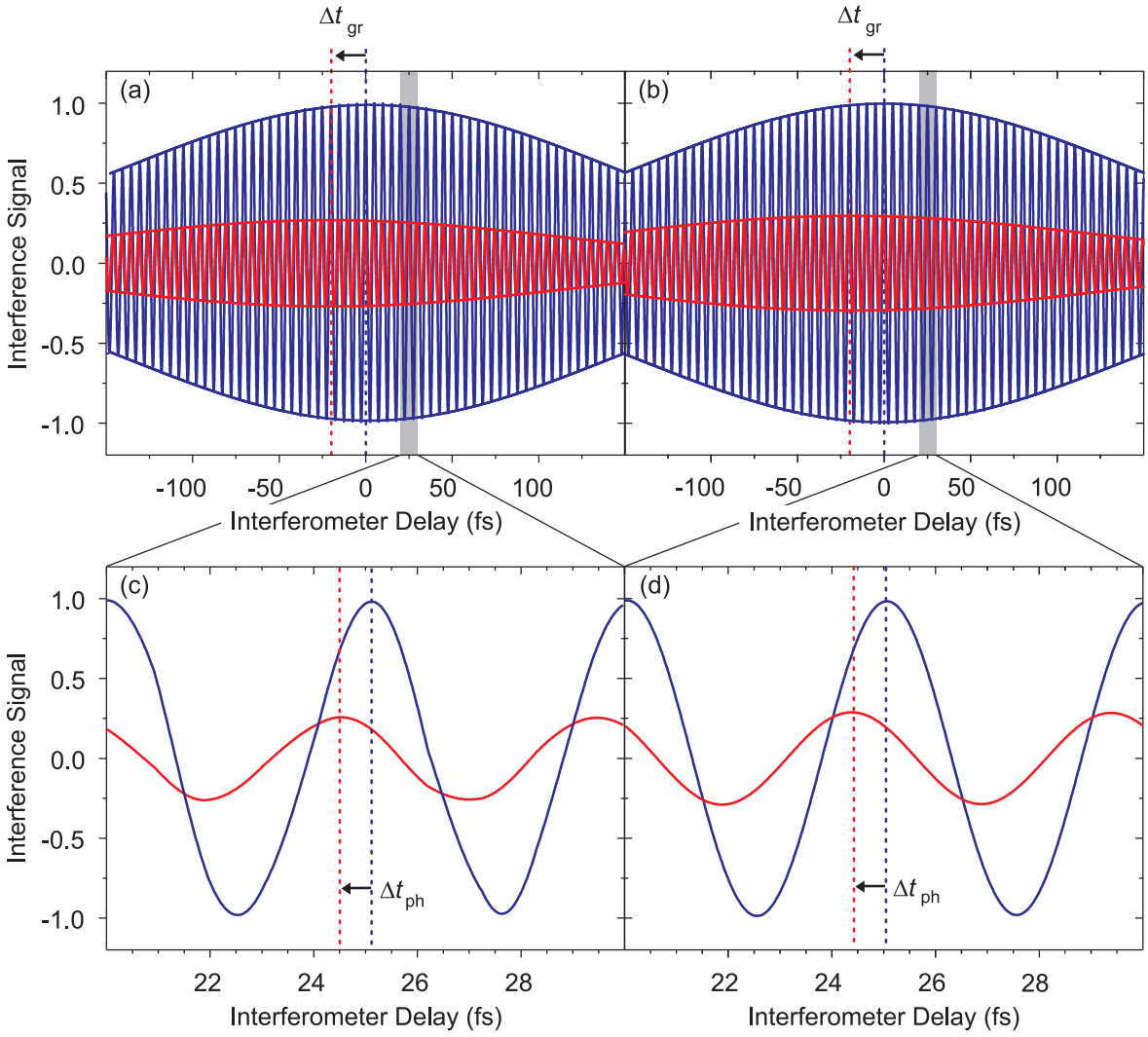

Figure 6.4: (a) Examples of typical measured interferograms (constant background subtracted for clarity), air interferogram (blue), and interferogram with metamaterial sample (red) are depicted. The center wavelength of the pulse is 1.5 µm. The Gaussian envelopes obtained from a least-squares fit to the interferogram extrema are depicted for both cases. The resulting negative group delay Δt_{gr} is indicated. (c) Enlarged view of two individual interference fringes. The resulting negative phase delay Δt_{ph} is indicated. The corresponding calculated data are shown in (b) and (d).

spectral range depicted. The group delay is either negative or positive. All measurements agree very well with our calculations. As described in the previous chapter, we directly use the numerical data without retrieving any parameters. However, using the retrieved material parameters would give strictly the identical result, because the complex transmittance and reflectance coefficients are strictly identical, owing on the principle of the retrieval procedure.

We start our discussion of the data in Fig. 6.5(b) by assuming that the phase delay is exclusively due to propagation. In this case, a negative refractive index requires phase delays more negative than $\Delta t_{\mathrm{ph}} = 0 - 0 - 2d/c_0$ according to equation (6.2). With the metamaterial

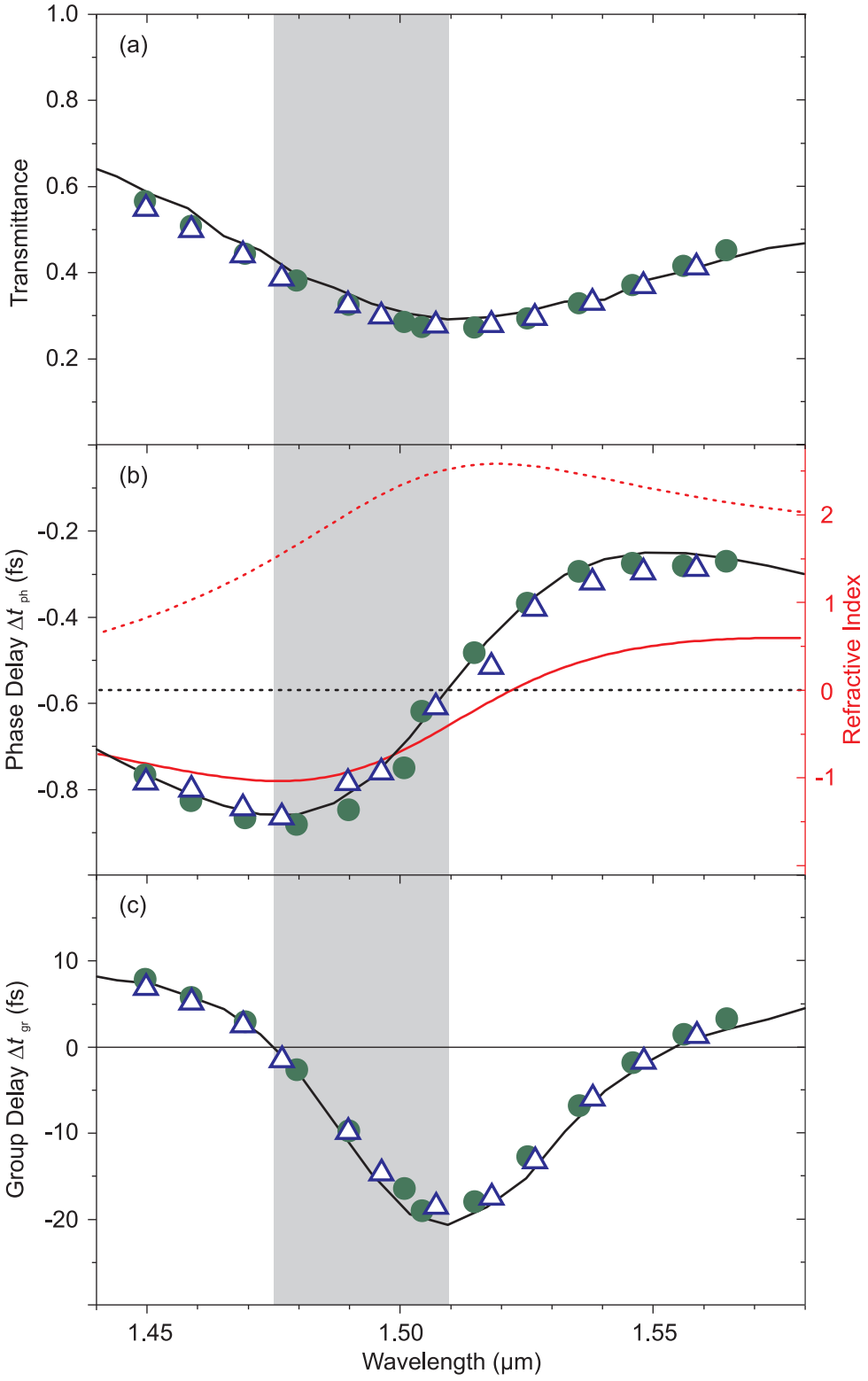

Figure 6.5: Summary of two different sets of experiments (blue triangles and green circles) on the sample shown in Fig. 6.1. The black curves show calculated data. (a) Transmittance spectra measured with Gaussian pulses. (b) Phase delay Δt_{ph}. A refractive index of $\mathrm{Re}(n) = 0$ together with the sample thickness of $d = 85\,\mathrm{nm}$ correspond to a propagation phase delay of $-2 \cdot 85\,\mathrm{nm}/c_0 = -0.57\,\mathrm{fs}$. This value is indicated by the black dashed horizontal line. Retrieved real (solid) and retrieved imaginary (dashed) part of the refractive index (red scale at right) are shown. (c) Group delay Δt_{gr} (compare with Fig. 6.4). The grey area highlights the regime with both $v_{\mathrm{ph}} < 0$ and $v_{\mathrm{gr}} < 0$ simultaneously.

thickness of $d = 85\,\mathrm{nm}$, we get the $\mathrm{Re}(n) = 0$ line at $\Delta t_{\mathrm{ph}} = -0.57\,\mathrm{fs}$, which is illustrated by the dashed horizontal line in Fig. 6.5(b). However, if the phase delay was exclusively due to propagation, the crossing of the phase delay curve with the $\mathrm{Re}(n) = 0$ line and the zero crossing of the real part of the refractive index should strictly coincide. We find a small spectral shift between the two crossings. This shift originates from an additional phase delay due to the interfaces air/metamaterial/substrate. As discussed before, one obtains phase delays from the Fresnel equations for complex metamaterial impedances. Multiple reflections between these interfaces further modify the phase. However, the additional phase delay is very small and thus can be approximately neglected. Considering the ratio between real part and imaginary part of the refractive index for this sample we find the FOM to be 1 at the maximum.

Now, we turn our focus on the group delay. Again, we assume that the group delay is exclusively due to propagation. In this case, we do not depict the $\mathrm{Re}(n) = 0$ line with $\Delta t_{\mathrm{gr}} = -0.57\,\mathrm{fs}$, since the measured and calculated group delays are much smaller than the phase delays. The smallest value we obtain for the group index is $n_{\mathrm{gr}} = -33$. Now, we consider the group delay in combination with the refractive index. For wavelengths above $1.55\,\mu\mathrm{m}$, the group delay and hence the group velocity is positive although the slope of the refractive index is negative. This is possible, since the value of the slope is very small and can be compensated by the positive real part of the refractive index [see equation (6.1)]. With decreasing wavelengths the slope steadily decreases and the group velocity gets negative. Here, the slope becomes smaller than $\mathrm{Re}(n)$. For shorter wavelengths, the slope turns again positive, the group velocity gets positive as well. Here, the negative real part of the refractive index cannot compensate for the large slope. In summary, the group velocity behaves exactly as expected from the characteristics of the refractive index combined with equation (6.1).

The measurements of the phase delay and the group delay provide a consistent picture of our metamaterial and the corresponding refractive index. Furthermore, these delay measurements are a very sensitive tool: While small modifications of the structural parameters have hardly any effects on the transmittance and reflectance spectra, the time delays act very sensitive on these variations. In addition, only these delay measurements provide the possibility to reveal the characteristics of the refractive index. Moreover, our measurements on negative group velocities are consistent with measurements performed in the microwave regime [92–95]. In summary, all possible combinations of positive (negative) phase velocities and group velocities have been measured at optical frequencies [96].

6.2 Low-loss negative-index metamaterial

Next, we optimize the FOM. For the cut-wire pairs [77], the maximum value was $\mathrm{FOM} \approx 0.1$ at $\mathrm{Re}(n) \approx -0.2$ around $1.5\,\mu\mathrm{m}$ wavelength. A precursor of the double-fishnet design gave $\mathrm{FOM} \approx 0.5$ at $\mathrm{Re}(n) \approx -1$ around $1.9\,\mu\mathrm{m}$ wavelength [97]. Later on the same group of authors showed experimental results obtained from the double-fishnet design with a maximum $\mathrm{FOM} \approx 1$ at $1.8\,\mu\mathrm{m}$ wavelength and a transmittance of approximately 40% [98]. The sample mentioned in the previous section already showed a FOM of one.

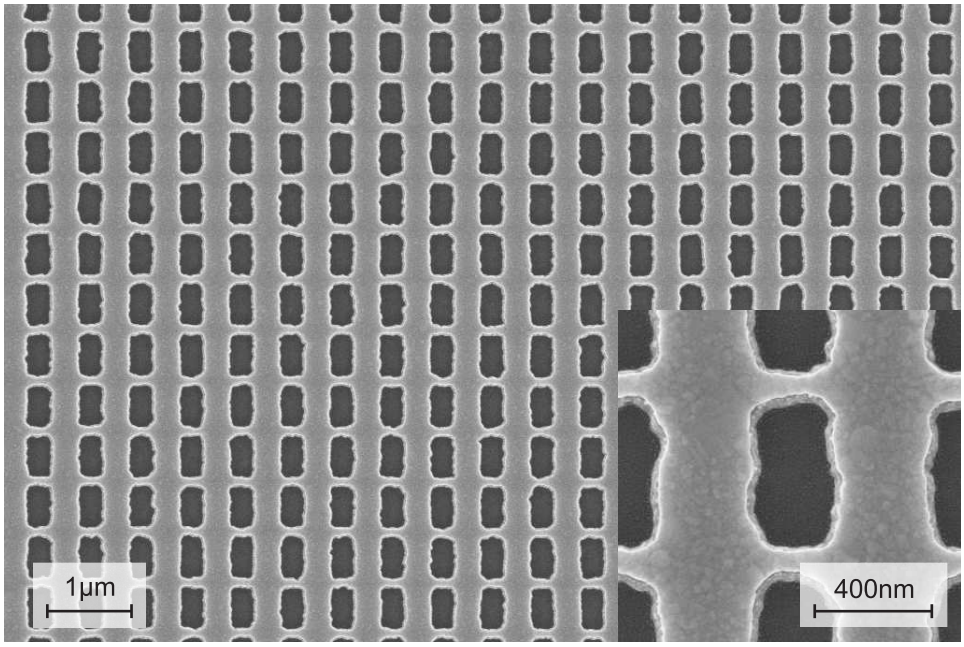

Figure 6.6: Top-view electron micrograph of the low-loss negative-index double-fishnet structure consisting of Ag/MgF_2/Ag. Parameters of the sample are: $t = 45$ nm, $s = 30$ nm, $w_x = 316$ nm, $w_y = 100$ nm, and lattice constant $a_x = a_y = a = 600$ nm. The metamaterial thickness is $d = 2t + s = 120$ nm. Inset, magnified view.

One important factor for loss is the usage of gold. As already described in chapter 2, the losses in silver are much lower. Thus, we optimized the geometrical parameters of the double-fishnet structure for silver, since the damping is reduced by a factor of four compared to gold [23]. Many parameters had to be varied carefully, to achieve a FOM as high as possible. Subsequently, we have fabricated a sample according to the parameter set of our simulations. Figure 6.6 reveals a high-quality silver film. The width of the thin wires is 100 nm. Hence, in this structure the aspect ratio of the height to the smallest lateral feature size is larger than one, which is very challenging from a fabricational point of view. Furthermore, the quality of the sample is obviously excellent. In Fig. 6.7(a) the measured spectra are shown. The solid lines indicate the measurements with the electric field oriented along the thin wires. Dashed lines correspond to the orthogonal incident polarization. Here the light field "sees" an effective metal with a large effective plasma frequency, hence low transmittance (high reflectance) over the entire spectral range is obtained.

These measured spectra are directly compared with numerical calculations [Fig. 6.7(b)] for our sample design. The plasma frequency used is $\omega_{\mathrm{pl}} = 1.37 \cdot 10^{16}\,\mathrm{s}^{-1}$, while the damping is $\gamma = 8.5 \cdot 10^{13}\,\mathrm{s}^{-1}$. The latter has been used as a free parameter. The resulting choice is somewhat larger than that of the literature [23] and effectively subsumes other loss channels, such as inhomogeneous broadening due to fabrication tolerances and radiative losses. The refractive index of the glass is $n = 1.48$, and that of the MgF_2 spacer is $n = 1.38$. In addition, we have as well measured the group delay [see Fig. 6.7(c)] and the phase delay [see Fig. 6.7(d)] for this sample. As already observed in the previously discussed sample, in a specific spectral region both the group velocity and the phase velocity are simultaneously

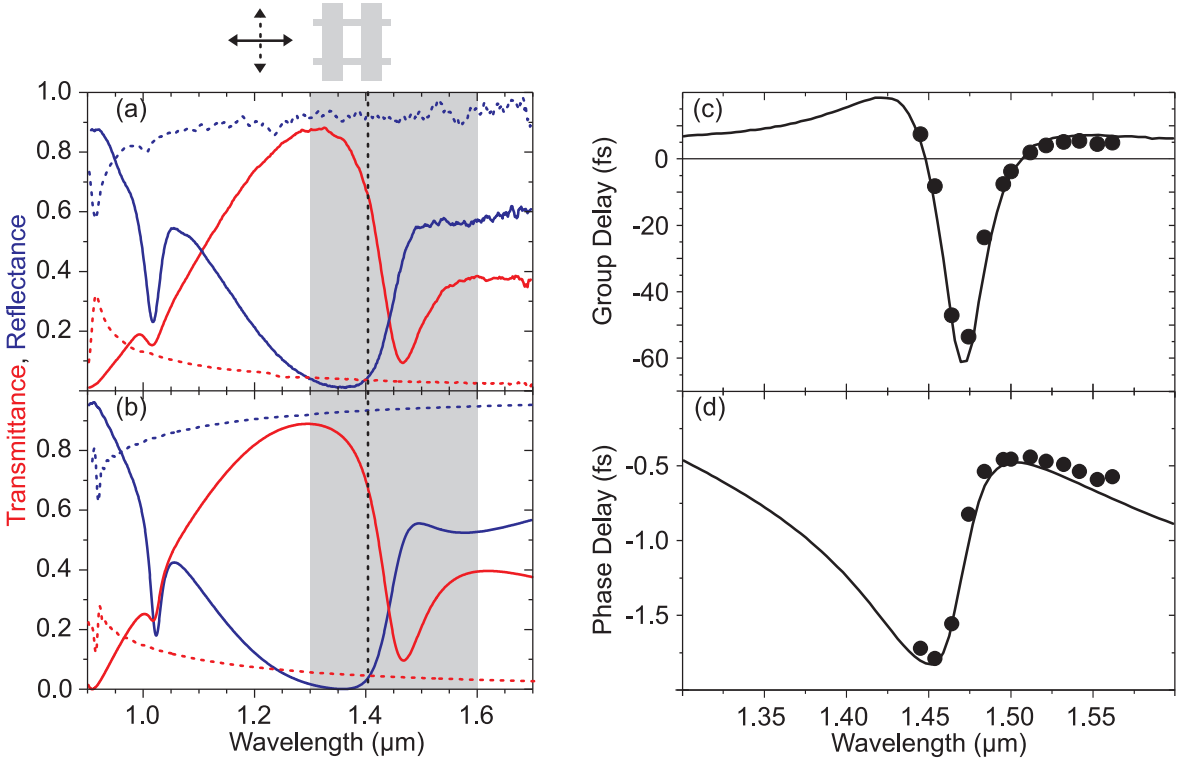

Figure 6.7: (a) Measured normal-incidence transmittance (red) and reflectance (blue) spectra for the incident polarization depicted on top. (b) Corresponding calculated spectra. Grey area, spectral region shown in Fig. 6.8; dashed vertical line, position of $\mathrm{Re}(n) = -1$, where the FOM is -3. (c),(d) Interferometric time-resolved experiments (dots) with the incident light polarized like the solid curves in (a). The solid curves are calculations with parameters identical to those in (b). (c) group-delay Δt_{gr} spectrum, (d) phase-delay Δt_{ph} spectrum.

negative. However, in this case the group velocity is more negative, since the damping of silver is smaller than that of gold.

It is apparent that the overall agreement between experiment and theory in Fig. 6.7 is extremely good. This gives us sufficient confidence into the theoretical results to retrieve the effective metamaterial parameters from the theory for the relevant linear polarization [see solid curves in Fig. 6.7(a)]. For the thickness of the metamaterial we have taken the physical thickness of $d = 2t + s = 120\,\mathrm{nm}$. We embedded the metamaterial structure in an effective homogeneous medium with refractive index $n = 1.05$. Using vacuum would slightly shift all resonances to the blue, hindering a direct comparison with Fig. 6.7. Figure 6.8 shows the retrieved complex parameters. Notably, we obtain a refractive index $\mathrm{Re}(n) = -2$ around $1.45\,\mu\mathrm{m}$ wavelength in (c). As expected, the permittivity ε in (a) closely resembles the permittivity of a diluted Drude metal, whereas μ exhibits a magnetic resonance behavior. The corresponding FOM is shown in (d). It reaches a maximum of $\mathrm{FOM} \approx 3$ at a spectral position where $\mathrm{Re}(n) \approx -1$. To the best of our knowledge, this is the largest value reported for any negative-index photonic metamaterial operating at optical frequencies to date [99].

However, there is a good reason, why most metamaterials operating at optical frequencies are based on gold: silver oxidizes with time. Therefore, we have studied the long-term

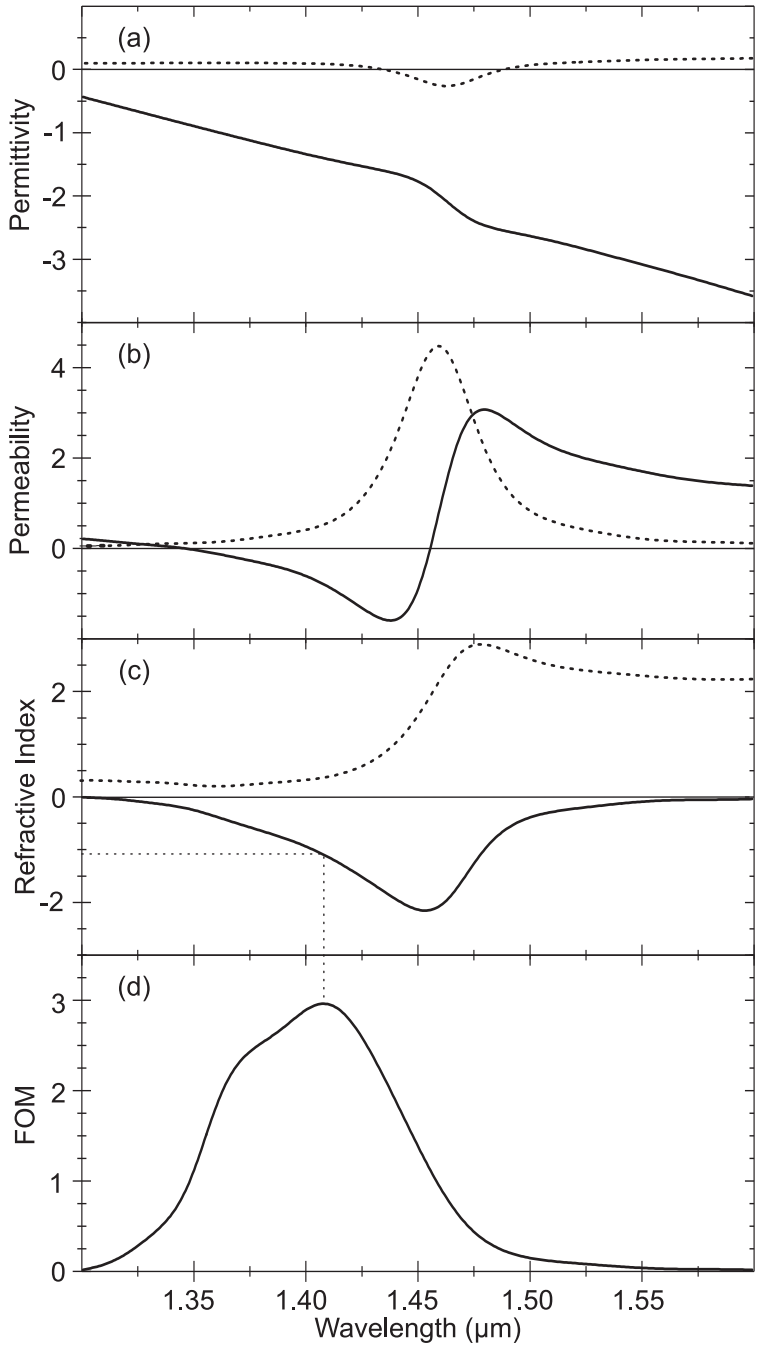

Figure 6.8: (a) Retrieved permittivity ε, (b) retrieved magnetic permeability μ, and (c) refractive index n. Solid curves correspond to real parts; dashed curves correspond to imaginary parts. (d) FOM. Dashed vertical line indicates spectral position, where the FOM reaches its largest value.

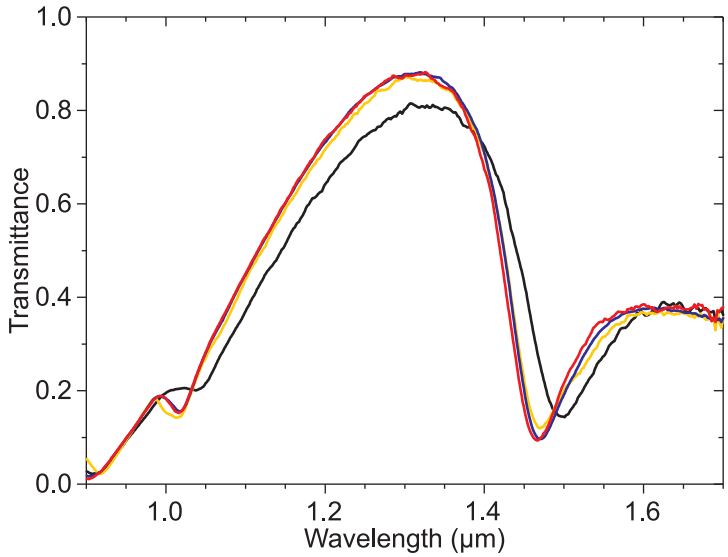

Figure 6.9: Measured normal-incidence transmittance spectra for the relevant incident polarization. Red curve corresponds to the solid transmittance curve in Fig. 6.7(a). Blue curve, taken one week later; yellow curve, taken two weeks later; black curve, taken one year later.

behavior of our sample. The obtained results are depicted in Fig. 6.9. The red curve corresponds to the solid red curve in Fig. 6.7(a). The spectra measured one and two weeks after the first measurement match well to the red curve within the measuring accuracy. This shows, that within two weeks the aging is negligible. However, the spectrum taken one year after the fabrication of the sample, shows larger deviations. On the one hand, the resonance is shifted to longer wavelengths. On the other hand, the resonance itself is less pronounced, which corresponds to an increase of the damping in the metal. This behavior was also observed in other silver samples. In summary, we have enough time to perform all important experiments.

6.3 Negative-index metamaterial operating in the visible

The shortest wavelength of a negative-index metamaterial was at telecommunication wavelengths. However, the following section deals with a structure having a negative refractive index at the red end of the visible spectrum (780 nm wavelength) for the first time [14]. In Figure 6.10(a) the sample is schematically depicted. Figure 6.10(b) shows a SEM image of the corresponding structure and reveals large-scale homogeneity as well as a 68 nm minimum lateral feature size at 97 nm thickness of the Ag/MgF_2/Ag sandwich. This aspect ratio, exceeding unity, poses again significant fabrication challenges. Compared to the already discussed samples, especially the relative width of the metal wires orientated along the electric field vector [i.e., the ratio w_y/a_y in Fig. 6.10(a)] had to be increased. This step increases the effective plasma frequency, which needs to be above the operation frequency to yield a negative electric permittivity.

Figure 6.11(a) shows measured normal-incidence intensity transmittance and reflectance

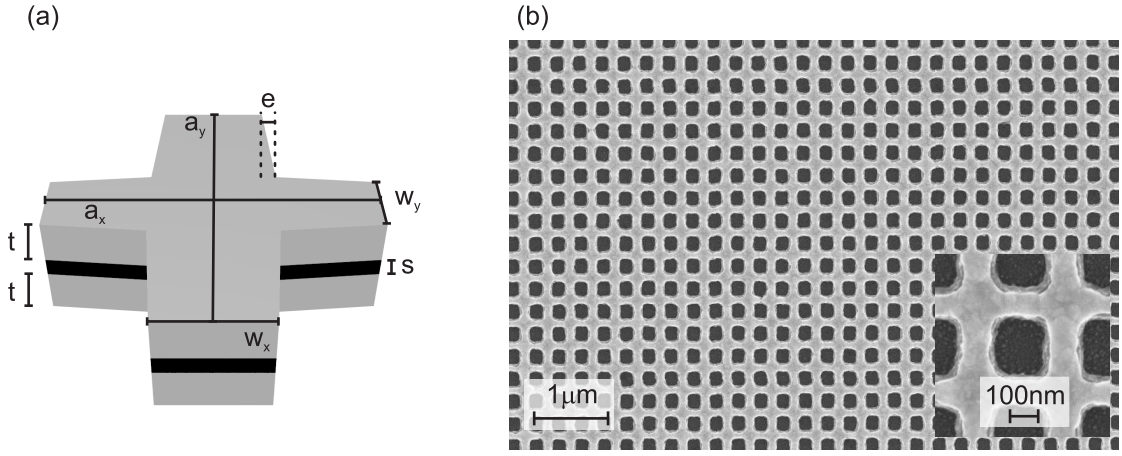

Figure 6.10: (a) Unit cell of the structure with definition of parameters: lattice constant $a_x = a_y = a = 300\,\text{nm}$, $w_x = 102\,\text{nm}$, $w_y = 68\,\text{nm}$, $t = 40\,\text{nm}$, $s = 17\,\text{nm}$, and $e_x = e_y = e = 8\,\text{nm}$. The last parameter describes small deviations from rectangular shape. (b) Top-view electron micrograph of the sample employed in Figs. 6.11 and 6.12. Inset, magnified view.

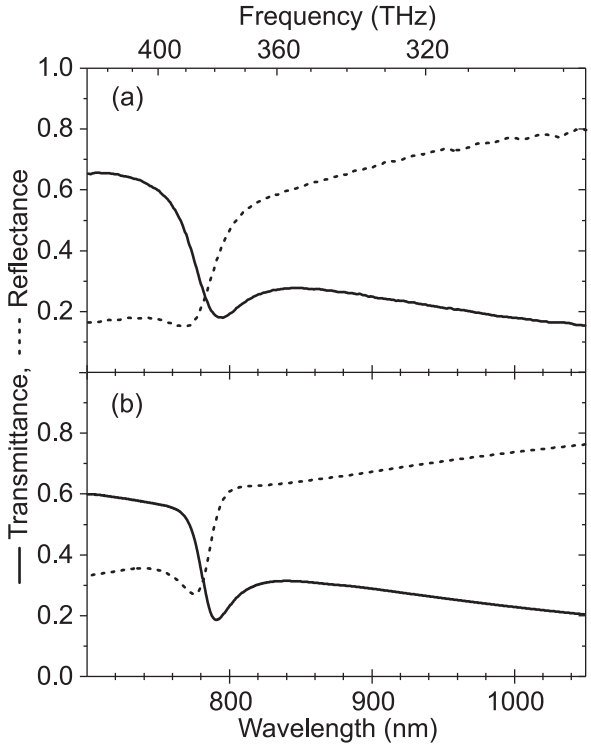

Figure 6.11: (a) Measured transmittance (solid) and reflectance (dashed) spectrum of the negative-index metamaterial for light polarized parallel to the $x-$axis. (b) Corresponding theoretical calculation. The same parameters are used in the calculations depicted in Fig. 6.12.

spectra of this metamaterial sample. Optical material parameters taken in the calculations shown in (b) are the MgF_2 refractive index $n = 1.38$, the glass substrate refractive index $n = 1.5$, and the Drude model for silver with a plasma frequency of $\omega_{\text{pl}} = 1.37 \cdot 10^{16}\,\text{s}^{-1}$ and a damping of $\gamma = 9 \cdot 10^{13}\,\text{s}^{-1}$. It is important that exactly the same set of parameters will be

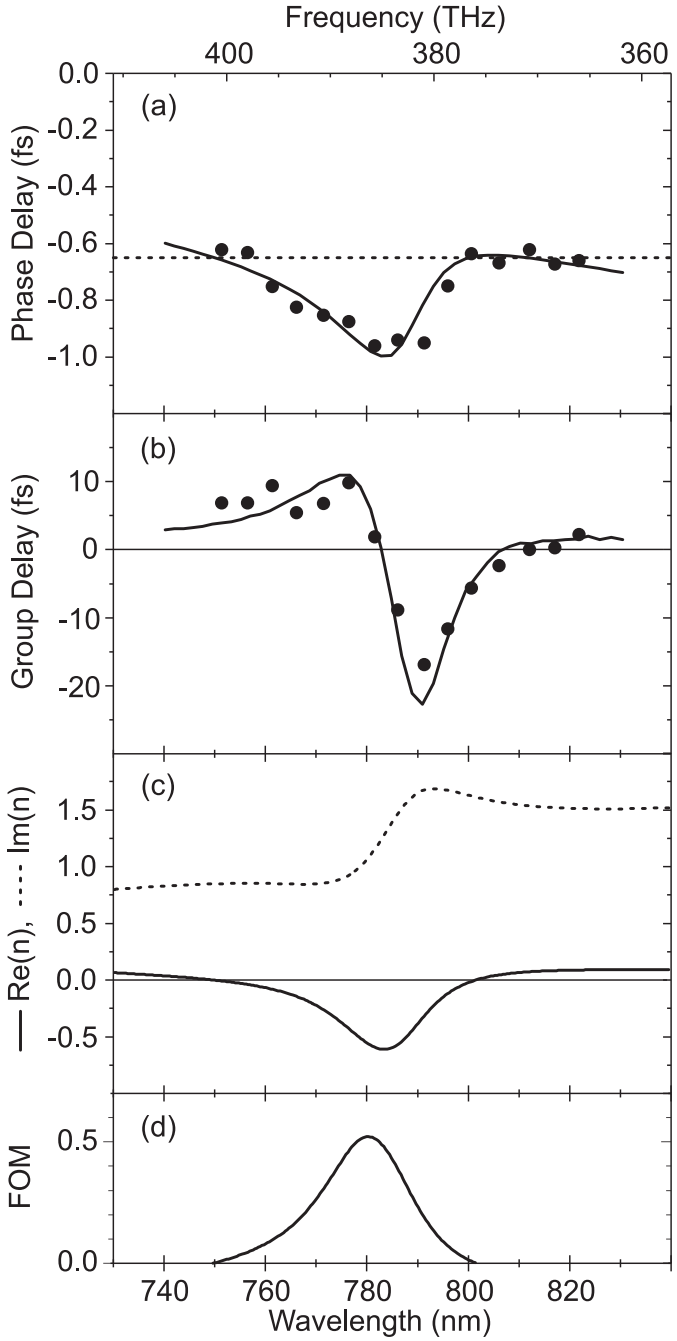

Figure 6.12: (a) Measured (dots) phase delay versus laser center wavelength for a pulse propagating through the metamaterial sample for the relevant polarization. The solid curve is the corresponding theoretical calculation. The dashed horizontal line corresponds to the $\mathrm{Re}(n) = 0$ line. (b) Group delay versus wavelength. (c) Retrieved real (solid) and imaginary (dashed) part of the refractive index n. (d) Resulting FOM. The same set of sample parameters is used in all calculations in Figs. 6.11 and 6.12.

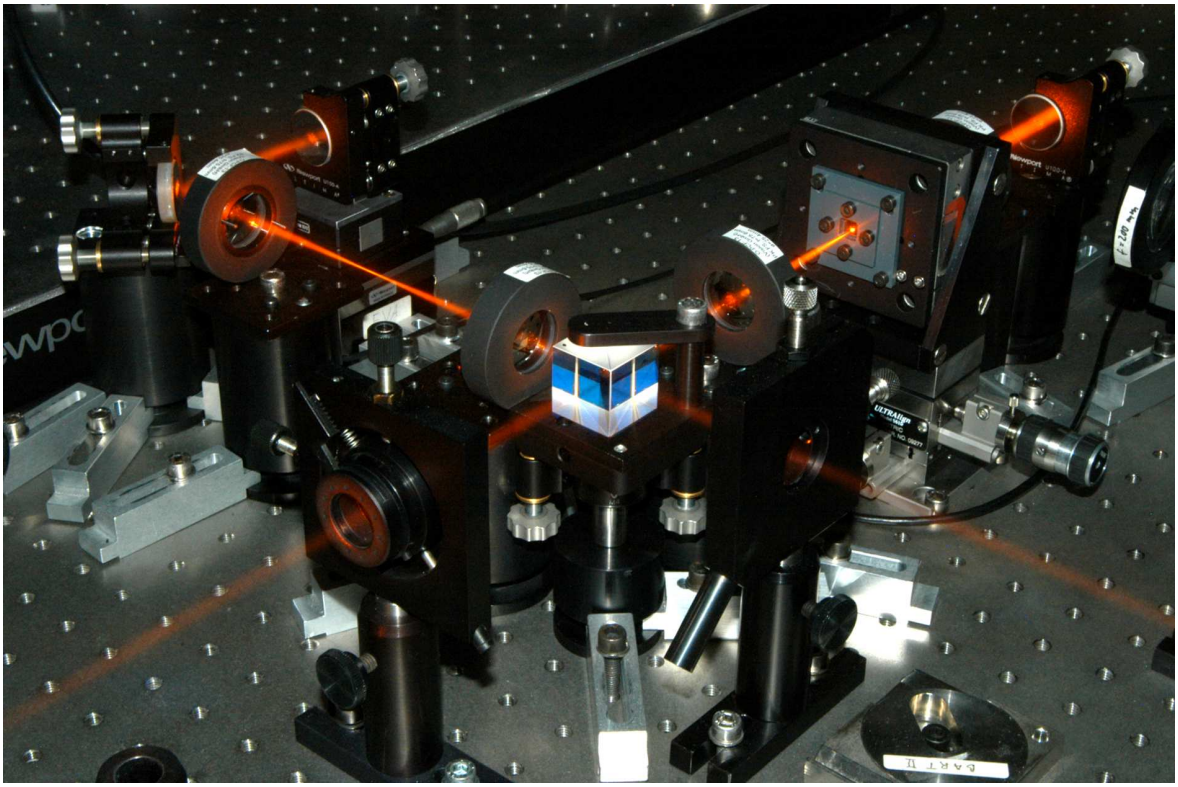

Figure 6.13: The Michelson interferometer used for the phase- and group delay measurements is shown. Here, the laser center wavelength is 780 nm. The red light is not an artefact of the digital camera, but can also be seen by the naked eye.

used later on in the theoretical analysis of the interferometric experiments as well as in the effective parameter retrieval.

Measured phase delay and group delay spectra (dots) are shown in Figs. 6.12(a) and (b) together with numerical calculations (solid curves). Finally, we retrieve the effective material parameters from theory and depict them in Fig. 6.12(c). From the increasing relative importance of the imaginary part of the silver dielectric function for frequencies (even remotely) approaching the plasma frequency, one expects increased losses. Indeed, the FOM shown in Fig. 6.12(d) is $\mathrm{FOM} = 0.5$ at best at a wavelength of 780 nm. The FOM is below 1, because the real part of the permeability stays positive in the entire spectral range.

Obviously, the experimental results agree well with theory, which consistently describes transmittance and reflectance spectra as well as phase delay and group delay spectra, all with one identical set of parameters. Thus, the effective material parameters, especially the negative real part of n retrieved from the same theory and the same parameters can be considered as very trustworthy. In conclusion, we have demonstrated a metamaterial with an effective real part of the refractive index of -0.6 around 780 nm wavelength. This wavelength can easily be seen with the naked eye in our laser experiments as can be seen in Fig. 6.13. Our work goes beyond previous work in the visible [100, 101], which claimed a negative magnetic permeability.

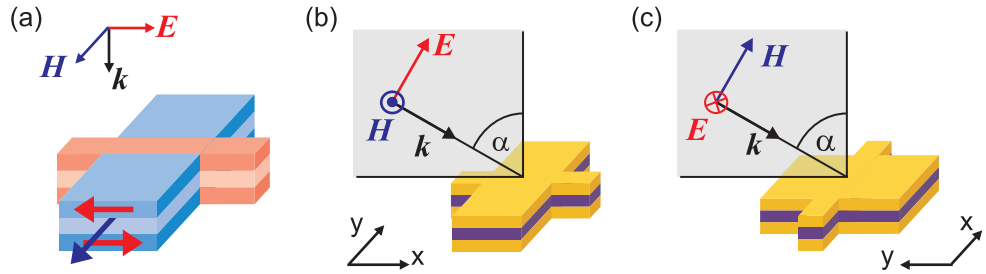

Figure 6.14: (a) The magnetic atom (blue) and the electric atom (red) in one unit cell are highlighted. The blue and red arrows schematically indicate a snapshot of the magnetic- and electric-dipole vectors, respectively. (b),(c) Scheme of measurement geometry. In (b) the sample is rotated around the axis with the broad stripes. This corresponds to an in-plane wave vector $\boldsymbol{k}_{||} = k_{||}(\cos(\varphi), \sin(\varphi)) = k_{||}(1, 0)$. In (c) the sample is rotated with the axis pointing along the thin wires. This corresponds to an angle of $\varphi = \pi/2$ with $k_{||}(0, 1)$. For all measurements, the electric field is oriented parallel to the thin wires. The parameters of the sample are: $a = 605\,\text{nm}$, $w_x = 324\,\text{nm}$, $w_y = 100\,\text{nm}$, $t = 30\,\text{nm}$, and $s = 32\,\text{nm}$. The layer sequence is Au/MgF_2/Au.

6.4 Observation of magnetization waves

Up to now we have neglected any interaction between different unit cells. In other words, the optical properties of the metamaterial are the result of the optical properties of the individual photonic atoms. One step beyond that [102], the electric dipole-dipole and magnetic dipole-dipole interactions between next-nearest neighbors (and beyond) lead to a coupling of the photonic atoms. In the present context, one can distinguish between four different types of couplings: On the one hand, electric (e) and magnetic (m) dipole-dipole interactions, respectively; on the other hand, transverse ($\perp$) and longitudinal ($||$) waves, respectively. Here, transverse and longitudinal refer to the dipole orientation with respect to the in-plane wave vector $\boldsymbol{k}_{||} = (k_x, k_y)$ of the excitation. The theory for all four cases has been evaluated [103, 104].

Intuitively, the interaction between equally orientated dipoles – be it electric or magnetic – is attractive (repulsive) for a spatially homogeneous longitudinal (transverse) arrangement. Thus, the energetic minimum (maximum) of the dispersion relation $E(\boldsymbol{k}_{||})$ occurs for zero in-plane momentum $\boldsymbol{k}_{||}$, and finite wave numbers increase (decrease) the energy. Note that electric and magnetic dipoles are usually perpendicular to each other. This means that, e.g., the electric transverse case competes with the magnetic longitudinal case. Thus, the photon energy increases or decreases with wave number, depending on wether electric or magnetic dipole-dipole interactions dominate. The question which one dominates cannot easily be answered *a priori*.

Here, we study a sample closely similar but not identical to the previously discussed sample with a FOM ≈ 3. Instead of silver we used gold as a metal. The sample parameters are given in Fig. 6.14. Moreover, the measurement geometry is illustrated and the corresponding parameters are introduced. Coupling to the above mentioned modes is accomplished by oblique incidence of light onto the metamaterial layer. This geometry leads to a modulus of the in-plane wave number $k_{||}$ given by

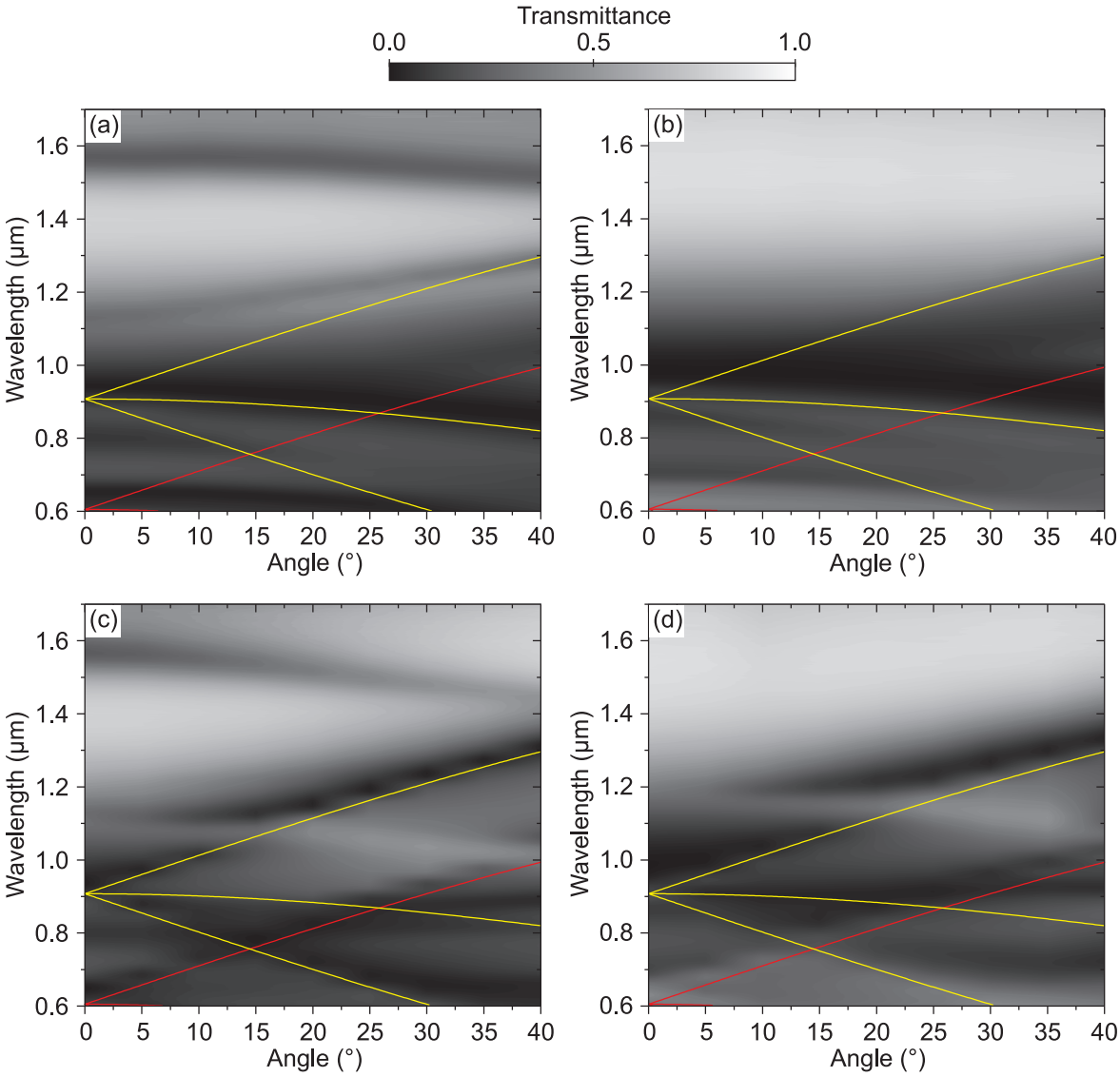

Figure 6.15: (a), (c) depict angular resolved measurements of the double-fishnet structure and (b), (d) of an identical structure yet without the top gold layer. The first row corresponds to an angle of $\varphi = \pi/2$, the second row to $\varphi = 0$ (compare with Fig. 6.14). The angle of incidence α is varied from $0°$ to $40°$ in $5°$ steps. The Wood anomalies with $n_i = n_1 = 1$ are depicted in yellow, the Wood anomalies with $n_i = n_2 = 1.5$ in red.

$$k_{||} = \frac{2\pi}{\lambda} \sin(\alpha), \tag{6.3}$$

with the incident (vacuum) wavelength of light λ. By choosing different axes of rotation, different principal directions in reciprocal space can be investigated. Figure 6.14 illustrate the two cases $\boldsymbol{k}_{||} = k_{||}(\cos(\varphi), \sin(\varphi)) = k_{||}(1, 0)$ and $k_{||}(0, 1)$. For the sample parameters given in Fig. 6.14, for $\alpha = 40°$ and for $\lambda = 1.5\,\mu$m, the modulus of the in-plane wave vector reaches a value greater than $k_{||} = 0.5\pi/a$. This means that a substantial fraction of the Brillouin zone can be investigated along these lines.

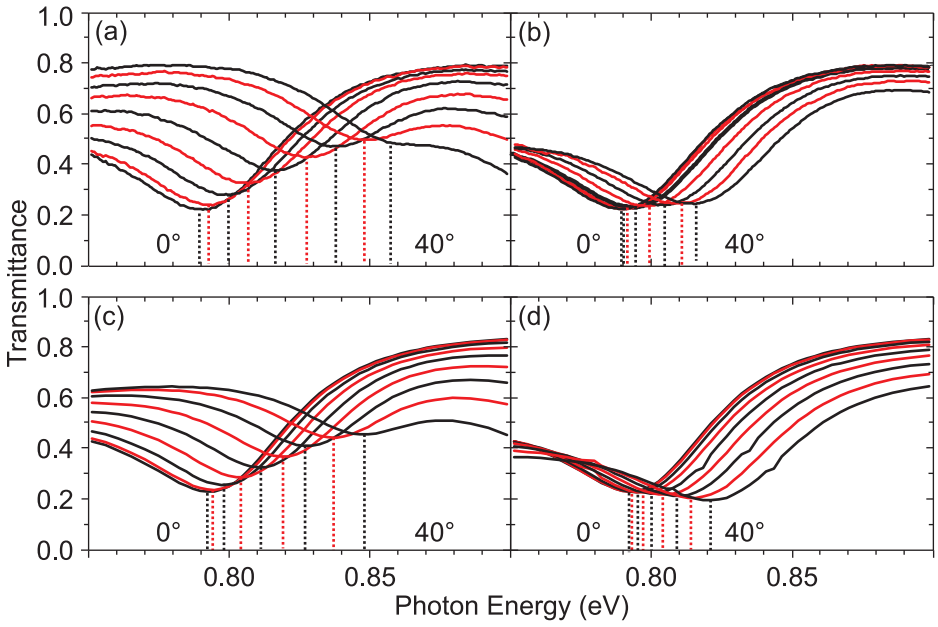

Figure 6.16: (a),(b) Measured oblique-incidence transmittance spectra for different angles α with respect to the surface normal, from $0°$ to $40°$ in steps of $5°$ (for clarity, the color alternates between black and red). The in-plane wave vector is $\boldsymbol{k}_{||} = k_{||}(1, 0)$ in (a) and $k_{||}(0, 1)$ in (b). (c),(d) Calculated spectra corresponding to (a) and (b), respectively.

However, before we address the interaction of the dipoles, we study the characteristics of the structure for a large spectral range. In order to unambiguously identify the magnetic resonance, we have fabricated two identical samples, yet one without the top gold layer. The experimental results of both the negative-index sample and the control sample are shown in Fig. 6.15. For wavelengths shorter than 1 µm we observe a rich behavior for both samples. Besides the Wood anomalies additional resonances are excited in the metal stripes. One can also clearly observe the interaction of these resonances with the Wood anomalies. By comparing the experimental results of the negative-index sample and the control sample, we realize that only the resonance at around 1.55 µm does only appear in the spectra of the negative-index sample and not in the spectra of the control sample. This resonance corresponds to the magnetic resonance. We restrict ourselves to this long-wavelength resonance which moreover is not near any Wood anomalies. Furthermore, we now change from wavelengths to energies as we study interaction effects.

Experimental transmittance spectra of the metamaterial sample are shown in Fig. 6.16. For both oblique-incidence geometries shown, the transmittance dip shifts to higher photon energies (shorter wavelengths) with increasing angle α. To further analyze these findings, we plot the photon-energy position of the transmittance dips (see vertical dashed lines in Fig. 6.16) versus in-plane wave number $k_{||}$. The latter can easily be calculated from the angle α. The resulting measured dispersion relations are shown in Fig. 6.17. For the structure under investigation the electric dipoles are orientated along the x direction and the magnetic-dipole moments are orientated along the y direction [also see Fig. 6.14(a)]. Thus, the spectral shape of the dispersion relations indicates that the longitudinal electric dipole-dipole coupling is

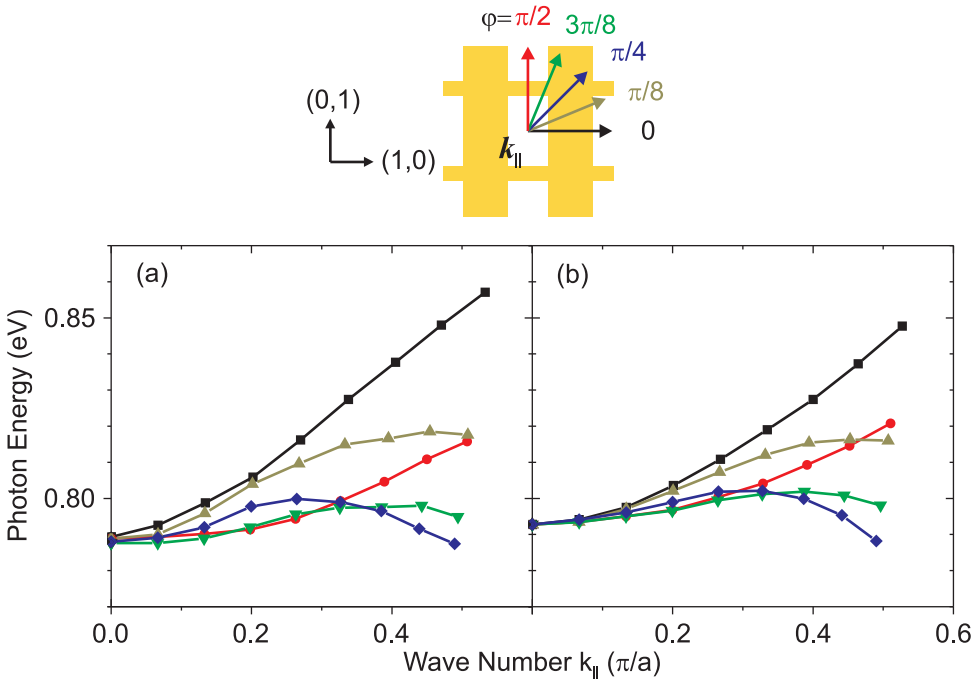

Figure 6.17: Photon energies of transmittance dips (see vertical dashed lines in Fig. 6.16) versus in-plane wave number $k_{||}$ as determined from the angle α. (a) Experiment, (b) theory. Propagation directions are indicated by the in-plane wave vector $\vec{k}_{||} = k_{||}\,(\cos(\varphi), \sin(\varphi))$ and illustrated at the top. $\varphi = 0$ corresponds to Figs. 6.16(a) and (c), $\varphi = \pi/2$ to Figs. 6.16(b) and (d).

dominant for propagation along $k_{||}(1,0)$, whereas longitudinal magnetic dipole-dipole coupling is dominant for propagation along $k_{||}(0,1)$ (otherwise the photon energy in Fig. 6.17 should decrease rather than increase with increasing modulus of the in-plane wave number). Waves resulting from magnetic dipole-dipole interactions have recently been discussed theoretically and have been called "magneto-inductive" waves [104]. These magnetization waves are the classical analogue of magnons for interacting quantum-mechanical spins. So far, these waves have only been observed experimentally at megahertz frequencies [105]. Recently, a similar behavior has been observed at infrared wavelengths [106]. Figure 6.17 also shows propagation directions different from the two principal directions $\boldsymbol{k}_{||} = k_{||}(1,0)$ and $\boldsymbol{k}_{||} = k_{||}(0,1)$. Here, the behavior is more complex and the photon energy versus in-plane momentum is a non-monotonous function. We interpret this behavior in terms of the nontrivial competition between the four types of interactions (see discussion above): electric/magnetic and transverse/longitudinal.

To further test our interpretations, we compare the measured data with numerical calculations based on JCMsuite. Geometrical parameters are as shown in Fig. 6.14. For the permittivity of gold we assume a Drude behavior with a plasma frequency of $\omega_{\mathrm{pl}} = 1.33 \cdot 10^{16}\,\mathrm{s}^{-1}$ and a damping of $\gamma = 1.15 \cdot 10^{14}\,\mathrm{s}^{-1}$. The refractive index of the glass substrate is taken as $n = 1.5$ and that of the MgF_2 spacer as $n = 1.38$. Calculated results are shown in Figs. 6.16(c), (d), and 6.17(b). Obviously, very good agreement between experiment and theory is obtained. In particular, the calculated dispersion relations quantitatively agree with

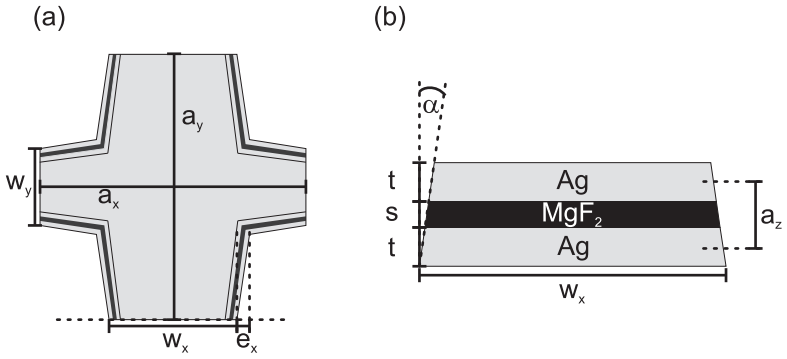

Figure 6.18: Scheme of the metamaterial with $N = 1$ functional layers under investigation. (a) Top view on one unit cell, (b) side view. The geometrical parameters are: $a_x = a_y = a = 645\,\text{nm}$, $w_x = 318\,\text{nm}$, $w_y = 173\,\text{nm}$, $\alpha = 8°$, $t = 31\,\text{nm}$, $s = 21\,\text{nm}$, and $e_x = e_y = 14\,\text{nm}$.

the experimental ones and reproduce the observed anisotropy regarding propagation along the two principal directions $\boldsymbol{k}_{||} = k_{||}(1,0)$ and $\boldsymbol{k}_{||} = k_{||}(0,1)$ as well as for the other three directions.

Finally, we address the question which parts of the negative-index structure are important for the observed couplings. If, for example, the thin metal double wires [marked red in Fig. 6.14(a)] are completely eliminated in the calculations, the transmittance dips in Fig. 6.16 show hardly any influence on α. This observation indicates that the thin metal double wires mediate both the above-mentioned strong electric and magnetic dipole-dipole couplings. This observation also unambiguously shows that the observed spectral shifts are not a property of the isolated magnetic atoms.

6.5 First steps towards three-dimensional photonic metamaterials

All studies and previous discussions on negative-index metamaterials at optical wavelengths investigated single functional layers only. It is well known, for instance, from electronic crystals, that the surface or a monolayer can exhibit properties that are rather different from the bulk. Thus it is relevant to investigate whether the optical constants of a single layer of a negative-index metamaterial really correspond to those of many layers (bulk).

A single functional layer is shown in Fig. 6.18. The obvious first approach to extend this structure into the third dimension is to stack this building block consisting of metal-dielectric-metal (mdm) with an additional spacer layer inbetween (i.e., mdm-spacer-mdm-spacer-...) several or many times [107]. A simplified design results from simply eliminating the additional spacer between the building blocks and merging the adjacent pairs of metal layers into one, leading to the simple layer sequence mdmdmdmdm.... Note, that the lattice constant along the stacking direction, a_z, becomes much smaller than the wavelength of light. This means that the effective-medium approximation is very well justified. Indeed, the design used in the experiments below uses 31 nm silver and 21 nm MgF_2; hence $a_z = 52\,\text{nm}$,

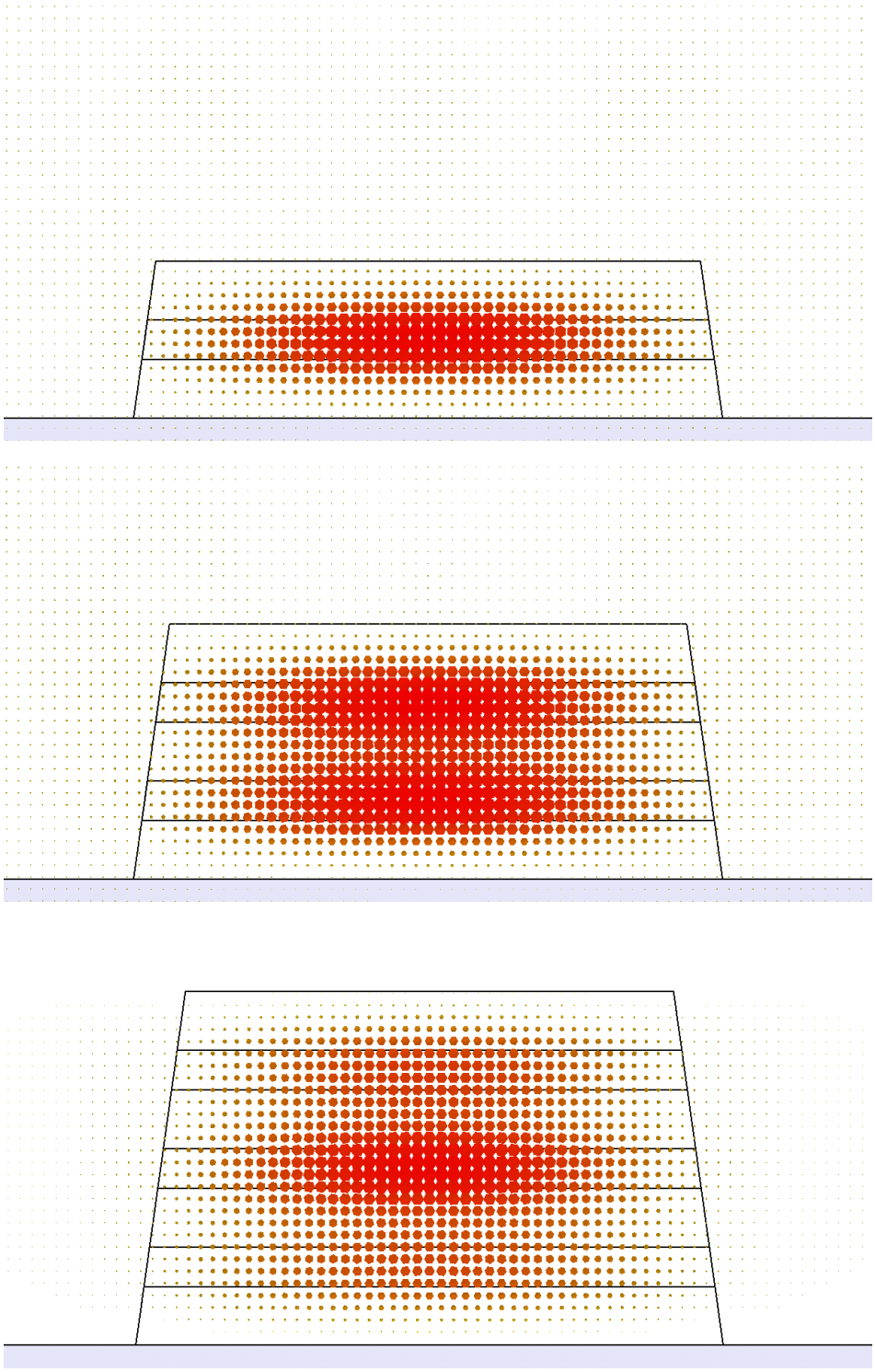

Figure 6.19: Snapshot of the $\boldsymbol{H}$ field (linear scale) for $N = 1$ (top), $N = 2$ (middle), and $N = 3$ (bottom) functional layers and a wavelength of $1.43\,\mu$m for the plane indicated by the dashed horizontal line in Fig. 6.18.

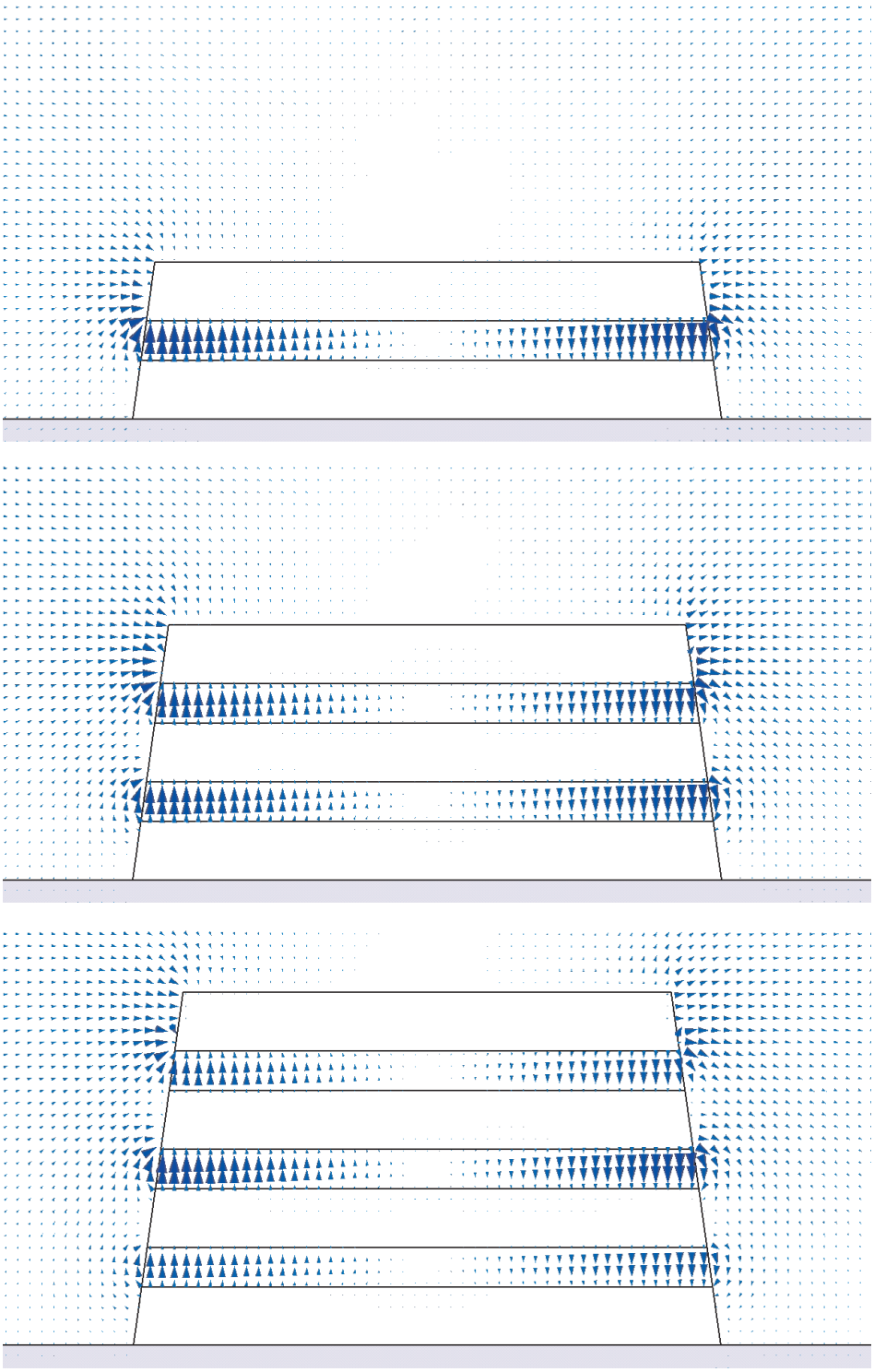

Figure 6.20: Snapshot of the $\boldsymbol{E}$ field (linear scale) for $N = 1$ (top), $N = 2$ (middle), and $N = 3$ (bottom) functional layers and a wavelength of $1.43\,\mu m$ for the plane indicated by the dashed horizontal line in Fig. 6.18.

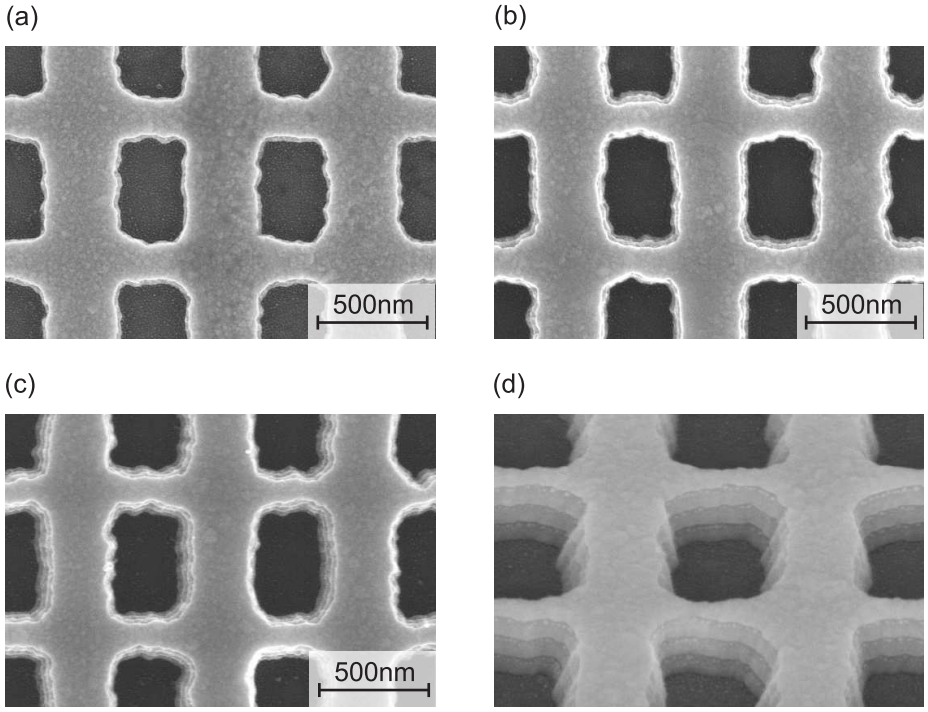

Figure 6.21: Top view electron micrographs of a modified double-fishnet structure with $N = 1$ functional layer (a), $N = 2$ functional layers (b), and $N = 3$ functional layers (c). (d) Electron micrograph of a structure similar to (c) with (oblique) viewing angle of $50°$. One can clearly observe the layer sequence.

which is 27 times smaller than the operational wavelength of $1.44\,\mu$m. Numerical calculations show that the magnetic-dipole moments of the three different functional layers add up to a finite macroscopic magnetic field. The corresponding $\boldsymbol{H}$ is illustrated in Fig. 6.19. It results mainly from the displacement current, i.e., from $-\mathrm{i}\omega\boldsymbol{D} = -\mathrm{i}\omega\varepsilon_0\varepsilon\boldsymbol{E}$ in the frequency domain. To illustrate this aspect, Fig. 6.20 shows a snapshot of the $\boldsymbol{E}$ field phase shifted by $90°$ with respect to Fig. 6.19. In addition, the corresponding fields are shown for $N = 1$ and $N = 2$ functional layers in the respective graphs. The similarities of the field distributions for the different numbers of functional layers can be clearly observed.

Due to the fabrication method of our samples, we end up with nonrectangular side walls, typically with an angle α of $8°$ with respect to the substrate normal on all sides. Obviously, this effect becomes particularly influential for thick samples like the multilayer structures of interest here. Corresponding SEM images are shown in Fig. 6.21. All other geometrical parameters are indicated in Fig. 6.18; optical parameters taken are a MgF_2 refractive index of $n = 1.38$, a glass substrate refractive index of $n = \sqrt{2.2}$, a plasma frequency of $\omega_{\mathrm{pl}} = 1.37 \cdot 10^{16}\,\mathrm{s}^{-1}$ and a damping of $\gamma = 8.5 \cdot 10^{13}\,\mathrm{s}^{-1}$.

Figure 6.22 compares measured and calculated normal-incidence transmittance and reflectance spectra for the two orthogonal linear incident polarizations indicated at the top and for $N = 1$, $N = 2$, and $N = 3$ functional layers. Three functional layers correspond to seven actual layers, i.e., the sequence mdmdmdm on top of the glass substrate. Horizontal polarization leads to a negative refractive index (see below); vertical polarization merely serves as a consistency check. The overall agreement between experiment and theory in

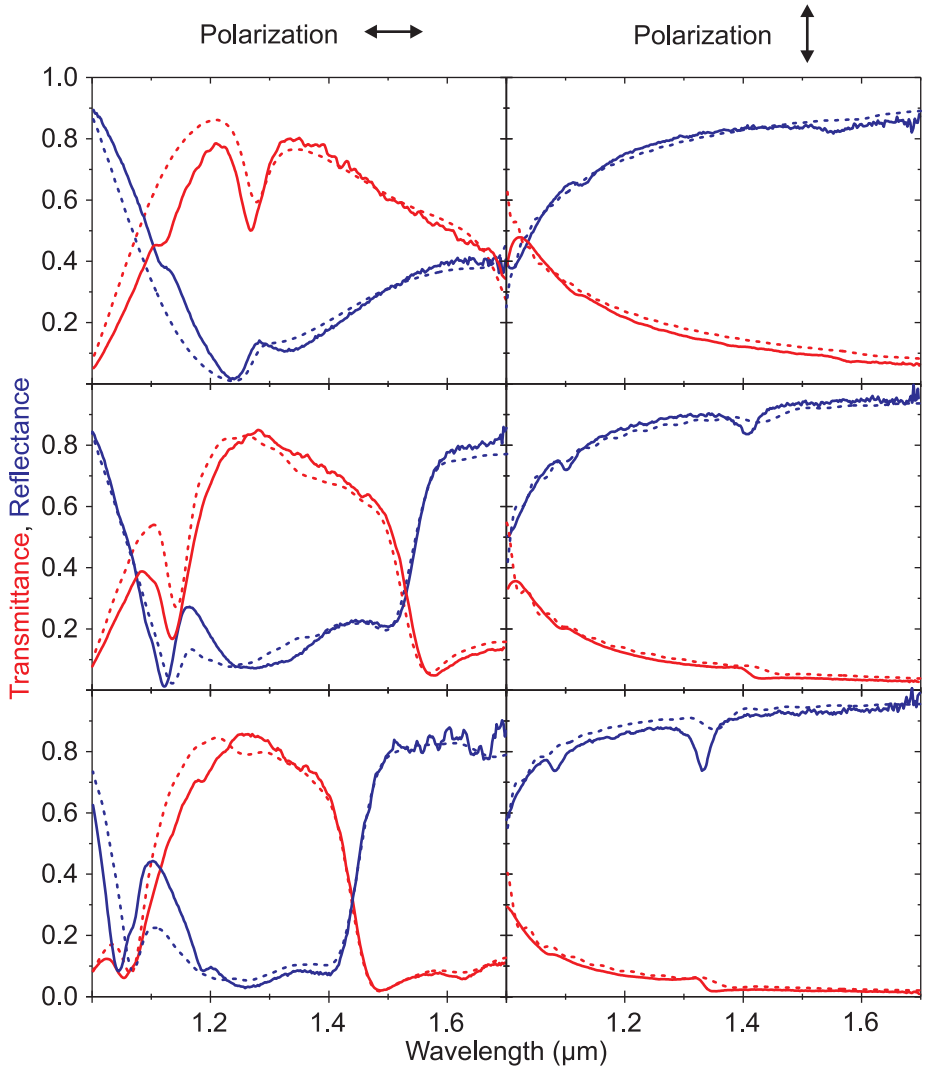

Figure 6.22: Measured (solid) and calculated (dashed) normal-incidence transmittance (red) and reflectance (blue) spectra for the relevant horizontal incident polarization in the left-hand column. For completeness and as a consistency check, the vertical polarization is shown in the right-hand column. The first, second, and third rows correspond to $N = 1, 2, 3$ functional layers, respectively.

Fig. 6.22 is very good – even for the rather complex three-functional-layer sample. Notably, the transmittance for this sample around a wavelength of $1.44\,\mu$m, where a negative real part of the refractive index occurs (see below), is as large as 60%. Note that we have used a strictly identical parameter set for the three cases $N = 1, 2, 3$ in our calculations, i.e., identical $w_x, w_x, a_x, a_y, \alpha, s, t, e_x, e_y$ as well as identical optical parameters and identical Drude parameters. Thus, the following retrieval based on the same theory and parameters, can be considered as very trustworthy.

We again retrieve the effective optical parameters as usual. We take the physical thickness of our metamaterial stacks ($d = 83, 135, 187\,$nm for $N = 1, 2, 3$, respectively) on the glass substrate in the retrieval. Figure 6.23 shows that the shape of the retrieved real part of the complex refractive index hardly changes with the number of functional layers N for

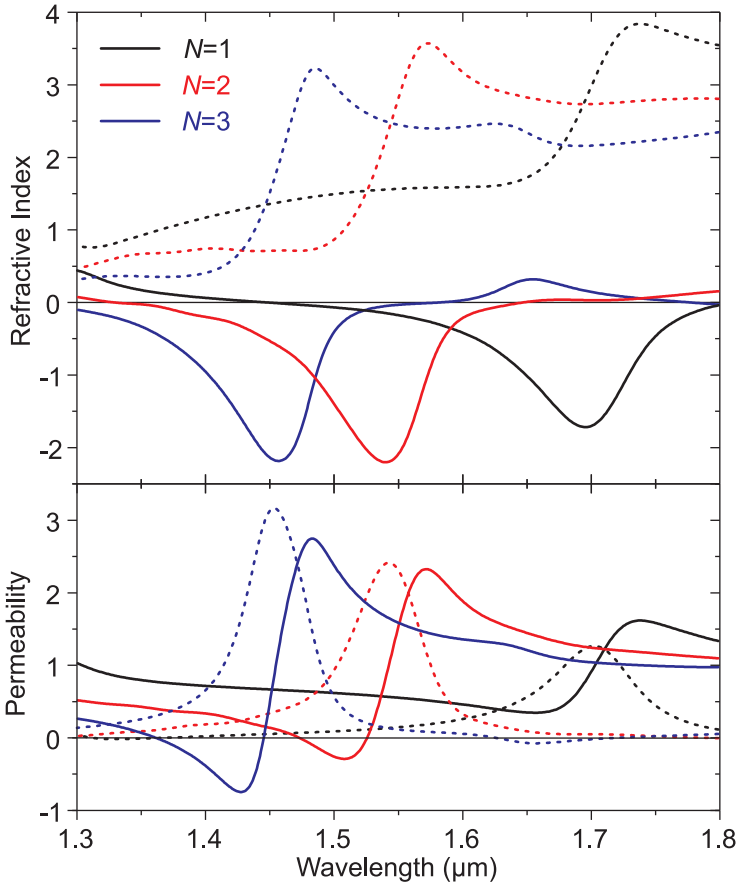

Figure 6.23: Effective refractive index n (top) and magnetic permeability μ (bottom) retrieved from the calculated complex transmittance and reflectance spectra for the same parameters as in Fig. 6.22; horizontal incident polarization. Real parts are solid, imaginary parts are dashed. The number of functional layers N is indicated.

$N = 1, 2, 3$. The negative real part of n for $N = 2, 3$ results from the combination of a negative real part of the electric permittivity ε (not shown) and a negative real part of the magnetic permeability μ. The increase of the FOM with N towards a maximum of FOM ≈ 2.5 at a wavelength of $1.41\,\mu$m should not be taken too seriously, as the detailed behavior depends on the value of N the response has been optimized for. In this case we have optimized it for $N = 3$. The blueshift of the resonance with increasing N simply results from the trapezoidal shape, i.e., from the finite angle α (see Fig. 6.18), which directly influences the magnetic resonance frequency. One might have expected three magnetic resonances at three different spectral positions for $N = 3$ or a huge inhomogeneous broadening – if the three functional layers were independent. The numerical calculations clearly show that this behavior does not occur. The magnetic dipole moment of one functional layer stems from the antisymmetric current oscillation in the two metal layers surrounding one dielectric spacer. Thus one might have naively expected that the magnetic-dipole moments of adjacent functional layers would cancel to some extent. However, the numerical calculations show that this behavior does not occur either. This conclusion is not surprising in view of the sub-wavelength distance of the functional layers that introduces a strong coupling *via* the light field. Furthermore, adjacent

functional layers share one common metal layer. These two aspects lead to a cooperative behavior that is very favorable for performance. In particular, it makes the structure robust against varying individual resonance frequencies, i.e., robust against fabrication tolerances.

However, it is currently not quite clear whether the mentioned cooperative effects will prevail for structures that are many wavelengths in thickness. While our results are a first step towards three-dimensional photonic metamaterials, it should be clear that it is still a long way to study truly three-dimensional isotropic negative-index metamaterials at optical frequencies.

Chapter 7

Conclusions

In this thesis, we have investigated the linear-optical properties of negative-index metamaterials at optical and visible frequencies in both experiment and theory. Metamaterials offer the possibility to manipulate both the electric and the magnetic field of the incoming light. This gives rise to astonishing phenomena such as a negative refractive index.

Metamaterials consist of responsive building blocks smaller than the relevant wavelength of light. Thus, the light wave "sees" an effective medium which can be characterized by an effective electric permittivity ε and an effective magnetic permeability μ. From these two quantities a refractive index n can be deduced. In the experiments, we have employed the double-fishnet metamaterial which can be viewed as composed of (i) "electric atoms" leading to $\varepsilon < 0$ and (ii) "magnetic atoms" leading to $\mu < 0$: (i) The electric atoms are represented by thin and long metal wires parallel to the incident electric field vector. Their behavior is that of a diluted metal with a plasma frequency lower than that of the bulk metal. (ii) The resonance wavelength of the magnetic atoms is determined by the length of double wires or plates in the direction of the incident electric field vector. The magnetic dipole moment stems from the anti-symmetric current eigenmode of the two coupled metal layers, each of which can be viewed as a half-wavelength antenna. Above the magnetic eigenfrequency, the magnetic permeability can be negative. By combining these two sorts of atoms, it is possible to obtain a negative permittivity and a negative permeability in a certain frequency interval. Furthermore, a negative refractive index is achievable.

Before dealing with experiments, we have explored the physics of the refractive index and the phenomenon of refraction. With a ray tracing program like POV-Ray, for example, one can simulate the behavior of isotropic materials with a certain refractive index n, and in the case of $n < 0$ one observes rays which are refracted to the "wrong side". As a consequence, simple scenes such as a drinking glass filled with a liquid get rather complicated if the liquid has $n < 0$: Objects appear as if ripped, one can look around corners, and many more unusual effects can be observed. Hence, it is common to relate the refractive index to the phenomenon of refraction at an interface. Yet, we have shown that – in general – the refractive index merely describes the velocity of the front of constant phase of a wave in a medium with respect to vacuum. In order to emphasize this aspect, we have presented examples exhibiting negative refraction although only positive refractive indices occur. For

an anisotropic material like calcite, for instance, one can get both negative and positive refraction, depending on the angle of incidence. Furthermore, also with metals and even with isotropic and homogenous thin dielectric films, negative refraction can occur. The physics of negative refraction is based on the behavior of the Poynting vector at the interface since the Poynting vector describes the direction of the energy flow. The Poynting vector, however, is not directly related to the refractive index, and thus negative refraction is not necessarily related to a negative refractive index.

Before actually fabricating metamaterials, we have always optimized the structures by different simulation techniques for efficiency and comparison. From the numerical calculations the effective material parameters, i.e., the permeability, the permittivity, and the refractive index have been deduced. For the double-fishnet design, for instance, we have studied the effects of the shape of the holes on the refractive index, and the losses. We have shown that rectangular holes are better in terms of lower losses than circular holes at wavelengths around 1.5 µm.

All our metamaterial samples have been fabricated by standard electron-beam lithography. During this process, a photoresist is patterned, to serve as a mask in a subsequent evaporation process in which different metals and/or dielectrics have been deposited onto the sample substrate. Electron-beam lithography offers the possibility to fabricate high-quality structures on a nanometer scale. This high-precision technique is essential since our responsive building blocks have to be smaller than the relevant wavelength – for visible light, the artificial atoms already have to be smaller than a few hundreds of nanometers. Electron-beam evaporation of the constituent materials of our metamaterials is inevitable as we need high-quality films.

In order to measure a negative refractive index and hence a negative phase velocity we have built a Michelson interferometer setup. We have employed 170-fs optical pulses around 1.5 µm wavelength, or 125-fs pulses around 800 nm wavelength, depending on the operation wavelength of the metamaterials. Hence, it has been possible to measure both the phase velocity and the group velocity inside our metamaterial. We have demonstrated a negative phase velocity in a metamaterial around 1.5 µm wavelength. Furthermore, we have found a spectral range in which the group velocity is negative, i.e., the maximum of the output pulse envelope leaves the metamaterial before the maximum of the corresponding input pulse envelope enters the metamaterial. However, this aspect is not in conflict with causality since pulse reshaping in the sample is of crucial importance. In our experiment we have also found a spectral interval in which both the phase velocity and the group velocity are negative simultaneously. This behavior has been observed experimentally for the first time at optical frequencies.

In the next generation of samples, we have employed silver instead of gold as the constituent metal in our metamaterials. Silver has the advantage of lower losses compared to gold. We have carefully optimized a structure to exhibit a large figure of merit (FOM), i.e., the negative ratio of real part to imaginary part of the refractive index: $\mathrm{FOM} = -\mathrm{Re}(n)/\mathrm{Im}(n)$. Recent metamaterials operating at optical wavelengths had shown values of $\mathrm{FOM} < 1$, i.e., the imaginary part of the refractive index has dominated the corresponding real part. We have achieved to fabricate a metamaterial with a $\mathrm{FOM} \approx 3$. This is 30

times larger than the value obtained in the first negative-index metamaterial at optical wavelengths. Our large FOM is also related to our almost transparent metamaterial – more than 60% transmission in the spectral range where $\mathrm{Re}(n) < 0$.

We have further studied the interaction between different unit cells of our metamaterials. In the above discussions, the optical properties of the metamaterials are the result of the optical properties of the individual atoms. Going one step further, the electric dipole-dipole and magnetic dipole-dipole interactions between next-nearest neighbors (and beyond) lead to a coupling of the photonic atoms. In order to clarify the interactions, we have measured transmittance spectra under oblique incidence of light. This procedure allows to infer the in-plane dispersion relation. We have found that the magnetic and the electric interactions strongly depend on the in-plane wave vector. From the geometry and the dispersion shape, we have concluded that the coupling is predominantly driven *via* magnetic dipoles for the wave propagation along the magnetic-dipole direction. These magnetization waves are the classical analogue of magnon excitations of quantum-mechanical spins. If the electric atoms are completely eliminated in calculations, transmittance spectra show hardly any influence on the in-plane wave vector. This observation indicates that the electric atoms mediate both the above-mentioned strong electric and magnetic dipole-dipole couplings. Furthermore, it also unambiguously reveals that changes in the spectra are not a property of the isolated magnetic atoms alone.

In order to obtain a negative refractive index in the visible spectrum of light, we have further miniaturized the respective building blocks of our metamaterial. The corresponding sample shows a $68\,\mathrm{nm}$ minimum lateral feature size at $97\,\mathrm{nm}$ thickness of the metamaterial. This aspect ratio exceeding unity already poses significant fabrication challenges. By comparing transmittance, reflectance, and phase-sensitive time-of-flight experiments with theory, we have inferred a real part of the refractive index of $\mathrm{Re}(n) = -0.6$ at $780\,\mathrm{nm}$ wavelength – which is visible in the laboratory – with a $\mathrm{FOM} \approx 0.5$. This metamaterial has been the first to show a negative refractive index in the visible.

All studies and previous discussions on negative-index metamaterials at optical wavelengths are based on single functional layers only. However, it is well known, for instance from electronic crystals, that the surface or a monolayer can exhibit properties that are rather different from the bulk. Thus, we have investigated whether the optical properties of a single layer of a negative-index metamaterial correspond to those of many layers. We have fabricated corresponding samples with one, two, and three functional layers. For all three samples we have obtained a negative refractive index at optical wavelengths and, e.g., for the three-functional-layer sample we have observed a transmittance exceeding 60% at a wavelength of $1.44\,\mu\mathrm{m}$, at which a negative real part of the refractive index has been obtained. We have shown that the optical properties of the different samples almost do not change with the numbers of layers. The experimental data has been well reproduced by corresponding numerical calculations.

Broadly speaking, photonic metamaterials offer the possibility to obtain optical properties which do not occur in natural substances. In this thesis, we have realized a negative refractive index at optical and even visible frequencies and have investigated new effects. However, we have only fabricated metamaterials which are mostly limited to two-dimensional

structures. Yet, the aim is to realize truly three-dimensional, isotropic, negative-index metamaterials at optical frequencies. This is still a long way, while first steps are made. The field of optics & photonics has already changed considerably by the enlarged possibilities offered by photonic metamaterials. Further exciting discoveries are to be expected.

Appendix A

Transfer-matrix method for oblique incidence of light

We study the behavior of a plane wave impinging on slab with refractive index n_{II} and thickness d [15]. The figure displays the case of s-polarization. The important fact is that each wave $E_{\mathrm{rI}}, E_{\mathrm{r'I}}, \ldots$ represents the resulting wave of all possible waves emerging from each point of the medium and propagating in all directions. Consequently, the summation is already included. From Maxwell's equation one obtains that at the interface the tangential components of $\boldsymbol{E}$ and $\boldsymbol{H}$ as well as the normal components of $\boldsymbol{D}$ and $\boldsymbol{B}$ are conserved. First, we deal with s-polarized light. At the interface from medium I to II the following holds:

$$\begin{aligned} E_{\mathrm{I}} &= E_{\mathrm{iI}} + E_{\mathrm{rI}} = E_{\mathrm{tII}} + E_{\mathrm{r'II}}, && \text{(A.1)} \\ H_{\mathrm{I}} &= (H_{\mathrm{iI}} - H_{\mathrm{rI}})\cos(\alpha_{\mathrm{I}}) = (H_{\mathrm{tII}} - H_{\mathrm{r'II}})\cos(\alpha_{\mathrm{II}}), && \text{(A.2)} \\ &= (E_{\mathrm{iI}} - E_{\mathrm{rI}})Z_{\mathrm{I}}^{-1}\cos(\alpha_{\mathrm{I}}) = (E_{\mathrm{tII}} - E_{\mathrm{r'II}})Z_{\mathrm{II}}^{-1}\cos(\alpha_{\mathrm{II}}). && \text{(A.3)} \end{aligned}$$

Here, we have used the relation

$$\boldsymbol{H} = Z^{-1}\hat{\boldsymbol{k}} \times \boldsymbol{E}, \tag{A.4}$$

with the impedance $Z = \sqrt{\frac{\mu_0\mu}{\varepsilon_0\varepsilon}}$ and the unit wave vector $\hat{\boldsymbol{k}}$. Analogously, at the interface of medium II to III one has:

$$\begin{aligned} E_{\mathrm{II}} &= E_{\mathrm{iII}} + E_{\mathrm{rII}} = E_{\mathrm{tIII}}, && \text{(A.5)} \\ H_{\mathrm{II}} &= (E_{\mathrm{iII}} - E_{\mathrm{rII}})Z_{\mathrm{II}}^{-1}\cos(\alpha_{\mathrm{II}}) = E_{\mathrm{tIII}}Z_{\mathrm{III}}^{-1}\cos(\alpha_{\mathrm{III}}). && \text{(A.6)} \end{aligned}$$

Between both interfaces the plane wave propagates and accumulates the phase delay of $k'd = k_0 n_{\mathrm{II}}\cos(\alpha_{\mathrm{II}})d$. Thus, we obtain:

$$\begin{aligned} E_{\mathrm{iII}} &= E_{\mathrm{tII}}e^{\mathrm{i}k'd}, && \text{(A.7)} \\ E_{\mathrm{rII}} &= E_{\mathrm{r'II}}e^{-\mathrm{i}k'd}. && \text{(A.8)} \end{aligned}$$

Than, we can rewrite the equations (A.5) and (A.6):

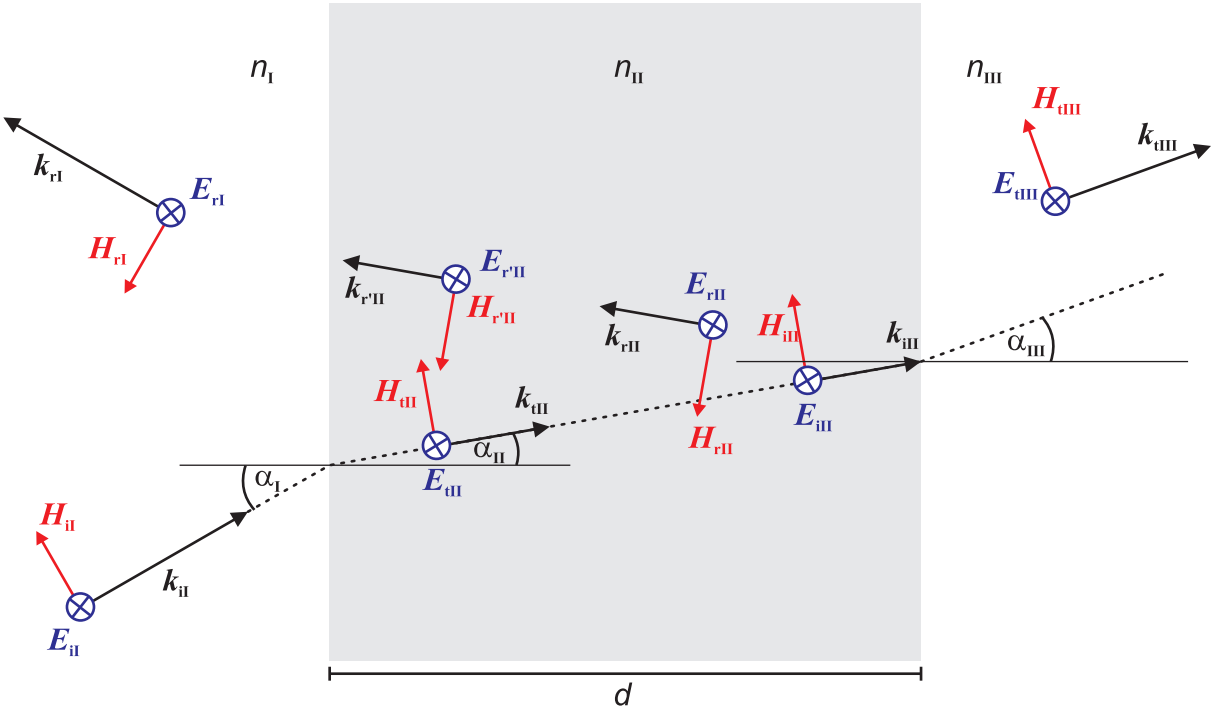

Figure A.1: A s-polarized electromagnetic wave impinges from a medium with refractive index n_{I} on a slab with refractive index n_{II} and thickness d.

$$E_{\mathrm{II}} = E_{\mathrm{tII}}e^{\mathrm{i}k'd} + E_{\mathrm{r'II}}e^{-\mathrm{i}k'd}, \tag{A.9}$$

$$H_{\mathrm{II}} = \left(E_{\mathrm{tII}}e^{\mathrm{i}k'd} - E_{\mathrm{r'II}}e^{-\mathrm{i}k'd}\right) Z_{\mathrm{II}}^{-1}\cos(\alpha_{\mathrm{II}}). \tag{A.10}$$

Using equations (A.1) and (A.3) we get

$$E_{\mathrm{I}} = E_{\mathrm{II}}\cos(k'd) - H_{\mathrm{II}}\mathrm{i}\sin(k'd)/\gamma_{\mathrm{II}}, \tag{A.11}$$

$$H_{\mathrm{I}} = -E_{\mathrm{II}}\gamma_{\mathrm{II}}\mathrm{i}\sin(k'd) + H_{\mathrm{II}}\cos(k'd), \tag{A.12}$$

with

$$\gamma_{\mathrm{II}} = Z_{\mathrm{II}}^{-1}\cos(\alpha_{\mathrm{II}}). \tag{A.13}$$

In the case of p-polarized light, the calculations are performed analogously. The mere difference, one obtains at the end, is:

$$\gamma_{\mathrm{II}} = \left(Z_{\mathrm{II}}\cos(\alpha_{\mathrm{II}})\right)^{-1}. \tag{A.14}$$

Thus, in the matrix notation one gets:

$$\begin{pmatrix} E_{\mathrm{I}} \\ H_{\mathrm{I}} \end{pmatrix} = M_{\mathrm{II}} \begin{pmatrix} E_{\mathrm{II}} \\ H_{\mathrm{II}} \end{pmatrix} \tag{A.15}$$

$$= \begin{pmatrix} \cos(k'd) & -\mathrm{i}\sin(k'd)/\gamma_{\mathrm{II}} \\ -\gamma_{\mathrm{II}}\mathrm{i}\sin(k'd) & \cos(k'd) \end{pmatrix} \begin{pmatrix} E_{\mathrm{II}} \\ H_{\mathrm{II}} \end{pmatrix}. \tag{A.16}$$

In order to calculate the characteristics of a plane wave impinging on more than one layer, the corresponding matrices are simply multiplied:

$$M = M_{\mathrm{II}} M_{\mathrm{III}} M_{\mathrm{IV}} \ldots = \begin{pmatrix} m_{11} & m_{12} \\ m_{21} & m_{22} \end{pmatrix}. \tag{A.17}$$

Rewriting equation (A.16), we obtain for the layer shown above in the case of s-polarized light:

$$\begin{pmatrix} E_{\mathrm{iI}} + E_{\mathrm{rI}} \\ (E_{\mathrm{iI}} - E_{\mathrm{rI}})\gamma_{\mathrm{I}} \end{pmatrix} = M_{\mathrm{II}} \begin{pmatrix} E_{\mathrm{tIII}} \\ E_{\mathrm{tIII}}\gamma_{\mathrm{III}} \end{pmatrix}. \tag{A.18}$$

The resulting amplitude transmission coefficients t and amplitude reflection coefficients r are defined as

$$t = \frac{E_{\mathrm{tIII}}}{E_{\mathrm{iI}}}, \tag{A.19}$$

$$r = \frac{E_{\mathrm{rI}}}{E_{\mathrm{iI}}}. \tag{A.20}$$

Thus, we obtain for the amplitude transmission coefficients for s- and p-polarized light:

$$t_{\mathrm{s}} = \frac{2\gamma_{\mathrm{I}}}{\gamma_{\mathrm{I}} m_{11} + \gamma_{\mathrm{I}}\gamma_{\mathrm{III}} m_{12} + m_{21} + \gamma_{\mathrm{III}} m_{22}}, \tag{A.21}$$

$$t_{\mathrm{p}} = \frac{Z_{\mathrm{III}}}{Z_{\mathrm{I}}} \frac{2\gamma_{\mathrm{III}}}{\gamma_{\mathrm{I}} m_{11} + \gamma_{\mathrm{I}}\gamma_{\mathrm{III}} m_{12} + m_{21} + \gamma_{\mathrm{III}} m_{22}}, \tag{A.22}$$

Here, the index indicates the corresponding polarization. In the case of $\alpha_{\mathrm{I}} = 0$, t_{s} equals t_{p}.

Bibliography

[1] V. G. Veselago, *The Electrodynamics of Substances with Simultaneously Negative Values of ϵ and μ*, Sov. Phys. Usp. **10**, 509 (1968).

[2] J. B. Pendry, A. J. Holden, D. J. Robbins, and W. J. Stewart, *Magnetism from conductors and enhanced nonlinear phenomena*, IEEE Trans. MTT **47**, 2075 (1999).

[3] R. A. Shelby, D. R. Smith, and S. Schultz, *Experimental Verifcation of a Negative Index of Refraction*, Science **292**, 77 (2001).

[4] J. B. Pendry, *Negative Refraction Makes a Perfect Lens*, Phys. Rev. Lett. **85**, 3966 (2000).

[5] N. Fang, H. Lee, C. Sun, and X. Zhang, *Sub–Diffraction-Limited Optical Imaging with a Silver Superlens*, Science **308**, 534 (2005).

[6] J. B. Pendry, D. Schurig, and D. R. Smith, *Controlling Electromagnetic Fields*, Science **312**, 1780 (2006).

[7] U. Leonhardt, *Optical Conformal Mapping*, Science **312**, 1777 (2006).

[8] D. Schurig, J. J. Mock, B. J. Justice, S. A. Cummer, J. B. Pendry, A. F. Starr, and D. R. Smith, *Metamaterial Electromagnetic Cloak at Microwave Frequencies*, Science **314**, 977 (2006).

[9] I. V. Shadrivov, A. A. Sukhorukov, and Y. S. Kivshar, *Complete Band Gaps in One-Dimensional Left-Handed Periodic Structures*, Phys. Rev. Lett. **95**, 193903 (2005).

[10] Y. Yuan, L. Ran, J. Huangfu, H. Chen, L. Shen, and J. A. Kong, *Experimental verification of zero order bandgap in a layered stack of left-handed and right-handed materials*, Opt. Express **14**, 2220 (2006).

[11] D. R. Smith, J. B. Pendry, and M. C. K. Wiltshire, *Metamaterials and Negative Refractive Index*, Science **305**, 788 (2004).

[12] T. J. Yen, W. J. Padilla, N. Fang, D. C. Vier, D. R. Smith, J. B. Pendry, D. N. Basov, and X. Zhang, *Terahertz Magnetic Response from Artificial Materials*, Science **303**, 1494 (2004).

[13] S. Linden, C. Enkrich, M. Wegener, J. F. Zhou, T. Koschny, and C. M. Soukoulis, *Magnetic Response of Metamaterials at 100 Terahertz*, Science **306**, 1351 (2004).

[14] G. Dolling, M. Wegener, C. M. Soukoulis, and S. Linden, *Negative-index metamaterial at 780 nm wavelength*, Opt. Lett. **32**, 53 (2007).

[15] E. Hecht, *Optik* (Oldenbourg Verlag, 2001).

[16] J. D. Jackson, *Classical Electrodynamics - Third Edition* (Wiley, 1998).

[17] J. Kästel and M. Fleischhauer, *Quantum Electrodynamics in Media with Negative Refraction*, Laser Physics **15**, 1 (2005).

[18] D. R. Smith and N. Kroll, *Negative Refractive Index in Left-Handed Materials*, Phys. Rev. Lett. **85**, 2933 (2000).

[19] Povray, *http://www.povray.org*.

[20] V. A. Podolskiy and E. E. Narimanov, *Near-sighted superlens*, Opt. Lett. **30**, 75 (2005).

[21] R. Merlin, *Analytical solution of the almost-perfect-lens problem*, Appl. Phys. Lett. **84**, 1290 (2004).

[22] S. Durant, Z. Liu, J. M. Steele, and X. Zhang, *Theory of the transmission properties of an optical far-field superlens for imaging beyond the diffraction limit*, J. Opt. Soc. Am. B **23**, 2383 (2006).

[23] P. B. Johnson and R. W. Christy, *Optical Constants of the Noble Metals*, Phys. Rev. B **6**, 4370 (1972).

[24] J. B. Pendry, A. J. Holden, W. J. Stewart, and I. Youngs, *Extreme Low Frequency Plasmons in Metallic Mesostructures*, Phys. Rev. Lett. **76**, 4773 (1996).

[25] G. Mie, *Beiträge zur Optik trüber Medien, speziell kolloidaler Metallösungen*, Ann. Phys. **25**, 377 (1908).

[26] U. Kreibig and M. Vollmer, *Optical Properties of Metal Clusters* (Springer Verlag, 1995).

[27] J. D. Joannopoulos, R. D. Meade, and J. N. Winn, *Photonic Crystals* (Princeton University Press, 1995).

[28] G. D. Malyuzhinets, *A note on the radiation principle*, Zhurnal Technicheskoi Fiziki **21**, 940 (1951).

[29] N. Engheta, A. Salandrino, and A. Alu, *Circuit Elements at Optical Frequencies: Nanoinductors, Nanocapacitors, and Nanoresistors*, Phys. Rev. Lett. **95**, 095504 (2005).

[30] C. Caloz and T. Itoh, *Electromagnetic Metamaterials: Transmission Line Theory and Microwave Applications* (Wiley-IEEE Press, 2005).

[31] W. N. Hardy and L. A. Whitehead, *Split-ring resonator for use in magnetic resonance from 200-2000 MHz*, Rev. Sci. Instrum. **52**, 213 (1981).

[32] H. J. Schneider and P. Dullenkopf, *Slotted tube resonator: A new NMR probe head at high observing frequencies*, Rev. Sci. Instrum. **48**, 68 (1977).

[33] S. A. Schelkunoff and H. T. Friis, *Antennas: Theory and Practice* (Wiley, 1952).

[34] A. N. Lagarkov and A. K. Sarychev, *Optomagnetic composite medium with conducting nanoelements*, Phys. Rev. B **53**, 6318 (1996).

[35] L. V. Panina, A. N. Grigorenko, and D. P. Makhnovskiy, *Optomagnetic composite medium with conducting nanoelements*, Phys. Rev. B **66**, 155411 (2002).

[36] V. A. Podolskiy, A. K. Sarychev, E. E. Narimanov, and V. M. Shalaev, *Resonant light interaction with plasmonic nanowire systems*, J. Opt. A: Pure Appl. Opt. **7**, 32 (2005).

[37] S. Zhang, W. Fan, N. C. Panoiu, K. J. Malloy, R. M. Osgood, and S. R. J. Brueck, *Experimental Demonstration of Near-Infrared Negative-Index Metamaterials*, Phys. Rev. Lett. **95**, 137404 (2005).

[38] S. Zhang, W. Fan, K. J. Malloy, S. R. J. Brueck, N. C. Panoiu, and R. M. Osgood, *Near-infrared double negative metamaterials*, Opt. Express **13**, 4922 (2005).

[39] J. F. Zhou, L. Zhang, G. Tuttle, T. Koschny, and C. M. Soukoulis, *Negative index materials using simple short wire pairs*, Phys. Rev. B **73**, 041101 (2006).

[40] W. J. Padilla, D. R. Smith, and D. N. Basov, *Spectroscopy of metamaterials from infrared to optical frequencies*, J. Opt. Soc. Am. B **23**, 404 (2006).

[41] C. Enkrich, *Magnetic Metamaterials for Photonics*, Ph.D. thesis, Universität Karlsruhe (TH) (2006).

[42] S. Linden, C. Enkrich, G. Dolling, M. W. Klein, J. Zhou, Th. Koschny, C. M. Soukoulis, S. Burger, F. Schmidt, and M. Wegener, *Photonic metamaterials: Magnetism at optical frequencies*, IEEE J. Sel. Top. Quant **12**, 1097 (2006).

[43] V. G. Veselago and E. E. Narimanov, *The left hand of brightness: past, present and future of negative index materials*, Nature Mater. **5**, 759 (2006).

[44] C. M. Soukoulis, S. Linden, and M. Wegener, *Negative Refractive Index at Optical Wavelengths*, Science **315**, 47 (2007).

[45] V. M. Shalaev, *Optical negative-index metamaterials*, Nature Phot. **1**, 41 (2007).

[46] R. W. Wood, *On a remarkable case of uneven distribution of light in a diffraction grating spectrum*, Phylos. Mag. **4**, 396 (1902).

[47] L. Rayleigh, *On the dynamical theory of gratings*, Proc. Roy. Soc. (London) **A79**, 399 (1907).

[48] K. Busch, G. von Freymann, S. Linden, S. Mingaleev, L. Tkeshelashvili, and M. Wegener, *Periodic nanostructures for photonics*, Phys. Rep. , in press (2007).

[49] H. Luo, W. Hu, X. Yi, H. Liu, and J. Zhu, *Amphoteric refraction at the interface between isotropic and anisotropic media*, Opt. Commun. **254**, 353 (2005).

[50] Y. Zhang, B. Fluegel, and A. Mascarenhas, *Total Negative Refraction in Real Crystals for Ballistic Electrons and Light*, Phys. Rev. Lett. **91**, 157404 (2003).

[51] P. Bliokh and J. Felsteiner, *Comment on "Total Negative Refraction in Crystals for Ballistic Electrons and Light"*, arXiv:physics/0311066 (2003).

[52] H.-F. Yau, J.-P. Liu, B. Ke C.-H. Kuo, and Z. Ye, *Comment on "Total Negative Refraction in Real Crystals for Ballistic Electrons and Light" (Phys. Rev. Lett. 91, 157404 (2003))*, arXiv:cond-mat/0312125 (2003).

[53] I. Biaggio, *Does Optical Anisotropy Lead to Negative Refraction at an Interface?*, arXiv:cond-mat/0502308 (2003).

[54] P. St. J. Russell, *Interference of integrated Floquet-Bloch waves*, Phys. Rev. A **33**, 3232 (1986).

[55] R. Zengerle, *Light propagation in singly and doubly periodic planar waveguides*, J. Mod. Opt. **34**, 1589 (1987).

[56] H. M. Lai, C. W. Kwok, Y. W. Loo, and B. Y. Xu, *Energy-flux pattern in the Goos-Hänchen effect*, Phys. Rev. E **62**, 7330 (2000).

[57] P. Tournois and V. Laude, *Negative group velocities in metal-film optical waveguides*, Opt. Commun. **137**, 41 (1997).

[58] H. Shin and S. Fan, *All-Angle Negative Refraction for Surface Plasmon Waves Using a Metal-Dielectric-Metal Structure*, Phys. Rev. Lett. **96**, 073907 (2006).

[59] H. J. Lezec, J. A. Dionne, and H. A. Atwater, *Negative Refraction at Visible Frequencies*, Science **316**, 430 (2007).

[60] Zentrum Mikroskopie der Universität Basel, .

[61] M. Knoll and E. Ruska, *Das Elektronenmikroskop*, Z. f. Physik **78**, 318 (1932).

[62] V. K. Zworykin, J. Hiller, and R. L. Snyder, *A scanning electron microscope*, ASTM Bull. **117**, 15 (1942).

[63] P. W. Hawkes and E. Kasper, *Principles of Electron Optics* (Academic Press, London, 1989).

[64] P. Grivet, *Electron Optics* (Pergamon Press, Oxford, 1965).

[65] L. Reimer and G. Pfefferkorn, *Raster - Elektronenmikroskopie* (Springer, 1999).

[66] H. Boersch, *Experimentelle Bestimmung der Energieverteilung in Thermisch Ausgelösten Elektronenstrahlen*, Z. Phys. **139**, 115 (1954).

[67] R. F. M. Thornley and M. Hatzakis, *Electron Optical Fabrication of Solid State Devices*, Record of 9th Symp. on Electron, Ion and Laser Beam Tech. , 94 (1967).

[68] N. Feth, *Herstellung metalischer Metamaterialien mittels holographischer Laserlithographie und deren Charakterisierung*, Diplomarbeit, Universität Karlsruhe (TH) (2006).

[69] M. Deubel, *Three-Dimensional Photonic Crystals via Direct Laser Writing: Fabrication and Characterization*, Ph.D. thesis, Universität Karlsruhe (TH) (2006).

[70] K. S. Yee, *Numerical Solution of Initial Boundary Value Problems Involving Maxwell's Equations in Isotropic Media*, IEEE Trans. Antenna Propagation **14**, 302 (1966).

[71] S. Burger, R. Klose, A. Schädle, F. Schmidt, and L. Zschiedrich, *FEM modeling of 3D photonic crystals and photonic crystal waveguides*, Proc. SPIE **5728**, 164 (2005).

[72] L. Zschiedrich, R. Klose, A. Schädle, and F. Schmidt, *A new finite element realization of the perfectly matched layer method for Helmholtz scattering problems on polygonal domains in two dimensions*, J. Comput Appl. Math. **188**, 12 (2006).

[73] L. Zschiedrich, S. Burger, B. Kettner, and F. Schmidt, *Advanced finite element method for nano-resonators*, Proc. SPIE **6115**, 611515 (2006).

[74] D. R. Smith, S. Schultz, P. Markos, and C. M. Soukoulis, *Determination of effective permittivity and permeability of metamaterials from reflection and transmission coefficients*, Phys. Rev. B **65**, 195104 (2002).

[75] M. I. Stockman, *Criterion for Negative Refraction with Low Optical Losses from a Fundamental Principle of Causality*, Phys. Rev. Lett. **98**, 177404 (2007).

[76] M. W. Klein, C. Enkrich, M. Wegener, C. M. Soukoulis, and S. Linden, *Single-slit split-ring resonators at optical frequencies: limits of size scaling*, Opt. Lett. **31**, 1259 (2006).

[77] V. M. Shalaev, W. Cai, U. K. Chettiar, H. K. Yuan, A. K. Sarychev, V. P. Drachev, and A. V. Kildishev, *Negative index of refraction in optical metamaterials*, Opt. Lett. **30**, 3356 (2005).

[78] G. Dolling, C. Enkrich, M. Wegener, J. Zhou, C. M. Soukoulis, and S. Linden, *Cut-wire pairs and plate pairs as magnetic atoms for optical metamaterials*, Opt. Lett. **30**, 3198 (2005).

[79] G. Dolling, *Herstellung und Charakterisierung von magnetodielektrischen Metamaterialien*, Diplomarbeit, Universität Karlsruhe (TH) (2006).

[80] Z. Ku and S. R. J. Brueck, *Comparison of negative refractive index materials with circular, elliptical and rectangular holes*, Opt. Express **15**, 4515 (2007).

[81] M. Wegener, *Extreme Nonlinear Optics* (Springer, 2005).

[82] C. G. B. Garrett and D. E. McCumber, *Propagation of a Gaussian Light Pulse through an Anomalous Dispersion Medium*, Phys. Rev. A **1**, 305 (1970).

[83] L. Brillouin, *Wave Propagation and Group Velocity* (Academic, 1960).

[84] S. Chu and S. Wong, *Linear Pulse Propagation in an Absorbing Medium*, Phys. Rev. Lett. **48**, 738 (1982).

[85] L. J. Wang, A. Kuzmich, and A. Dogariu, *Gain-assisted superluminal light propagation*, Nature **406**, 277 (2000).

[86] M. D. Stenner, D. J. Gauthier, and M. A. Neifeld, *The speed of information in a 'fast-light' optical medium*, Nature **425**, 695 (2003).

[87] M. S. Bigelow, N. N. Lepeshkin, and R. W. Boyd, *Superluminal and Slow Light Propagation in a Room-Temperature Solid*, Science **301**, 200 (2003).

[88] A. Sommerfeld, *Über die Fortpflanzung des Lichtes in dispergierenden Medien*, Ann. Phys. **44**, 177 (1914).

[89] L. Brillouin, *Über die Fortpflanzung des Lichtes in dispergierenden Medien*, Ann. Phys. **44**, 203 (1914).

[90] H. Jeong, A. M. C. Dawes, and D. J. Gauthier, *Direct Observation of Optical Precursors in a Region of Anomalous Dispersion*, Phys. Rev. Lett. **96**, 143901 (2006).

[91] D. J. Gauthier and R. W. Boyd, *Fast Light, Slow Light and Optical Precursors: What Does It All Mean?*, Photonics Spectra , Jan. 82 (2007).

[92] O. F. Siddiqui, S. J. Erickson, G. V. Eleftheriades, and M. Mojahedi, *Time-Domain Measurement of Negative Group Delay in Negative-Refractive-Index Transmission-Line Metamaterials*, IEEE Trans. Microw. Theory Tech. **52**, 1449 (2004).

[93] O. F. Siddiqui, M. Mojahedi, and G. V. Eleftheriades, *Periodically Loaded Transmission Line with Effective Negative Refractive Index and Negative Group Velocity*, IEEE Trans. Antenna Propagation. **51**, 2619 (2003).

[94] J. F. Woodley and M. Mojahedi, *Negative Group Velocity and Group Delay in Left-Handed Media*, Phys. Rev. E **70**, 046603 (2004).

[95] M. Mojahedi, K. J. Malloy, G. V. Eleftheriades, J. F. Woodley, and R. Y. Chiao, *Abnormal Wave Propagation in Passive Media*, IEEE J. Sel. Top. Quant **1**, 30 (2003).

[96] G. Dolling, C. Enkrich, M. Wegener, C. M. Soukoulis, and S. Linden, *Simultaneous Negative Phase and Group Velocity of Light in a Metamaterial*, Science **312**, 892 (2006).

[97] S. Zhang, W. Fan, N. C. Panoiu, K. J. Malloy, R. M. Osgood, and S. R. J. Brueck, *Experimental Demonstration of Near-Infrared Negative-Index Metamaterials*, Phys. Rev. **95**, 137404 (2005).

[98] S. Zhang, W. Fan, K. J. Malloy, S. R. J. Brueck, N. C. Panoiu, and R. M. Osgood, *Demonstration of metal-dielectric negative-index metamaterials with improved performance at optical frequencies*, J. Opt. Soc. Am. B **23**, 434 (2006).

[99] G. Dolling, C. Enkrich, M. Wegener, C. M. Soukoulis, and S. Linden, *Low-loss negative-index metamaterial at telecommunication wavelengths*, Opt. Lett. **31**, 1800 (2006).

[100] A. N. Grigorenko, A. K. Geim, H. F. Gleeson, Y. Zhang, A. A. Firsov, I. Y. Khrushchev, and J. Petrovic, *Nanofabricated media with negative permeability at visible frequencies*, Nature **438**, 335 (2005).

[101] A. V. Kildishev, V. P. Drachev, U. K. Chettiar, D. Werner, D. Kwon, and V. M. Shalaev, *Comment on "Negative Refractive Index in Artificial Metamaterials" [A. N. Grigorenko, Opt. Lett., 31, 2483 (2006)]*, arXiv:physics/0609234 (2006).

[102] G. Dolling, M. Wegener, A. Schädle, S. Burger, and S. Linden, *Observation of magnetization waves in negative-index photonic metamaterials*, Appl. Phys. Lett. **89**, 231118 (2006).

[103] M. L. Brongersma, J. W. Hartman, and H. A. Atwater, *Electromagnetic energy transfer and switching in nanoparticle chain arrays below the diffraction limit*, Phys. Rev. B **62**, R16356 (2000).

[104] E. Shamonina and L. Solymar, *Properties of magnetically coupled metamaterial elements*, J. Magn. Magn. Mater. **300**, 38 (2006).

[105] M. C. K. Wiltshire, E. Shamonina, I. R. Young, and L. Solyma, *Dispersion characteristics of magneto-inductive waves: comparison between theory and experiment*, Electron. Lett. **39**, 215 (2003).

[106] H. Liu, D. A. Genov, D. M. Wu, Y. M. Liu, J. M. Steele, C. Sun, S. N. Zhu, and X. Zhang, *Magnetic Plasmon Propagation Along a Chain of Connected Subwavelength Resonators at Infrared Frequencies*, Phys. Rev. Lett. **97**, 243902 (2006).

[107] S. Zhang, W. Fan, N. C. Panoiu, K. J. Malloy, R. M. Osgood, and S. R. J. Brueck, *Optical negative-index bulk metamaterials consisting of 2D perforated metal-dielectric stacks*, Opt. Express **14**, 6778 (2006).

Acknowledgements

At this point, it is a great pleasure for me to thank all the people who have helped me and who have also contributed to the success of this thesis. It has been a short but very intensive time for me.

First of all, I would like to thank my advisor Prof. Martin Wegener for giving me the opportunity to work in the new and exciting field of photonic metamaterials. His enduring interest, his profound knowledge in the field of optics, many creative ideas, and fruitful discussion have been the successful fundament of my thesis. Sometimes the right question has opened a new route for the solution of a problem. Furthermore, it has been a pleasure to present my results on conferences.

I thank Prof. Kurt Busch for kindly agreeing to co-referee this thesis. Next, I want to express my gratitude to Stefan Linden who has supervised me during my Ph.D. thesis. His enduring support has also been an important factor for the success. Furthermore, he has greatly contributed to the readability and comprehensibility of this thesis. Additionally, I would like to thank Alexandra Ledermann for helping me with many details of the English language. Furthermore, as a non-expert in the field of metamaterials, she has improved the comprehensibility of this thesis. My thanks also goes to Matthias Klein for the enjoyable and intensive collaboration during the last few months. Besides building two complete new optical setups we have also worked on many questions concerning refraction. He also greatly contributed to the readability and comprehensibility of this thesis. I would also like to thank all the members of the Wegener group for many discussions (on and beyond science), the team spirit, and the comfortable atmosphere. It has also been a great pleasure for me to work with my former colleague Christian Enkrich. Together we have developed together the program for retrieving the refractive index.

I would like to thank Achim Schädle of the Nano-Photonics group at the ZIB in Berlin. He has dealt with the program JCMsuite and has optimized it according to our needs. Furthermore, his first numerical calculations regarding the beam displacement has helped me with my analytical calculations. Additionally, it was a pleasure for me to follow the invitation to a workshop on Nano-Photonics at the ZIB in Berlin. Furthermore, I would also like to thank Shuang Zhang for stimulating discussions during the DPG Summer School Metamaterials in Band Honnef.

My thanks also goes to the different facilities of the Institute of Applied Physics. Renate Helfen and Christa Weisenburger, our secretaires, have helped me with all bureaucratic tasks and problems. Furthermore, I would like to thank the DFG-Center for Functional Nanostructures (CFN) and the Karlsruhe School of Optics & Photonics (KSOP) for their support during my thesis. I am indebted to the electronic workshop. Especially in the last few months I have had the pleasure to challenge Heinz Hoffmann and Werner Gilde with a difficult problem for which they have found a wonderful solution. Furthermore, I have learned a lot about electronics. I thank Helmuth Lay from the electronic workshop for taking care of all computers. My thanks also goes to Thorsten Kuhn and the mechanical workshop who have dealt with all mechanical parts of the setups. It is pleasure to thank Jacques Hawecker for his kind introduction to scanning-electron microscopy and the usage of the specific

SEM.

Last, but definitely not least I would like to thank all of my friends and my family. A special thanks goes to my wife Susanne for her everlasting encouragement, precious love, and all the good times. Her enduring support built also the fundament for the success of my thesis.